


Spring 1-1-2015

Gravity Wave Propagation and Momentum Transport in Variable Environments

Katrina Bossert

University of Colorado Boulder, katrina.bossert@gmail.com

Follow this and additional works at: https://scholar.colorado.edu/asen_gradetds

 Part of the [Atmospheric Sciences Commons](#), [Remote Sensing Commons](#), and the [Systems Engineering and Multidisciplinary Design Optimization Commons](#)

Recommended Citation

Bossert, Katrina, "Gravity Wave Propagation and Momentum Transport in Variable Environments" (2015). *Aerospace Engineering Sciences Graduate Theses & Dissertations*. 119.

https://scholar.colorado.edu/asen_gradetds/119

This Dissertation is brought to you for free and open access by Aerospace Engineering Sciences at CU Scholar. It has been accepted for inclusion in Aerospace Engineering Sciences Graduate Theses & Dissertations by an authorized administrator of CU Scholar. For more information, please contact cuscholaradmin@colorado.edu.

Gravity Wave Propagation and Momentum Transport in Variable Environments

Ph.D. Thesis
By
Katrina Bossert

B.S., Electrical Engineering, University of Colorado, 2010

M.S. Electrical Engineering, University of Colorado, 2010

A thesis submitted to the
Faculty of the Graduate School of the
University of Colorado in partial fulfillment
of the requirement for the degree of
Doctor of Philosophy
Department of Aerospace Engineering Sciences
2015

This thesis entitled:
Gravity Wave Propagation and Momentum Transport in Variable Environments
Written by Katrina Bossert
has been approved for the Department of Aerospace Engineering Sciences

Dr. David Fritts

Prof. Jeffrey Thayer

Date: _____

The final copy of this thesis has been examined by the signatories, and we find that both the content and the form meet acceptable presentation standards of scholarly work in the above mentioned discipline.

Bossert, Katrina (Ph. D., Aerospace Engineering Sciences)

Gravity Wave Propagation and Momentum Transport in Variable Environments

Thesis directed by Dr. David Fritts

Gravity waves (GWs) play an important role in the dynamical processes of Earth's atmosphere. Momentum transport and deposition accompanying GW propagation and dissipation cause body forces that alter large-scale winds, and induce residual circulations from the troposphere into the mesosphere and lower thermosphere (MLT) and above. While these influences on mean state climatology are understood qualitatively, there remains a need for a more complete understanding of GW dynamics and their effects throughout the atmosphere. Small horizontal-scale GWs, especially those with large vertical wavelengths, account for a significant fraction of the total momentum fluxes (*MFs*) and the forcing of larger-scale motions. Yet these small-scale GWs are largely unresolved in global models and poorly described by parameterizations at present. Thus, a better understanding of small-scale GW (horizontal wavelengths < 100 km) dynamics and their influences on the momentum budget of the MLT is a major need.

This dissertation addresses small-scale GW dynamics and *MFs* in the MLT in variable environments using new state-of-the-art instrumentation. Data were provided by sodium resonance lidars, Advanced Mesospheric Temperature Mappers (AMTMs), and correlative instruments at the ALOMAR ground-based observatory in northern Norway, and employed during the Deep Propagating Gravity Wave Experiment (DEEPWAVE) performed in New Zealand in 2014. These data enabled quantification of multi-scale GW environments in which

larger-scale motions have strong influences on the propagation, evolution, *MFs*, and momentum deposition of smaller-scale GWs.

Results from ALOMAR revealed strong influences on small-scale GW propagation and *MFs* by variable large-scale wind and temperature fields, yielding variable propagation and ducting conditions, and occasional very large, local *MFs*. GW characterization and *MF* estimates using DEEPWAVE data likewise revealed a tendency for the largest *MFs* to be associated with smaller horizontal-scale GWs, often having magnitudes of many times larger than mean values in the MLT. DEEPWAVE measurements above regions of MW breaking also revealed apparent secondary GW generation, indicating more complex GW roles in momentum transport that must have significant, though unknown, implications at much higher altitudes.

Dedication

To my husband, my parents, and those who have paved the way before me.

We so often view the world around us as we have been taught to see it, and not as it is meant to be seen.

Acknowledgements

First, I would like to thank my research advisor Dr. Dave Fritts for guidance throughout this PhD as well as for providing many opportunities to grow as a researcher. I'm very lucky to have had these experiences working over at GATS. I would also like to thank my academic advisor, Dr. Jeffrey Thayer for introducing me to lidar and giving me the opportunity to learn using the ARCLITE system. I acknowledge my committee members Dr. Scott Palo, Dr. Al Gasiewski, and Dr. Jeffrey Forbes who have offered advice and feedback throughout this PhD process. Additionally, I acknowledge Dr. Xinzhao Chu, who provided a lidar course that helped prepare me for the lidar analysis portion of this PhD research.

I acknowledge my colleagues over at GATS. Dr. Bifford Williams has provided guidance with the ALOMAR lidar system, and built the DEEPWAVE sodium lidar system that provided results used in this thesis. Tyler Mixa assisted in taking data with the DEEPWAVE lidar system during the campaign. Dr. Brian Laughman has provided insight regarding gravity wave modeling and simulations.

I would also like to acknowledge my colleagues at other universities who have assisted in this research. Dr. Mike Taylor's group at Utah State University developed the Advanced Mesospheric Temperature Mapper that has been used in this thesis work. Dr. Pierre-Dominique Pautet has provided the AMTM data for both the ALOMAR and DEEPWAVE data sets, and also flew during every flight of the DEEPWAVE campaign to oversee the AMTM data collection. I owe a significant amount of gratitude to both Dr. Mike Taylor and Dr. Pierre-Dominique Pautet for their research input during this PhD.

I would like to thank Dr. Christopher Heale and Dr. Jonathan Snively at Embry-Riddle Aeronautical University for their contributions and insightful discussions regarding GW propagation and modeling. Dr. Christopher Heale provided output from a 2D GW model developed by Dr. Jonathan Snively that was used for calibration studies of the DEEPWAVE sodium lidar.

There were a large number of people involved during the DEEPWAVE campaign. I really want to recognize that without the dedication of so many scientists and engineers, I would not have access to such a wonderful data set. I especially acknowledge the contributions from those whose data was used in this thesis. The scientists and engineers from the Kingston meteor radar, Dr. Iain Reid, Dr. Damain Murphy, Dr. Andrew MacKinnon, and Andrew John Spargo, have provided an incredibly useful data set. I also acknowledge our colleagues from DLR. Dr. Andreas Dörnbrack provided ECMWF reanalysis for the flights during the DEEPWAVE campaign. Drs. Bernd and Natalie Kaifler developed and ran the Rayleigh lidar that was stationed at Lauder during the campaign.

The institute for atmospheric physics has provided collaborative data sets for ALOMAR. The SAURA radar data that was used in this dissertation was provided by Dr. Gunter Stober.

I would also like to thank Dr. Sharon Vadas for several insightful discussions regarding gravity waves. Her knowledge in this field and previous work has been helpful for my research.

Finally I would like to acknowledge my friends, family, and fellow students who have given me support throughout this process.

Contents

1. Introduction.....	1
1.1 Motivations.....	1
1.2 Gravity wave effects within the MLT.....	5
1.2.1 Gravity wave interactions with larger scale dynamics (tides, planetary waves, mean winds).....	5
1.2.2 The roles of small-scale GWs.....	6
1.3 GW modeling and parameterization.....	7
1.4 Instrumentation and observational studies of gravity waves.....	9
1.5 Research Overview.....	11
2. Gravity Wave Governing Equations.....	13
2.1 Overview of GW Equations.....	13
2.2 GW Momentum and Momentum Flux.....	17
3. Instrumentation.....	19
3.1 Advanced Mesospheric Temperature Mapper (AMTM).....	19
3.1.1 AMTM Measurement Overview.....	21
3.2 Sodium Lidar.....	26
3.2.1 Sodium Fluorescence Lidar Theory.....	26
3.2.2 Sodium Density Retrieval.....	29
3.2.3 Sodium Wind and Temperature Retrieval.....	29
3.2.4 Weber Sodium Lidar.....	32

3.2.5 DEEPWAVE Sodium Lidar	34
3.2.6 Lidar Sources of Error and Noise	44
3.3 Combined Sodium and AMTM measurements: An Overview.....	49
4. Gravity Wave Propagation Influences Due to Variable Background Environments	52
4.1 Small-scale GW propagation and characterization in variable environments	52
4.2 Influences of Propagation Environments.....	57
4.2.1 Gravity Wave Ducting	57
4.2.2 Small-scale Gravity Wave Propagation	72
4.2.3 Gravity Wave Critical Levels	78
4.3 Summary of Gravity Wave Propagation Due to Variable Background Environments	102
5. Small-Scale GW Forcing in the Mesosphere and Lower Thermosphere	104
5.1 GW Momentum Transport in a Multi-Scale Environment	105
5.2 Momentum Transport Due to Small-Scale Mountain Waves.....	116
5.3 Secondary GW Generation	128
5.4 Summary of small-scale GW Forcing.....	134
6. Conclusions.....	136
6.1 Gravity Wave Propagation in Variable Environments	136
6.2 Gravity Wave Momentum Flux Contributions.....	139
6.3 Overview and Future Work	140
References.....	143
Appendix A.....	155
Appendix B.....	164
Appendix C	168

Tables

Table 5.1: 240 km MW temperature perturbations and corresponding MF near 84 km	107
Table 5.2: 240 km MW mixing ratio vertical displacements near 83 km.....	108
Table 5.3: Estimated upper bound MF values for the ~240 km MW approximated from 83-87 km	110
Table 5.4: Small-scale parameters for passes 1-4 on the 13 July 2014 obtained from Figure 7	114
Table 5.5: Small-scale GW MF calculated without correcting for integration over the OH layer for passes 1 and 4 during the 13 July 2014 flight	114
Table 5.6: Parameters for observed GW on 29 June 2014 and corresponding MF calculation .	123
Table 5.7: Parameters for observed GW on 28 June 2014 and corresponding MF calculation .	127
Table B.1: Frequency offsets and relative line strengths	166

Figures

- Figure 1.1: The top panels show representations of the mid-latitude zonal winds in the summer and winter hemispheres as they would be without GW drag (dashed brown line) and the influence of GW drag on these winds that results in their zero crossing in the upper mesosphere (solid brown line). The bottom panels show the resulting meridional circulation accompanying the zonal wind reversals that causes an adiabatic cooling in the summer mesosphere and an adiabatic warming in the winter mesosphere. (Modified from Fritts, 2015). 2
- Figure 2.1: A diagram of induced acceleration on the background winds and resulting background wind increase due to a propagating GW 18
- Figure 3.1: An image of the AMTM at ALOMAR (credit: Dominique Pautet)..... 20
- Figure 3.2: A temperature image from the AMTM shows spatial values of temperatures integrated over the OH layer ~87 km..... 20
- Figure 3.3: AMTM measurements during intense background aurora..... 21
- Figure 3.4: AMTM measurement without aurora or auroral effects 22
- Figure 3.5: A simulation of detector noise as would be seen by the AMTM 23
- Figure 3.6: A keogram is shown in the bottom, and corresponding AMTM image for a given time is shown on the top. Lines through the image depict the north-south and east-west lines of data used in the keogram. Images from [Fritts *et al.*, 2014]. 25
- Figure 3.7: Spatial keograms from the DEEPWAVE flight on July 13, 2014 depict a stationary large-scale mountain wave, that would otherwise be undetected in a ground based instrument. 26
- Figure 3.8: Diagram of sodium hyperfine structure..... 28

Figure 3.9: Na absorption cross section plotted for different temperatures.....	30
Figure 3.10: Na absorption cross section plotted for different radial winds.....	30
Figure 3.11: Frequency lookup table	31
Figure 3.12: A system overview of the lidar transmitter	33
Figure 3.13: A system overview of the lidar receiver.....	34
Figure 3.14: Simulation output of large-amplitude wave temperatures and winds are shown in plots A and B. Simulated output of breaking wave temperatures and winds are shown in plots C and D.	36
Figure 3.15: Error due to 3 km pulse averaging. Plot A shows pulse averaging error for the large amplitude GW and plot B show the pulse averaging error for the breaking GW.....	37
Figure 3.16: Error due to vertical wind $\sim 0 \text{ ms}^{-1}$ assumption. Plot A shows the error for a large amplitude wave and Plot B shows the error for a breaking wave.....	38
Figure 3.17: Combined DEEPWAVE instrument specific errors. Plot A shows the total errors for the large amplitude wave and Plot B shows the total errors for the breaking wave.	39
Figure 3.18: Predicted measured versus actual modeled temperature and the associated temperature errors at 100 km. Plots A and C show the measured and actual temperatures for the large amplitude and breaking waves. Plots B and D show the associated temperature error at 100 km.....	40
Figure 3.19: Sodium densities for a low amplitude $\sim 40 \text{ km}$ horizontal GW	41
Figure 3.20: Temperature perturbations for the simulated $\sim 40 \text{ km}$ horizontal GW	41
Figure 3.21: Plot A shows the simple ratio of the scattering cross sections for F1 and F0 based on the winds and temperatures measured alone. Plot B gives the ratio of sodium densities measured at the two different averaging times for F1 and F0. Plot C shows the corrected	

ratio accounting for the difference in sodium densities and scattering cross sections as would be measured by return sodium counts along a flight track.	43
Figure 3.22: Plot A shows the measured temperatures for a timing offset resulting in a 3 spatial measurement difference for each frequency for a 40 km horizontal GW. Plot B shows the actual temperature perturbations of the 40 km horizontal GW.....	44
Figure 3.23: Plot A shows the 1.8m telescope overlap function and plot B shows the 0.5m telescope overlap function	45
Figure 3.24: The three frequencies used for sodium lidar (shown in orange) correspond to different absorption cross sections.....	47
Figure 3.25: Plot A on the left shows the temperature error from no extinction. Plot B on the right shows the corresponding cumulative sodium column abundance at each altitude.	48
Figure 3.27: A diagram of sodium layer and OH layer overlap observations.	50
Figure 3.28: Lidar weighted temperature and AMTM temperature	51
Figure 4.2: Sodium densities measured with the sodium resonance lidar at ALOMAR using a 1-min integration and 150-m range resolution on 22-23 January 2012.	60
Figure 4.3: Temperature profiles measured with the sodium lidar using 1.128 km and 1-hr averaging on 22-23 January 2012.	60
Figure 4.4: As in Figure 3 but for winds in the direction of GW propagation from east to west. Radial winds were converted to horizontal winds assuming vertical winds are zero for a 1-hr average.	61
Figure 4.5: N^2 calculated using the temperatures shown in Figure 3.....	62
Figure 4.6: Errors calculations from equation 4.3 associated with N^2 calculated from equation 4.1	62

Figure 4.7: m^2 values calculated including the wind shear and curvature terms.	63
Figure 4.8: Error calculated from equation 4.5 associated with m^2 calculation using equation 4.2	64
Figure 4.9: (Left panels) Predicted density perturbations using a constant temperature perturbation in altitude and time, the smoothed background sodium density, and average GW parameters measured over the night. (Middle panels) Measured sodium density perturbations. (Right panels) m^2 values for the corresponding time and altitude intervals. (left to right) Time intervals from 16 to 22 UT, 25 to 28 UT, and 28.8 to 30 UT. Calculations were made using an average of GW parameters observed throughout the night.	67
Figure 4.11: Spatial temperature map showing the 10-minute period GW	73
Figure 4.12: Lidar temperatures with 10 minute resolution for 27 January 2014	74
Figure 4.13: SAURA radar zonal winds with 7.5 minute resolution.....	74
Figure 4.14: SAURA radar meridional winds with 7.5 minute resolution	75
Figure 4.15: Calculation of N^2 using equation 4.1	76
Figure 4.16: Nightly average of N calculated using the data from Figure 4.15.....	76
Figure 4.17: Calculated m^2 for the 10-minute period GW.....	77
Figure 4.18: Example flight track over Mt. Cook.....	79
Figure 4.19: Flight diagram and approximate ground topography.....	79
Figure 4.20: GW overturning observed in the sodium mixing ratios on three different flights during the DEEPWAVE campaign.....	81
Figure 4.21: Rayleigh lidar temperature perturbations from the fourth pass show a vertical wavelength of ~20 km.	84

- Figure 4.22: ECMWF winds averaged over the duration of the flight with the maximum and minimum winds included for reference. 84
- Figure 4.23: ECMWF wind perturbation output at 43°S during the time of RF22 85
- Figure 4.24: Plot A shows Saber temperatures from two passes on 13 July 2014 at 12:38:21 and 12:39:31, and the averaged temperature between these passes. Plot B shows the nightly average from the Lauder Rayleigh Lidar on 12 July 2014 plotted with the averaged SABER temperature from plot A..... 86
- Figure 4.25: Imager intensities from the fourth pass of RF22 using the AMTM and side viewing IR cameras. These intensities show the ~240 km MW positioned over the South Island of New Zealand and spanning ~900 km meridionally. 88
- Figure 4.26: AMTM spatial keograms showing both the 240 km MW centered over New Zealand and several smaller-scale GWs. 88
- Figure 4.27: Kingston meteor radar wind 6-hour mean starting at 6 UT on 13 July 2014 show winds of 45ms^{-2} towards the east at 84 km and 25ms^{-1} towards the east at 87 km. 89
- Figure 4.28: Sodium mixing ratio contours for Passes 1 and 4 during 13 July 2014 flight. 90
- Figure 4.29: Small-scale GW observation from pass 4 during the 13 July 2014 flight. Figure A shows the AMTM observation of the overhead GW. Figure B shows the keogram for comparison. Figures C and D show the sodium mixing ratio and sodium density for the corresponding horizontal cross section of the AMTM spatial view. 92
- Figure 4.30: Above plots show data from the 1 July 2014 flight. Plot A shows the sodium mixing ratio indicating large perturbations for the ~100 km MW below 82 km, and no signal of this MW above 84 km. Plot B similarly shows density perturbations of the ~100 km MW that extend down to 74 km but are not visible above 84 km. Plot C clearly shows the ~100 km

MW temperature perturbations in the AMTM. Plot D shows the corresponding lidar temperatures, which indicate no temperature perturbations due to the ~100 km MW above 84 km.	95
Figure 4.31: Same Figure 4.30, but for the return pass over the island during the 1 July 2014 flight. These plots indicate a less defined ~100 km MW, but evidence is still visible in the sodium densities and AMTM temperatures.	96
Figure 4.32: Kingston meteor radar winds on 1 July 2014 both at the time of the measurements during the observed MW, and two hours ahead of the measurements to account for tidal differences between the meteor radar site at Tasmania and the South Island of New Zealand. Both measurements show a clear critical level for MW aligned zonally near 85 km in altitude.	97
Figure 4.33: Plots for the 4 July 2014 flight. Plot A shows temperatures measured from the sodium lidar. Plot B shows the sodium densities and D shows the mixing ratios computed from these densities. Plot C shows the OH imager keograms.	99
Figure 4.34: Plots from the 4 July 2014 flight. Plot A shows sodium densities. Plot B shows the corresponding OH imager keogram.	100
Figure 4.35: Plots A and B show the OH imager keograms at times before and after the observed strong MW activity on 4 July 2014.	100
Figure 4.36: Plots of Kingston meteor radar winds during 4 July 2014. Plot A shows wind vectors for the entire night. Plot B shows a 6-hour average surrounding the time of observation. Plot C shows a 6-hour average 2 hours ahead of the MW observation time to account for tidal differences between the DEEPWAVE observations and Kingston radar observation site.	101

- Figure 5.1: Sodium mixing ratios from the GV sodium lidar for the four RF22 flight segments on 13 July 2014 clearly show the ~240 km MW below 85 km, and strong dissipation of this MW above 85 km..... 108
- Figure 5.2: Overhead AMTM temperature maps of observed small-scale GWs during the four flight segments over Mt. Cook, NZ on 13 July 2014. The dashed boxes show the areas used for calculating temperature perturbations and wavelength using a Lomb Scargle periodogram. The arrows denote the intrinsic direction of propagation of the observed GWs. 111
- Figure 5.3: Sodium densities measured during the flight on 29 June 2014 between 15:16 UT and 15:37 UT..... 117
- Figure 5.4: Sodium mixing ratios measured during the flight on 29 June 2014 between 15:16 UT and 15:37 UT 117
- Figure 5.5: Sodium lidar temperatures measured during the flight on 29 June 2014 between 15:16 UT and 15:37 UT..... 118
- Figure 5.6: N^2 values calculated from smoothed temperatures for the flight on 29 June 2014 between 15:16 UT and 15:37 UT..... 119
- Figure 5.7: OH imager views corresponding to the lidar data from the 29 June flight. The blue arrows point out the two phases of the MW. 120
- Figure 5.8: AMTM keogram corresponding to the lidar data from the 29 June flight. The northern portion corresponds to the data shown in Figures 5.3-5.7..... 120
- Figure 5.9: OH images from the 29 June 2014 flight. Figure A shows the MW observation on the southern pass, which is apparent in the overhead camera and in the north viewing OH camera. Figure B shows the MW observation in the west viewing camera over the region of

the north flight track. A and B show the beginning and end of the MW, which persisted for ~1hr.	121
Figure 5.10: SABER data on 29 June 2014 showing the variability of the OH layer over a short distance of 1.3° latitude and 2.8° longitude. At 10:55:57, the OH layer appears to have a double peak at 85 and 80 km with a FWHM of ~11 km. At 10:55:57, the OH layer appears to be centered near 85 km with a FWHM ~7 km.....	122
Figure 5.11: Sodium densities from 28 June 2014 from 11:09-11:35 UT.....	124
Figure 5.12: The Plot A shows the sodium mixing ratios for the bottom side of the layer on 28 June 2014. Plot B shows the sodium densities for the bottom side of the layer. Near the Eastern end of the flight GW overturning is apparent.	124
Figure 5.13: Overhead OH camera images from 28 June 2014 show the MW appears at the western edge of the island and is spatially visible until the eastern edge.	125
Figure 5.14: Sodium lidar temperatures from 28 June 2014 from 11:09-11:35UT.....	126
Figure 5.15: N^2 values calculated from smoothed temperatures for the flight on 28 June 2014 from 11:09-11:35UT.....	127
Figure 5.16: Sodium mixing ratios at different altitudes for the first pass of the flight on 13 July 2014. Plot A shows lower altitudes below the critical level where MWs are still present. Plot B shows smaller scale GWs starting to appear near 90 km where a critical level is predicted. Plots C and D show the multiple different scales and phases of smaller scale GWs above the critical level.	129
Figure 5.17: Plot A shows sodium densities for 29 June 2014 and Plot B shows the corresponding mixing ratios.	130

Figure 5.18: Temperatures for 29 June 2014 from 15:16-15:37 UT using 1.2 km vertical averaging.....	131
Figure 5.19: Sodium densities on 28 June 2014. The arrows highlight the area of observed GW overturning.....	132
Figure 5.20: Sodium mixing ratios on 28 June 2014. The arrows highlight the area of observed GW overturning	132
Figure 5.21: Temperatures on 28 June 2014. The arrows highlight the wave structure observed above the region of GW overturning.	133

1. Introduction

1.1 Motivations

GWs, also referred to as buoyancy waves, play a critical role in transporting momentum throughout the Earth's atmosphere. They are the dominant mechanism for vertical transport of horizontal momentum from source regions in the lower atmosphere to regions of GW dissipation that may occur at much higher altitudes. GWs that reach the mesosphere and lower thermosphere (MLT) from about 60-90 km have especially strong influences on the climatology and circulation in the MLT as their momentum deposition in this region causes a mean drag on the zonal mean winds, resulting in reversals of the zonal jets and a mean meridional circulation that leads to a warmer winter mesopause and colder summer mesopause than would occur without GW momentum transport [*Lindzen, 1981; Holton, 1982; Garcia and Solomon, 1985*]. Figure 1.1 shows a diagram overview of the influences of GW induced drag on the atmosphere.

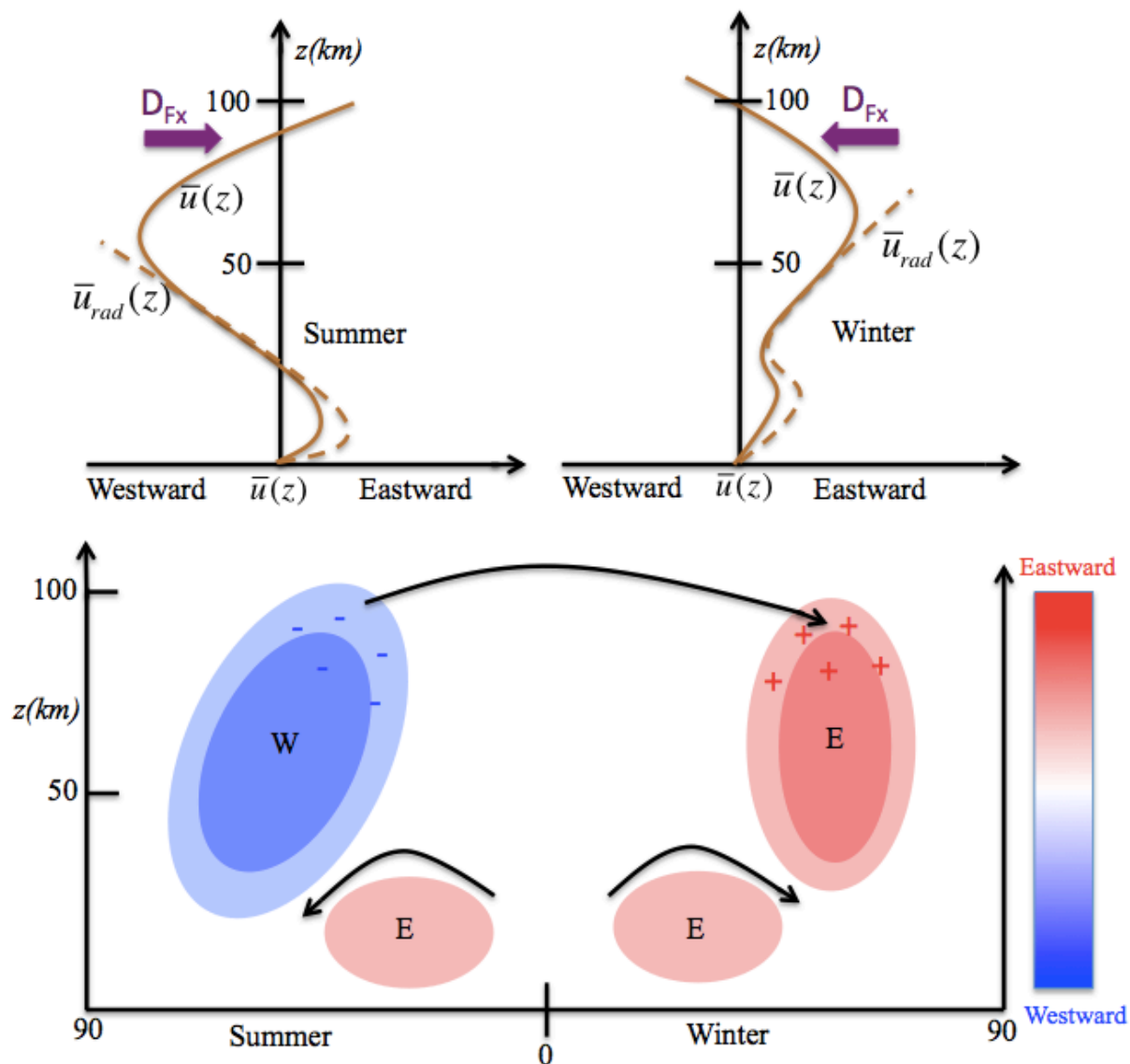


Figure 1.1: The top panels show representations of the mid-latitude zonal winds in the summer and winter hemispheres as they would be without GW drag (dashed brown line) and the influence of GW drag on these winds that results in their zero crossing in the upper mesosphere (solid brown line). The bottom panels show the resulting meridional circulation accompanying the zonal wind reversals that causes an adiabatic cooling in the summer mesosphere and an adiabatic warming in the winter mesosphere. (Modified from Fritts, 2015).

The linear theory of atmospheric GWs extending to high altitudes was developed by Colin Hines [*Hines*, 1960], and our understanding of the sources of GWs and their implications for the atmosphere has advanced significantly since this first study. Lindzen [1981] and Holton [1982, 1984] demonstrated the importance of GW breaking and turbulence in the MLT. Garcia and Solomon [1985] took these GW studies further, and accounted not only for the dynamical effects of GW breaking in the MLT region, but also the effects this had on the chemical composition in this region. These studies showed that GWs are responsible for the high latitude cold summer mesopause, and contribute to seasonal chemical composition differences within the MLT.

GWs are generated from several sources that include topography, convection, jet streams, and secondary wave generation. Topographic GW generation occurs when air flows over an obstacle such as a mountain, leading to vertical parcel displacements determined by the terrain. Topographic or mountain waves have been observed both in situ via aircraft [*Lilly and Kennedy*, 1973; *Smith*, 1978], and remotely using instrumentation such as radars [*Fritts et al.*, 1990]. Studies have shown that GWs generated over mountainous regions have significantly higher variances than GWs generated over flat or topographically insignificant regions [*Nastrom et al.*, 1987; *Fritts and Nastrom*, 1992]. While this indicates the importance of topographically generated GWs, not all strong GWs generated at the surface will attain high altitudes, as atmospheric filtering and instabilities can prevent these GWs from propagating to higher altitudes above the troposphere.

Other sources of GW generation also play a significant role throughout the atmosphere. Convective GWs can be generated through several suggested mechanisms including the obstacle effect [*Clark et al*, 1986], which involves a convective obstacle that can generate GWs in a

manner similar to airflow over topography, and by pure thermal forcing [Salby and Garcia, 1987]. Several observational studies suggest that convectively generated GWs near the troposphere and lower stratosphere can propagate up to the MLT under the right conditions [Yue et al., 2009; Vadas et al., 2012], showing the important influences that these GWs may have in the MLT. Jet streams and wind shear also contribute to GW generation through geostrophic adjustment [Fritts and Luo, 1992], and shear instabilities such as Kelvin Helmholtz instabilities [Scinocca and Ford, 2000; Fritts, 1984; Chimonas and Grant, 1984]. GWs can also be generated from other GW interactions, instabilities, and breaking [Vadas et al., 2003; Lane et al., 2006]. This method of GW generation is known as secondary GW generation, and also contributes GW generation well above the troposphere.

GW spectra evolve with altitude, which can partially be explained by the different generation mechanisms discussed above. In the troposphere, much of the GW generation is driven by topography and convection, which produce GW scales dependent on terrain, geometry, and timescale. As altitude increases, the jet stream, instabilities, and secondary GW generation add to the spectrum of GWs. Thus in the MLT, observed GWs typically come from a number of sources. Additionally, GWs grow exponentially with altitude due to the decreasing background atmospheric density. GWs able to achieve high altitudes within the MLT, also have higher associated amplitudes and momentum flux due to the growth with altitude, further increasing their momentum deposition in this region of the atmosphere. The scales and amplitudes of GWs that are able to reach the MLT are ultimately determined by various background conditions. As GWs increase amplitudes, they become more susceptible to instabilities. However, the atmospheric background conditions, in addition to instabilities, largely determine which GWs have the ability to propagate to any given altitude. The GWs may be filtered before reaching the

MLT due to dissipation, instabilities, breaking, or critical levels resulting in absorption or reflection. Thus, the propagation environment and variability of the background atmosphere play a key role in the GW momentum that reaches the MLT.

1.2 Gravity wave effects within the MLT

1.2.1 Gravity wave interactions with larger scale dynamics (tides, planetary waves, mean winds)

The ability of GWs to propagate to altitudes that reach into the MLT region is strongly dependent on background propagation environment conditions. Under favorable propagation conditions, the amplitudes of GWs increase exponentially with increasing altitude due to the decreasing background density. Larger-scale dynamics can affect GW propagation by producing environments that are conducive to GW propagation, or by creating unfavorable propagation environments that can cause GWs to dissipate, reflect, or become unstable. In this section the important effects that GWs have in the MLT and the interactions between GWs and larger-scale dynamics are discussed.

While GW momentum deposition has been shown to impact larger scale dynamics such as mean and zonal winds, GWs can also be strongly influenced by larger scale background dynamics. Observations of GWs have shown there is a seasonal dependence on the propagation direction and spectra of GWs within the MLT that correlates with seasonal changes in background mean winds [Espy *et al.*, 2004b]. Background and mean winds can filter out various spectra of GWs [Taylor *et al.*, 2003; Fritts and Vadas, 2008], as a background wind can generate a critical level or reflection point for small-scale GWs with high phase speeds. This causes a

preference for GWs propagating in a specific direction [Beres *et al.*, 2002]. Additionally, winds and wind shear can also generate instabilities that contribute to wave dissipation.

Tides affect GW propagation and produce filtering effects that modulate GW momentum transport to the MLT [Liu *et al.*, 2013; Fritts and Vincent, 1987; Espy *et al.*, 2004a; Forbes *et al.*, 1984]. Tidal structure can also cause ducting of smaller-scale GWs [Snively *et al.*, 2007]. Similarly, PWs have also been found to have influences such as filtering effects on GWs [Dunkerton and Butchart, 1984; Lieberman *et al.*, 2013; Smith 1995; Manson *et al.*, 2003]. Conversely, while being strongly influenced by these larger scale dynamics, GWs may also play a role in influencing larger scale dynamics such as tides [Nakamura *et al.*, 1987; Walterscheid, 1981; Liu *et al.*, 2013].

The relationship between GWs and larger scale-dynamics is complex due the nature that both the smaller-scale GWs and the dynamics influence each other. For instance, slow dissipation of a GW due to instabilities will deposit momentum and energy as it propagates, which acts as a force on local background mean flow. GW instabilities can arise from either the GW itself growing too large, or they can arise from background environment conditions such as local shear and convective instabilities. A better understanding of the GW filtering that takes place due to various mechanisms of the background dynamics will allow for more accurate ways of characterizing smaller-scale GWs and their influences on the momentum budget within the MLT under various background conditions.

1.2.2 The roles of small-scale GWs

Small-scale GWs are especially of interest as several studies suggest that smaller-scale GWs (< 100 km) contribute significantly to the total momentum flux budget [Smith *et al.*, 2008;

Plougonven et al., 2008; *Nastrom and Fritts*, 1992; *Vincent and Reid*, 1983; *Preusse*, 2008; *Hertzog et al.*, 2012]. Short horizontal wavelength GWs with large vertical wavelengths and group velocities will attain the highest MF s (the theory for GWs and associated MF is discussed further in section 2). Despite these potentially large momentum flux influences, small-scale GWs are mostly unaccounted for in global models.

Especially short horizontal wavelength GWs ($< \sim 40$ km) with high intrinsic phase speeds can be particularly prone to reflection and ducting within the atmosphere, although all GWs can be ducted under the specific atmospheric conditions [*Chimonas and Hines*, 1986]. Ducted GWs generally have vertical evanescent regions, which are readily observed by OH imagers. It is important to understand the conditions under which these small-scale GWs can be ducted as ducting disrupts the vertical transport of horizontal momentum, and ducted GWs do not contribute to the vertical momentum flux over the area which they are observed. Freely propagating GWs have the potential to contribute large, localized MF values that can greatly influence the MLT.

Given the potentially large MF influences due to small horizontal scale GWs and the strong dependence on background environment that the propagation of these GWs has, studying small-scale GWs is of interest for a better understanding of the full effects of GW influences in the atmosphere, and especially the MLT.

1.3 GW modeling and parameterization

Global models provide a method of understanding large-scale dynamical and climatological processes. They deliver a complement to direct measurements, which are unable to cover all locations and all times. Global models are generally constrained by resolution, and

do not presently accurately account for small-scale atmospheric activity on the order of tens of kilometers. Given these constraints, smaller-scale GWs are accounted for in models by using a general parameterization of GW drag (GWD) in the atmosphere [Kim *et al.*, 2003; McLandress, 1998]. These parameterizations of GWD were initially implemented in models to account for necessary adjustments in modeled zonal jets [McFarlane, 1987; Palmer *et al.*, 1986], and showed the important roles that GWD plays on large-scale dynamics in the lower and middle atmosphere. The early parameterizations focused on orographic sources of GWD generation. These parameterizations have gone hand in hand with the ability to do localized modeling of GW generation due to topographic sources [Dornbrack *et al.*, 1999; Durran and Klemp, 1987; Farmer and Armi, 1999]. While this addresses the sources of GWs that may dominate the lower atmosphere, it becomes necessary to include non-orographic GW sources, such as convectively generated GWs, as model altitudes increase [Alexander *et al.*, 2010; Kim *et al.* 2003]. A review of older non-orographic GW parameterization methods is provided in McLandress [1998]. Many methods involve the parameterization of a spectral range of non-orographic GWD [Fritts and Lu, 1993; Alexander and Dunkerton, 1999; Scinocca, 2003].

While these parameterization methods have continued to improve and provide more accurate representations of GWD, small-scale GWs are still unresolved by current global models, and there remain unanswered questions about missing sources of GWD [McLandress *et al.*, 2012; Jiang *et al.*, 2014; Alexander, 2010]. Many comparisons between climate models and measurements are done using satellite measurements [Gellar *et al.*, 2013; Alexander and Barnett, 2007]. Satellite measurements provide a source of measurements that cover many regions of the globe. However, these measurements may be biased in terms of larger wavelength GWs that are more readily observed by satellites, and lack the sensitivity to the shorter wavelength spectra

GWs that can significantly contribute to the momentum flux budget within the atmosphere [Preusse *et al.*, 2008]. Ultimately, while the parameterizations of GWD can be tuned in models to account for effects on mean wind, it remains difficult to quantify and compare modeled GWD with GW observations [Alexander, 2010]. There is still a need for more accurate high-resolution experimental measurements and quantifications of GW *MFs* both on a localized and global scale.

1.4 Instrumentation and observational studies of gravity waves

Remote sensing instrumentation has played an important part in the characterization of GWs within the MLT region of the atmosphere. The instrumentation used has changed over the years, and this section gives an overview of the history of measurements of GWs within the MLT, and the current instrumentation techniques used to obtain information about MLT GWs.

Lidars have been used to study the MLT since the advent of metal resonance fluorescence lidars. Initial measurements of sodium densities were used to determine GW parameters [Gardener and Shelton, 1985], and the eventual development of wind and temperature measurement techniques using resonance fluorescence lidars in the MLT have allowed for more in-depth characterizations of GWs [Collins *et al.*, 1996; Wilson *et al.*, 1991; Hu *et al.*, 2002; Williams *et al.*, 2002; Yue *et al.*, 2010]. While ground-based lidars have the ability to measure the period of GWs passing overhead, the drawback of these systems is their inability to directly measure horizontal wavelengths. Stationary ground-based lidars also lack the ability to reliably discern mountain waves (MWs).

Airglow emissions from the MLT have played an integral role in allowing for observations and characterizations of GWs within the MLT. These emissions can come from the sodium and the hydroxyl layer, producing photon emissions from various chemical reactions.

Airglow images were first produced by [Peterson and Keiffaber, 1973], and have since been used as a standalone instrument in numerous GW studies e.g. [Yue et al., 2009; Taylor et al., 1997; Taylor et al., 2003]. These airglow observations provide a means of measuring ground-relative phase speeds of GWs and the horizontal wavelengths and orientations of GWs that are within the field of view of the imager (usually less than several hundred kilometers). Previous techniques using airglow imagers could calculate temperatures from the observed intensities using the Krassovsky ratio [Krassovsky, 1972]. However, this method can be highly inaccurate. More recently, airglow emissions have been used to detect temperatures through an instrument called the Advanced Mesospheric Temperature Mapper (AMTM) developed at Utah State University by Dr. Mike Taylor and colleagues [Pautet, et al., 2014].

In addition to lidars and airglow imagers, other instruments have also contributed to our understanding of GWs within the MLT. As discussed in section 1.2, satellites have provided a valuable means of global GW measurements, but are biased towards larger horizontal wavelengths that are more readily detectable by satellites. Radars have also provided the ability to characterize GWs through MF, VHF, UHF and meteor radar wind measurements [Reid et al., 1988; Tsuda et al., 1990; Murphy and Vincent, 1993; Nakamura et al., 1993].

Various instrument combinations provide more complete data sets. There have been several studies done using combinations of existing instruments (e.g. lidar, radar, imagers) [Cai et al., 2014; Collins and Smith, 2004; Namboothiri et al., 1996; Nielsen et al., 2012; Hecht et al., 2001; Hecht et al., 1997]. Studies using both lidars and imagers prove especially beneficial, as the lidars can characterize the background wind and temperature environment, and imagers can define GW amplitudes, horizontal wavelengths, and phase speeds. The AMTM is discussed in more detail in section 3.1, and the sodium lidar is further discussed in section 3.2.

1.5 Research Overview

While significant research progress has been made to better understand GWs and their interactions with the atmosphere [*Fritts and Alexander, 2003; Alexander et al., 2010*], there still remain many questions about GW multi-scale interactions, filtering, and instabilities that all contribute to the varying GW spectrum and *MFs* with altitude. This dissertation contributes to these broader goals by addressing the following questions:

- 1) How are GW propagation and *MF* affected by variable background environments?
- 2) What contributions do smaller-scale GWs (horizontal scales < 100 km) make to the momentum budget of the MLT?

These studies are carried out utilizing the combination of the Advanced Mesospheric Temperature Mapper (AMTM) and a sodium resonance fluorescence Light Detection and Ranging (LiDAR) system. The AMTM measures temperatures using emission lines from the hydroxyl layer centered at ~87 km. These temperature measurements provide a spatial view of ~180 x 144 km which allows for the calculation of spatial temperature perturbations, wavelengths, and relative phase speeds of small horizontal-scale GWs (on the order of ~100 kilometers or less). Sodium LiDARs provide wind and temperature measurements in altitude and time from ~80-110 km. This allows for the derivation of the local background winds and temperature gradients for observed GWs in the AMTM. These measurements are implemented using the following research facilities:

Arctic Lidar Observatory for Middle Atmosphere Research ALOMAR:

The ALOMAR facility houses the Weber sodium lidar. During the winter months when the conditions allow for airglow measurements, the AMTM is also housed at ALOMAR. This research facility provides measurements at an Arctic location, and provides the opportunity for collaborative measurements with other instruments including the IAP Rayleigh Lidar, Meteor radar, and SAURA radar.

DEEPWAVE:

The DEEPWAVE campaign took place during June/July 2014 out of Christchurch, NZ. This data set includes data obtained over more than 130 flight hours from the NSF/NCAR Gulfstream V jet, which housed a sodium lidar, Rayleigh lidar, AMTM overhead camera, two side-view airglow imagers, dropsondes, and flight level data. This data set also comprises of measurements from the Lauder, NZ ground based station that included a second USU AMTM as well as a DLR Rayleigh lidar.

Section 2 of this dissertation discusses the theory of GWs. The instrumentation used for the studies examined in this dissertation is discussed in section 3. Section 4 discusses the impacts of local background environment on the propagation of small-scale GWs, and the experimental observations and case studies that have been done regarding these environmental influences. Section 5 discusses the contributions that small-scale GWs have to the momentum flux budget within the MLT.

2. Gravity Wave Governing Equations

2.1 Overview of GW Equations

Gravity wave behavior may be described using the equations expressing the conservation of mass, momentum, and energy [Fritts and Alexander 2003]. The general equations are nonlinear and account for several aspects of GW dynamics under ideal circumstances. For the purposes of this research, the equations can be simplified in several ways while retaining key terms relevant to the applications of this dissertation. Since the main focus of this research is small-scale GWs, the Earth's rotational effects are not important and left out of these equations. Also, since these GWs in the MLT occur at scales only weakly influenced by dissipation, inviscid motions are assumed. Additionally, the GWs are assumed to be isentropic. It is also assumed that the background atmosphere varies only in altitude, hence GW variations will occur only in the plane of propagation. These assumptions lead to the following equations for two-dimensional (2-D) motions in a vertical plane.

$$\frac{Du}{Dt} + \frac{1}{\rho} \frac{\partial p}{\partial x} = 0 \quad (1)$$

$$\frac{Dw}{Dt} + \frac{1}{\rho} \frac{\partial p}{\partial z} + g = 0 \quad (2)$$

$$\frac{D\theta}{Dt} = 0 \quad (3)$$

$$\frac{1}{\rho} \frac{D\rho}{Dt} + \frac{\partial u}{\partial x} + \frac{\partial w}{\partial z} = 0 \quad (4)$$

Here D/Dt is the material derivative, u is horizontal velocity, w is vertical velocity, p is pressure, ρ is the density, x and z are the horizontal and vertical directions, and θ is the potential temperature which can be written as:

$$\theta = \frac{p}{\rho R} \left(\frac{p_0}{p} \right)^{R/c_p} \quad (2.5)$$

Assuming that perturbations are small, these equations can be linearized assuming background parameters of \bar{u} , $\bar{w}=0$, $\bar{\theta}$, \bar{p} , and $\bar{\rho}$. Linearizing and expanding the above equations 2.1-2.4 and expanding the material derivative, equations 2.7-2.10 can be obtained. The following derivation accounts for a wind shear with altitude, which has been assumed to be zero in Fritts and Alexander, [2003].

$$\frac{du'}{dt} + \bar{u} \frac{\partial u'}{\partial x} + w' \frac{\partial \bar{u}}{\partial z} + \frac{\partial}{\partial x} \left(\frac{p'}{\bar{\rho}} \right) = 0 \quad (2.6)$$

$$\frac{dw'}{dt} + \bar{u} \frac{\partial w'}{\partial x} + \frac{\partial}{\partial z} \left(\frac{p'}{\bar{\rho}} \right) - \frac{1}{H} \left(\frac{p'}{\bar{\rho}} \right) + g \frac{\rho'}{\bar{\rho}} = 0 \quad (2.7)$$

$$\frac{d}{dt} \left(\frac{\theta'}{\bar{\theta}} \right) + \bar{u} \frac{\partial}{\partial x} \left(\frac{\theta'}{\bar{\theta}} \right) + w' \frac{N^2}{g} = 0 \quad (2.8)$$

$$\frac{d}{dt} \left(\frac{\rho'}{\bar{\rho}} \right) + \bar{u} \frac{\partial}{\partial x} \left(\frac{\rho'}{\bar{\rho}} \right) + \frac{\partial u'}{\partial x} + \frac{\partial w'}{\partial z} - \frac{w'}{H} = 0 \quad (2.9)$$

Assuming perturbations of the form:

$$\left(u', w', \frac{\theta'}{\bar{\theta}}, \frac{\rho'}{\bar{\rho}}, \frac{p'}{\bar{p}}\right) = (\tilde{u}, \tilde{w}, \tilde{\theta}, \tilde{\rho}, \tilde{p}) \exp\left[i(kx + mz - \omega t) + \frac{z}{2H}\right] \quad (2.10)$$

where H is the scale height, and $z/2H$ accounts for perturbation growth to conserve the kinetic energy of the GW, equations 2.7-2.10 can be rearranged into the following form:

$$-i\hat{\omega}\tilde{u} + w' \frac{\partial \bar{u}}{\partial z} + ik \frac{p'}{\bar{\rho}} = 0 \quad (2.11)$$

$$-i\hat{\omega}\tilde{w} + \frac{\partial}{\partial z} \left(\frac{p'}{\bar{\rho}}\right) - \frac{p'}{\bar{\rho}} \frac{1}{H} + g \frac{\rho'}{\bar{\rho}} = 0 \quad (2.12)$$

$$i\hat{\omega}\tilde{\rho} + \frac{N^2}{g} \tilde{w} = 0 \quad (2.13)$$

$$-i\hat{\omega}\tilde{p} + ik\tilde{u} + \frac{\partial \tilde{w}}{\partial z} - \frac{\tilde{w}}{H} = 0 \quad (2.14)$$

Here N is the buoyancy frequency given in equation 2.15, $k=2\pi/\lambda_x$ is the horizontal wavenumber, $m=2\pi/\lambda_z$ is the vertical wavenumber, λ_x and λ_z are the horizontal and vertical GW wavelengths, ω is the ground-relative frequency of the GW, and $\hat{\omega} = \omega - ku$ is the intrinsic frequency.

$$N^2 = \frac{g}{T} \left(\frac{dT}{dz} + \Gamma \right) \quad (2.15)$$

A complete derivation of equations 2.11-2.14 from 2.1-2.4 is given in Appendix A. These equations can be rearranged into relations between different perturbation quantities. These

relations are called the polarization relations, and allow for the phases and amplitudes of different GW parameters to be compared. Neglecting wind shear, these relations are given in 2.16-2.19.

$$\tilde{\rho} = \frac{iN^2}{\hat{\omega}g} \tilde{w} \quad (2.16)$$

$$\tilde{w} = \frac{\hat{\omega} \left(-m - \frac{i}{2H} \right)}{(N^2 - \hat{\omega}^2)} \tilde{p} \quad (2.17)$$

$$\tilde{\theta} = \frac{-iN^2}{\hat{\omega}g} \tilde{w} \quad (2.18)$$

$$\tilde{w} = \frac{k \left(-m - \frac{i}{2H} \right)}{(N^2 - \hat{\omega}^2)} \tilde{u} \quad (2.19)$$

Utilizing equations 2.11-2.14, the dispersion relation can be obtained. This is given by:

$$\hat{\omega} = \frac{k^2 N^2}{\left(k^2 + m^2 + \frac{1}{4H^2} \right)} \quad (2.20)$$

The vertical wavenumber can be obtained from this dispersion relation and is given by:

$$m^2 = \frac{N^2}{(c-u)^2} - k^2 - \frac{1}{4H^2} \quad (2.21)$$

A more complete version of m^2 has been derived by [Nappo, 2013] using the Taylor-Goldstein equation. This version accounts for shear and curvature in the vertical wind field and is given below:

$$m^2 = \frac{N^2}{(c-u)^2} + \frac{1}{(c-u)} \frac{d^2u}{dz^2} - \frac{1}{H(c-u)} \frac{du}{dz} - \frac{1}{4H^2} - k^2 \quad (2.22)$$

2.2 GW Momentum and Momentum Flux

The vertical flux of horizontal momentum is given by $\bar{\rho}\langle u'w' \rangle$. Here $\langle \rangle$ denotes an average over the GW phase. The momentum flux per unit density, $\langle u'w' \rangle$, can be written in terms of measurable parameters from both the AMTM and sodium lidar, as given in equation 2.23. The complete derivation of equation 2.23 is given in Appendix A.

$$\langle u'w' \rangle = \frac{1}{2} \tilde{u}^2 \left(\frac{k}{m} \right) = \frac{1}{2} \left(\frac{\tilde{\theta}}{\bar{\theta}} \frac{g}{N} \right)^2 \left(\frac{k}{m} \right) \quad (2.23)$$

While older techniques using imagers developed methods to calculate the temperature perturbation used in the above equation from intensity perturbations observed by the imager, the AMTM allows for the temperature perturbation to be obtained directly from the OH(3,1) layer emissions. Furthermore, correlative lidar data provide specification of the background temperatures and horizontal winds with altitude, which are key to understanding the GW propagation environments.

The momentum flux is important as the momentum associated with propagating GWs amounts to an acceleration of the background wind that is transient until the GW dissipates. The momentum expressed by equation 2.24 is conserved following GW propagation, and becomes permanent where the GW has dissipated.

$$Momentum = \int_0^{\infty} \bar{\rho}(z) \Delta \bar{u}(z) dz \quad (2.24)$$

The acceleration accompanying GW propagation is given in equation 2.25 from Fritts [1984].

$$\frac{\partial \bar{u}}{\partial t} = -\frac{1}{\rho} \frac{\partial}{\partial z} (\rho \langle u' w' \rangle) \quad (2.25)$$

As shown in Figure 2.1, for a GW packet propagating upward, the background wind accelerates to a maximum value based background density as in equation 2.24, and decreases to what it was before the GW entered the region for conservative propagation. For dissipating GWs, part or all of this momentum is left behind depending on the degree of dissipation, resulting in a permanent change in the background wind in the direction of horizontal GW propagation.

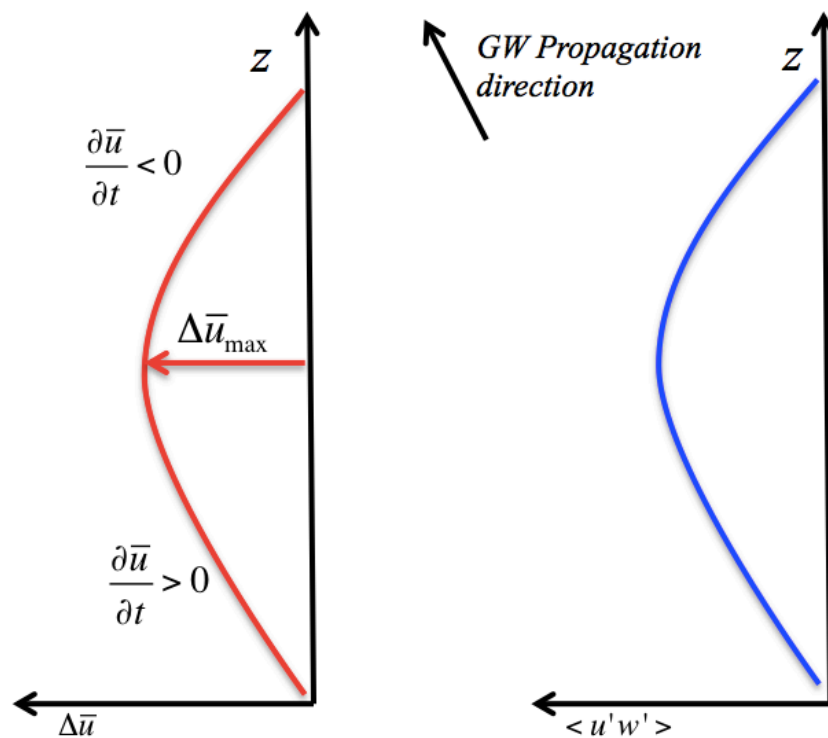


Figure 2.1: A diagram of induced acceleration on the background winds and resulting background wind increase due to a propagating GW

3. Instrumentation

3.1 Advanced Mesospheric Temperature Mapper (AMTM)

This section provides an overview of the AMTM. The AMTM data, provided by Utah State University, is used throughout this dissertation in many of the studies. A more in depth discussion of the theory behind this instrument is given in Appendix B.

The AMTM was developed at Utah State University by Dr. Mike Taylor and colleagues [Pautet *et al.*, 2014]. The AMTM provides a 2-D spatial map of the OH(3,1) rotational temperature and band intensity over a field of view of 144 km X 180 km centered at zenith. The measured temperatures result from a weighted average of emissions over the nocturnal OH layer, which is generally centered near 87 km with a FWHM of ~8 km [She and Lowe, 1998; Baker and Stair, 1988].

The imaging system uses three narrow band filters centered on the P1(2) and P1(4) lines of the OH(3,1) band, and a nearby region to assess the background level emissions. The emission returns are then imaged onto an InGaAs detector that is 320 X 256 pixels. This detector is cooled to -50° C which helps to reduce electronic noise. At ALOMAR, a complete temperature profile is collected every 41 seconds, and this was adjusted for the DEEPWAVE campaign to complete a temperature profile every 17 seconds. The ground-based AMTM has a horizontal resolution of ~0.5 km while the DEEPWAVE flight based AMTM has a horizontal resolution of ~1 km. The

AMTM placed at ALOMAR is shown in Figure 3.1. A temperature map from this instrument is given in Figure 3.2.



Figure 3.1: An image of the AMTM at ALOMAR (credit: Dominique Pautet)

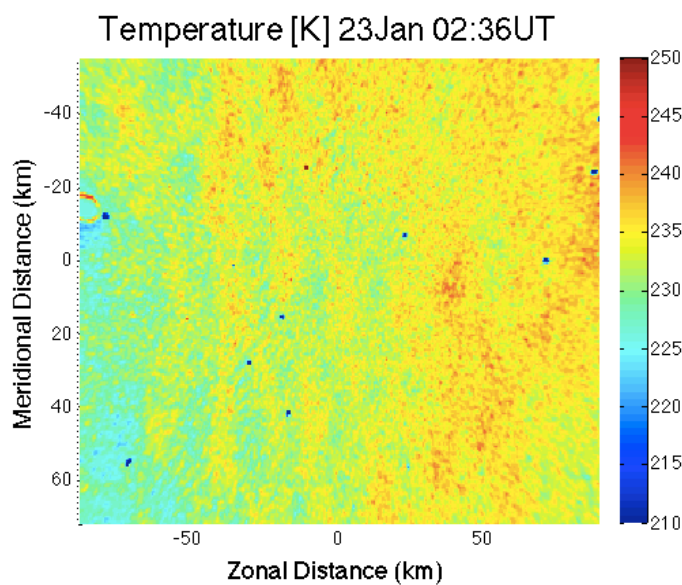


Figure 3.2: A temperature image from the AMTM shows spatial values of temperatures integrated over the OH layer ~ 87 km

3.1.1 AMTM Measurement Overview

3.1.1a Sources of Noise and Error

While, the AMTM yields reliable temperature measurements from the OH layer, there are several sources of error that can contribute to the reliability of the measurement. Some of these uncertainties arise from the instrument itself, while others are environmental factors. These errors and uncertainty sources are described in the following segments.

Background Light Sources

Due to the sensitivity of the system to low photon emissions, background light sources can cause issues in the data. Sources of background light include light from contamination from the facility (for this reason the rooftop at ALOMAR is kept dark), twilight, aurora, and a full moon. Aurora can be a source of error in the detector if the event is strong enough. However, during aurora, there may still be portions of the field of view that are unaffected. Figure 3.3 shows two images from the AMTM during a time of aurora. Figure 3.4 shows an unaffected image for comparison.

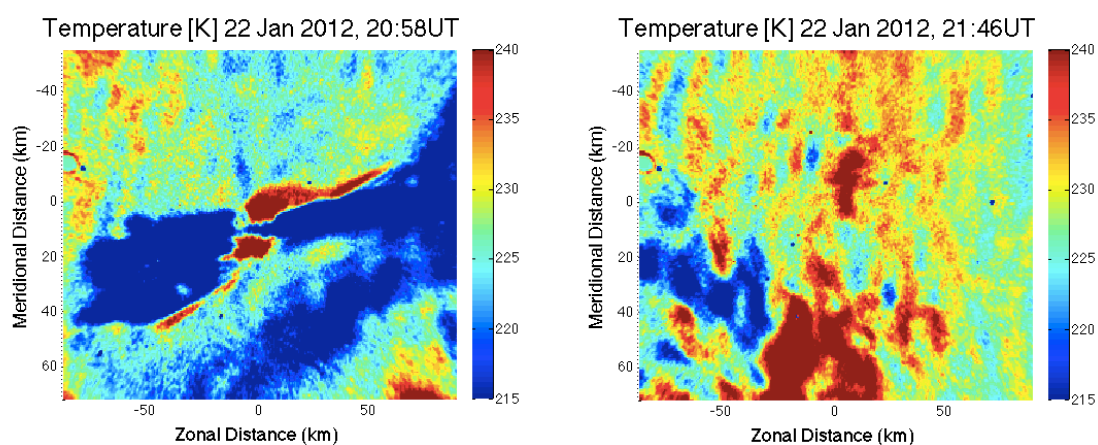


Figure 3.3: AMTM measurements during intense background aurora

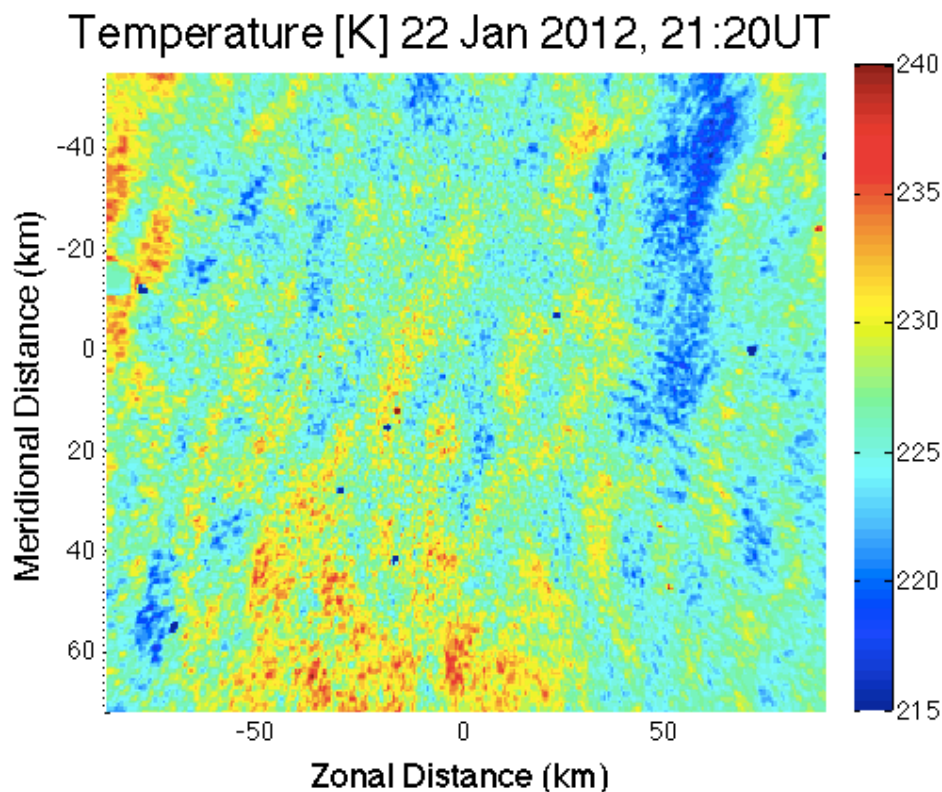


Figure 3.4: AMTM measurement without aurora or auroral effects

Detector Noise

The detector itself can contribute to noise which can impact temperature measurements. While this effect is small, it still limits precision on AMTM temperature measurements. This noise has been modeled as white noise with standard deviation of 1K, and this is shown in figure 3.5. Additional noise can be observed within the AMTM, which is not instrument dependent. This is noise due to turbulence within the atmosphere and is described in the following section.

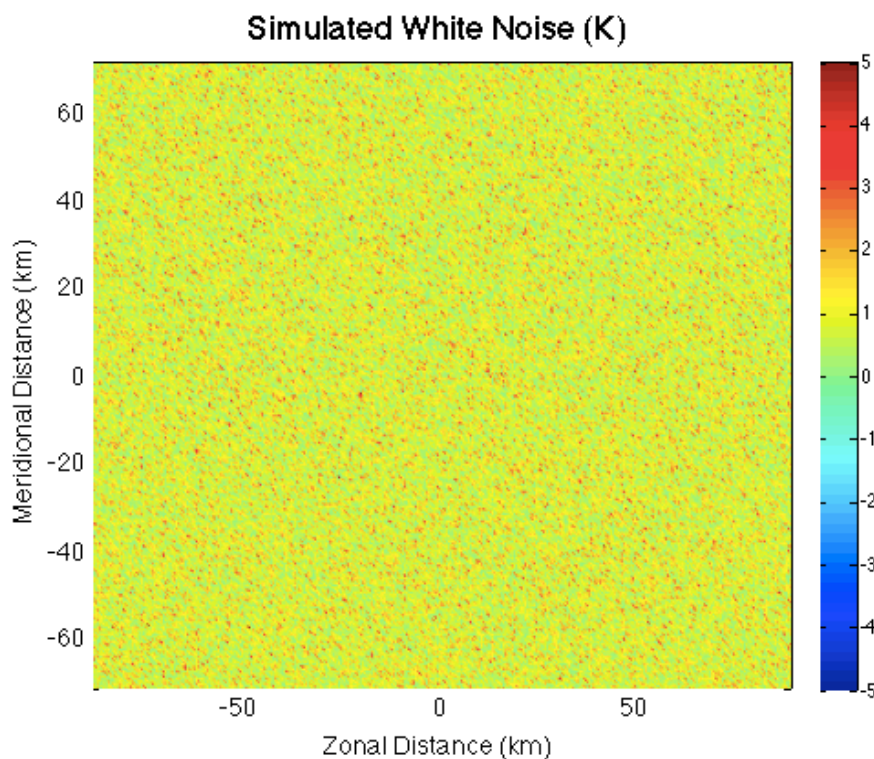


Figure 3.5: A simulation of detector noise as would be seen by the AMTM

Atmospheric Noise

Temperature deviations in the MLT region may also occur due to turbulence within this region. This turbulence creates a spectrum of noise known as an Kolmogorov spectrum. This noise can be modeled as $\sim k^{-5/3}$ spectrum, where k is a wavenumber. [Tennekes and Lumley, 1972].

OH Layer Averaging

Emissions observed by the AMTM are averaged over the OH layer. Thus, GW temperatures measured by the AMTM are weighted by the shape of the OH layer, and there is often a cancellation effect depending on the wavelength of the GW. This issue is discussed more in [Hickey and Yu, 2005]. Errors can arise in correcting for averaging that takes place over the OH layer given the background winds and chemistry, and the intrinsic parameters of the GW.

Additionally, the actual shape of the OH layer is often times unknown, and this adds uncertainty to temperature averaging corrections as well.

3.1.1b AMTM Measurement Capabilities

In addition to the rectangular 144 km x 180 km spatial temperature map as shown in Figure 3.2, the AMTM can also provide OH(3,1) P1(2) intensity images. While these do not provide a direct temperature measurement, they provide an image with less noise, less temporal averaging, and the ability to detect very small-scale dynamics and instabilities. Additionally, individual images at each time frame can be used to generate a keogram. Lines intersecting zenith in the north-south and east-west directions from each AMTM image at each successive times can be put together to form a single keogram image depicting wave activity over a given time period. A depiction of how to obtain a keogram is given in figure 3.6. The observations from the AMTM in both a stationary ground position and aboard the Gulfstream V plane used in the DEEPWAVE campaign are discussed in the following sections.

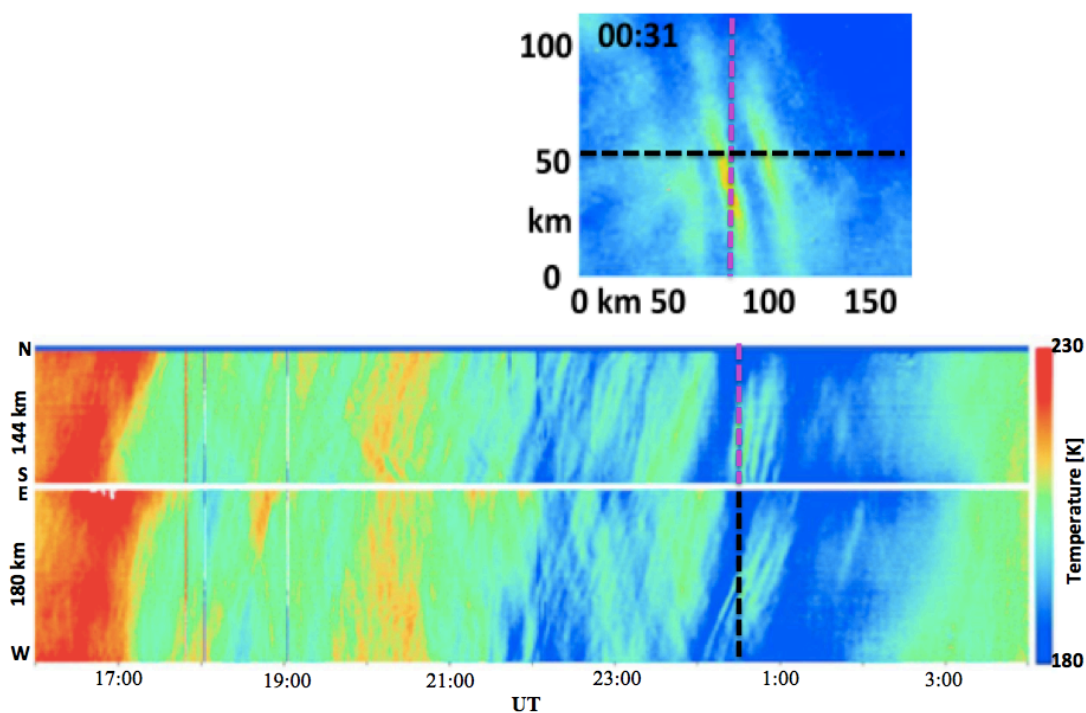


Figure 3.6: A keogram is shown in the bottom, and corresponding AMTM image for a given time is shown on the top. Lines through the image depict the north-south and east-west lines of data used in the keogram. Images from [Fritts *et al.*, 2014].

DEEPWAVE Measurements

DEEPWAVE allowed for spatial temperature maps to be generated in time rather than a stationary map depicting gravity waves and dynamics passing over a given area. Keograms can similarly be generated over a map. An example of this from [Bossert *et al.*, 2015] is shown in Figure 3.7. These flight-based keograms allow for GW hotspots and stationary mountain waves to more readily be observed.

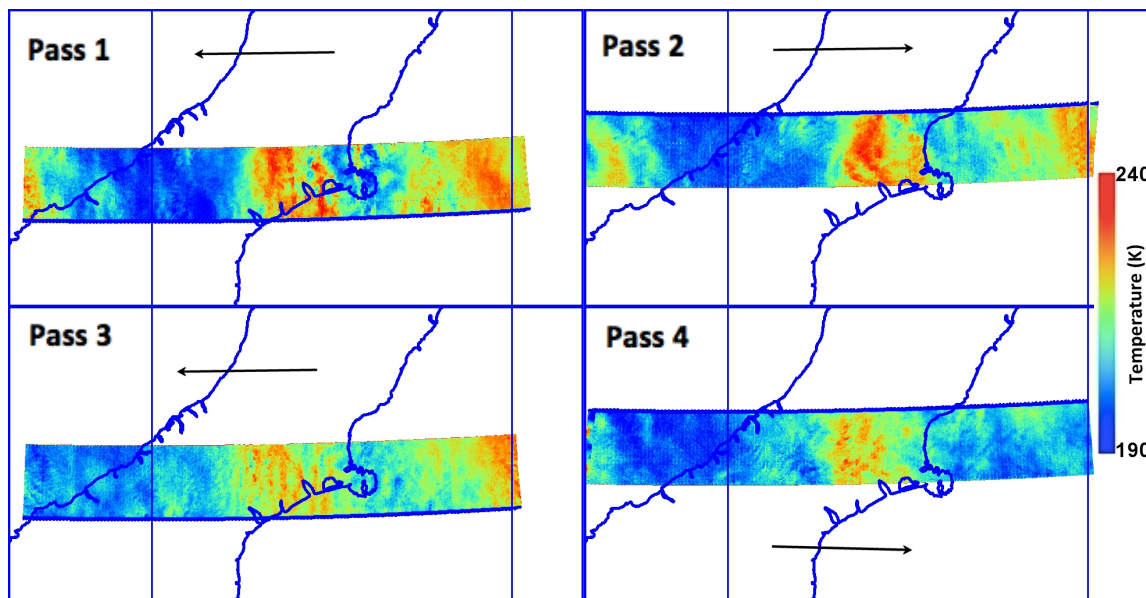


Figure 3.7: Spatial keograms from the DEEPWAVE flight on July 13, 2014 depict a stationary large-scale mountain wave, that would otherwise be undetected in a ground based instrument.

3.2 Sodium Lidar

The type of lidar system used in these studies in conjunction with the AMTM is called sodium resonance fluorescence lidar. This lidar utilizes the D2a line of sodium to measure winds, temperatures, and sodium densities from ~80-105 km. The theory for sodium lidars has previously been developed, and is directly applicable to the research provided in this dissertation. The ALOMAR sodium lidar analysis uses the previously existing CSU lidar analysis code, which is based on the equations and theory discussed in the following sections. However, the DEEPWAVE sodium lidar analysis code was written at GATS, inc. as part of this dissertation research. The equations and theory discussed below are directly used in the analysis methods.

3.2.1 Sodium Fluorescence Lidar Theory

Sodium lidar measurements can be described using the fundamental lidar equation, which quantifies the return photon counts from a lidar pulse. This is given by equation 3.1. The return

photons are dependent on the atmospheric path to and from the sodium atoms, the sodium scattering cross section, and the receiver. The parameters of this equation are further described in appendix B.

$$N_s(\lambda, z) = (N_{trans}) * (\sigma(\lambda_{up})n\Delta z) * \left(\frac{A}{4\pi z^2}\right) * (\eta \cdot T_a^2(\lambda)E(\lambda_{up})E(\lambda_{down})G(z)) + N_B\Delta t \quad (3.1)$$

The transmitted number of photons can be calculated using the laser power using equation 3.2.

The parameters of this equation are further described in appendix B.

$$N_{trans}(\lambda) = \frac{P_L(\lambda) * \Delta t}{(h * c) / \lambda} \quad (3.2)$$

The sodium scattering cross section is derived from 6 main absorption lines in the D2 transition of the sodium atom [She and Yu, 1995]. A diagram of these lines is given in Figure 3.8. A corresponding table of intensities is available Appendix B. Using the 6 sodium D2 lines, the sodium scattering cross section can be obtained. The equation for the sodium cross section is given in equation 3.3 and a description list of the corresponding variables is given in Appendix B.

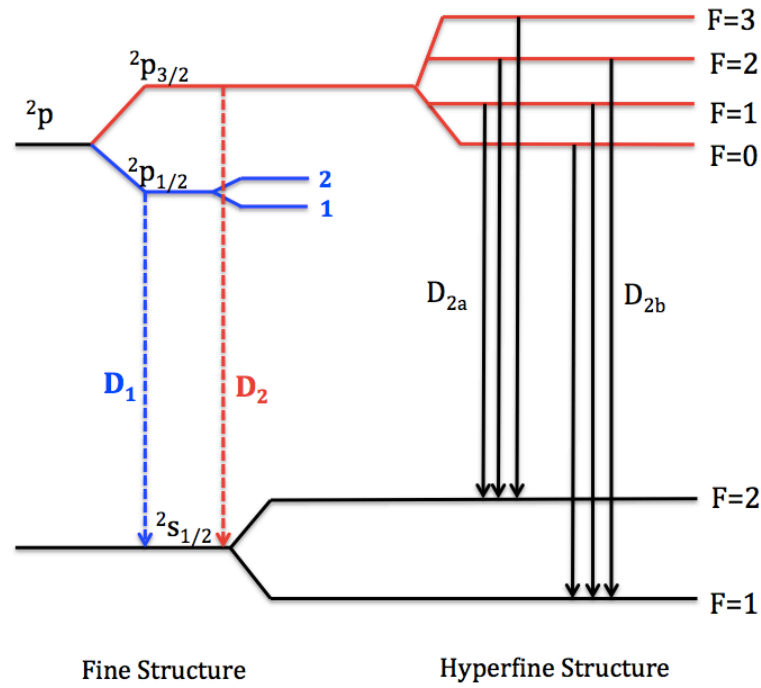


Figure 3.8: Diagram of sodium hyperfine structure

$$\sigma_{na}(v, T, V_R, \Omega) = \frac{1}{\sqrt{2\pi}\sigma_D} \frac{e^2 f}{\epsilon_0 m_e c} \sum_n \left(g_n q_n(\Omega) \cdot \exp \left(- \frac{\left[v_n - v \left(1 - \frac{V_r}{c} \right) \right]^2}{2 \cdot \left(\frac{k_b T}{M \lambda_o} \right)} \right) \right) \quad (3.3)$$

The value for $q_n(180^\circ)$ has been calculated over ALOMAR previously [Fricke and von Zahn, 1985]. The value for $g_n q_n(180^\circ)$ is equivalent to the A_n value given in Table B.1 in Appendix B. Thus, equation 3.3 can be written in terms of backscatter cross section, which is given in equation 3.4.

$$\sigma_{na}(v, T, V_R, 180^\circ) = \frac{1}{\sqrt{2\pi}\sigma_D} \frac{e^2 f}{\epsilon_0 m_e c} \sum_n \left(A_n \cdot \exp \left(- \frac{\left[v_n - v \left(1 - \frac{V_r}{c} \right) \right]^2}{2 \cdot \left(\frac{k_b T}{M \lambda_o} \right)} \right) \right) \quad (3.4)$$

The use of equation 3.4 to obtain winds, temperatures and sodium densities is discussed in the following sections.

3.2.2 Sodium Density Retrieval

Sodium densities can be obtained by comparing or normalizing lidar photon returns to photon returns at a Rayleigh scattering altitude where the density is known. The equation for normalized counts is given by equation 3.5. The equation for calculating sodium density from these normalized counts is given by equation 3.6.

$$N_{norm}(f) = \frac{N_{Na}(f)}{N_{Ray}(f) * E(f) * E(f_{down})} \quad (3.5)$$

$$n_{Na}(z) = \frac{N_{norm}(f, z)}{\sigma(z)} 4\pi n_{Ray}(z_{Ray}) \sigma_{Ray} = \frac{N_{norm}(f, z)}{\sigma(z)} 4\pi * (2.938e - 32) \frac{P(z_{Ray})}{T(z_{Ray})} \frac{1}{\lambda^{4.0117}} \quad (3.6)$$

In addition to being used in the calculation for sodium density, the Rayleigh normalized photon counts are also used to calculate winds and temperatures. This is discussed in the following section.

3.2.3 Sodium Wind and Temperature Retrieval

The sodium scattering cross section given in equation 3.4 will change with temperature. Higher temperatures cause the scattering cross section Doppler broadening, and radial winds cause Doppler shifts to occur. Figures 3.9 and 3.10 demonstrate the effects of temperature Doppler broadening and wind Doppler shifting on the sodium scattering cross section.

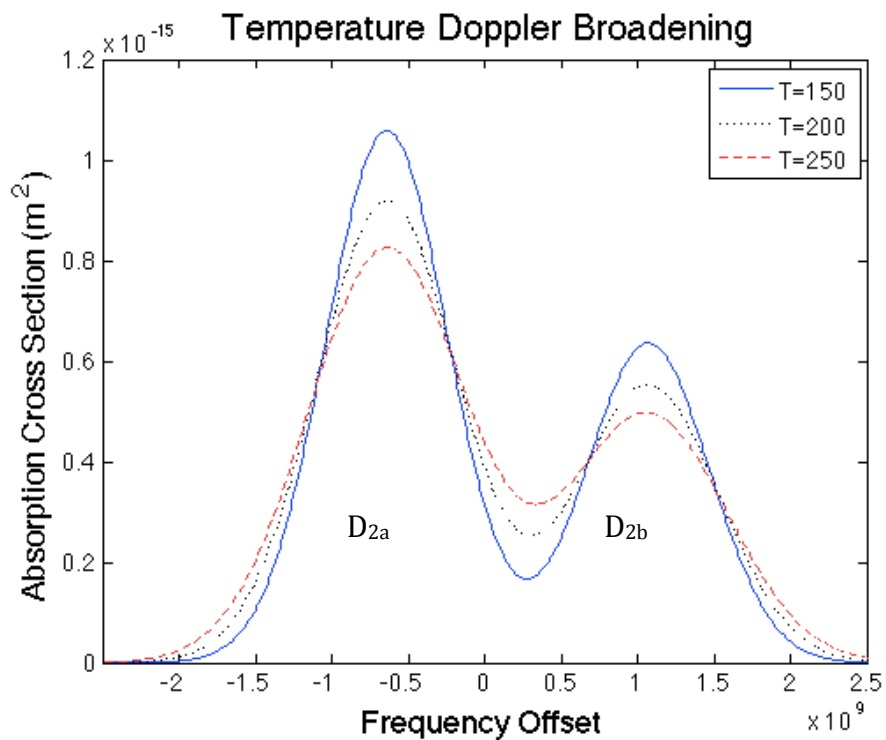


Figure 3.9: Na absorption cross section plotted for different temperatures

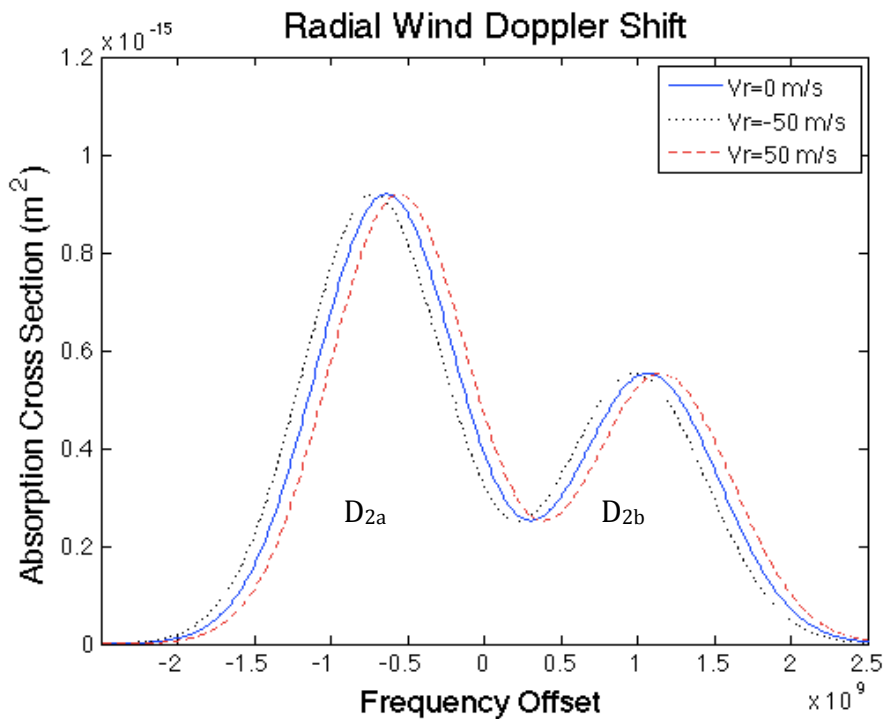


Figure 3.10: Na absorption cross section plotted for different radial winds

Utilizing ratios of two or more frequencies, the measured absorption cross section can be related to a specific radial wind and temperature [Papen, 1995]. A lookup table can be created in terms of ratios for specific winds and temperatures. Ratios of the frequencies measured from the sodium lidar can then be used with the lookup table to determine corresponding winds and temperatures. The ratios used to determine temperatures and winds for the three frequency sodium lidar setup are given in equations 3.7 and 3.8. An example of a corresponding lookup table is given in Figure 3.11.

$$R_r = \frac{N_{norm}(f_+) + N_{norm}(f_-)}{N_{norm}(f_{center})} \quad (3.7)$$

$$R_w = \frac{\log(N_{norm}(f_+) / N_{norm}(f_-))}{\log\left(\frac{(N_{norm}(f_+) * N_{norm}(f_-))}{(N_{norm}(f_{center}))^2}\right)} \quad (3.8)$$

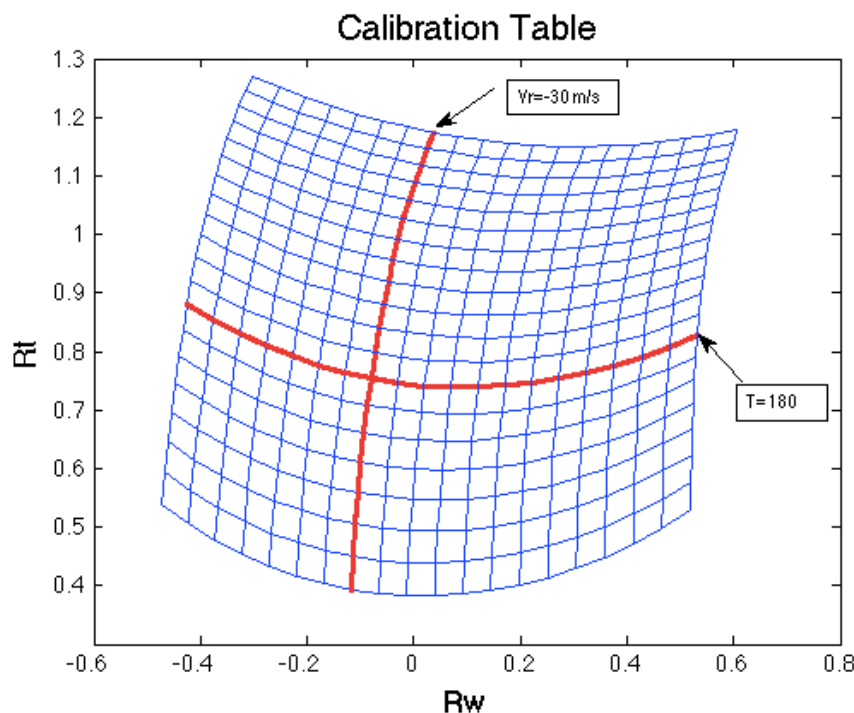


Figure 3.11: Frequency lookup table

3.2.4 Weber Sodium Lidar

The Weber sodium lidar [She *et al.* 2002] is a resonance fluorescence lidar located at the ALOMAR observatory on northern Norway (69° N, 16° E). The lidar system gives dependable winds, temperatures and sodium densities from ~80-105 km during the Arctic winter months with resolutions of as little as 5-10 minutes and 1 km for temperatures and winds, and 1 minute and 150 m for sodium densities. The lidar system uses a sum frequency generator (SFG) to produce about 50 mW of 589 nm light at the sodium D2a resonance line. The frequency is tuned using a sodium vapor cell with Doppler free saturation spectroscopy [She *et al.* 1992]. This light is sent through acousto-optic modulators (AOM) to shift between the center frequency of the D2a line at 589.189 nm and two up and down shifted frequencies at ± 630 MHz. These three frequencies allow for the theoretical shape of the D2a line to be calculated, providing radial wind and temperature estimates as described in section 4.3. When the lidar beams are tilted off-zenith, zonal and meridional components of the wind field can be obtained by suitable averaging in time.

The CW light from the SFG and AOMs is sent through a pulsed dye amplifier (PDA) pumped with a Spectra-Physics Nd:YAG laser. Until the end of 2012, this laser pulsed at 50 Hz. However, it has since been adjusted to 30Hz in order to sync with the existing RMR lidar at ALOMAR. The emitted PDA pulses have a full-width-half maximum (FWHM) duration of 6.7 ns and a FWHM linewidth of 130 MHz. The emitted power is about 400 mW. The outgoing beam is expanded to a size of 20 mm with a divergence of 0.5 mrad. This leads to a sampling area size of about 40 m in diameter at 80 km when the beam is pointed at zenith.

The return photons are collected using two 1.8 m diameter IAP telescopes. These telescopes can be steered up to 30° off zenith. The returns are counted using Hamamatsu

photomultipliers. A chopper removes low altitude returns to prevent saturation. The range bin size for a beam configured at zenith is 150 m. The system shifts between each of the three frequencies and remains at 5 s at each frequency, allow for a minimum integration time of 15 s.

System diagrams for the transmit side of the lidar and the receiver side of the lidar are given in Figures 3.12 and 3.13 respectively.

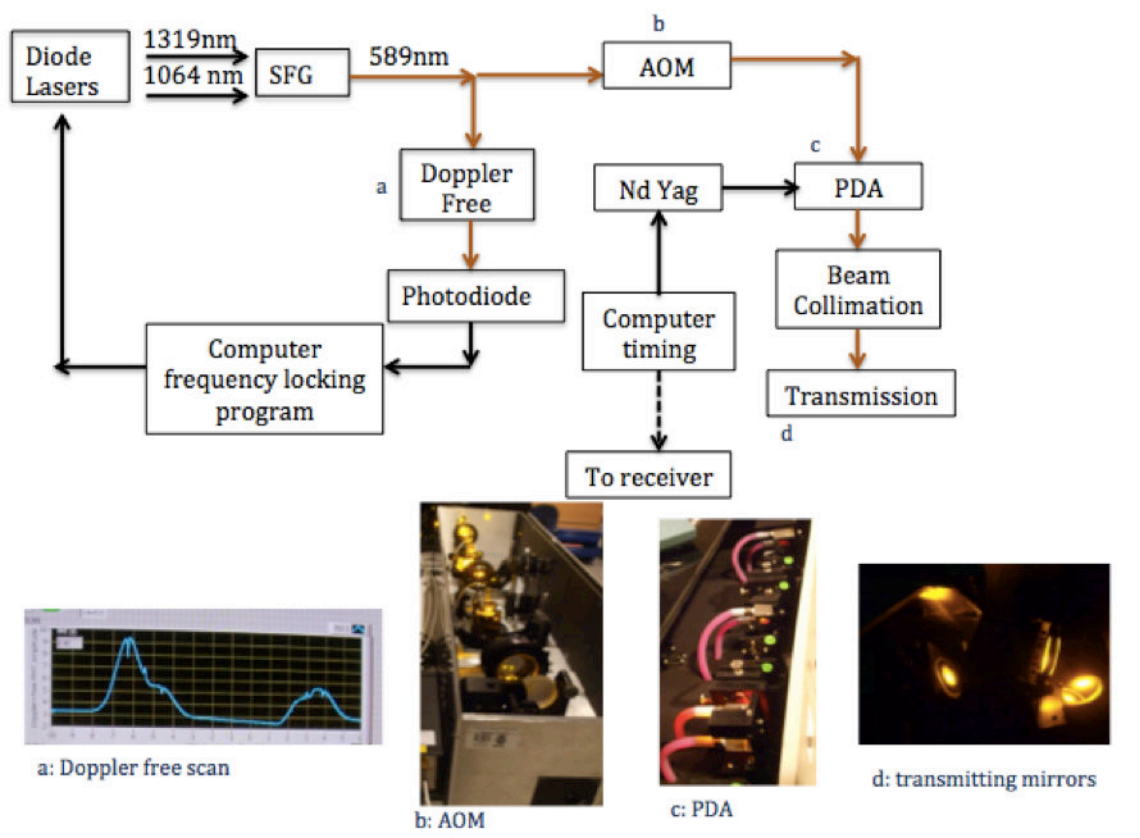


Figure 3.12: A system overview of the lidar transmitter

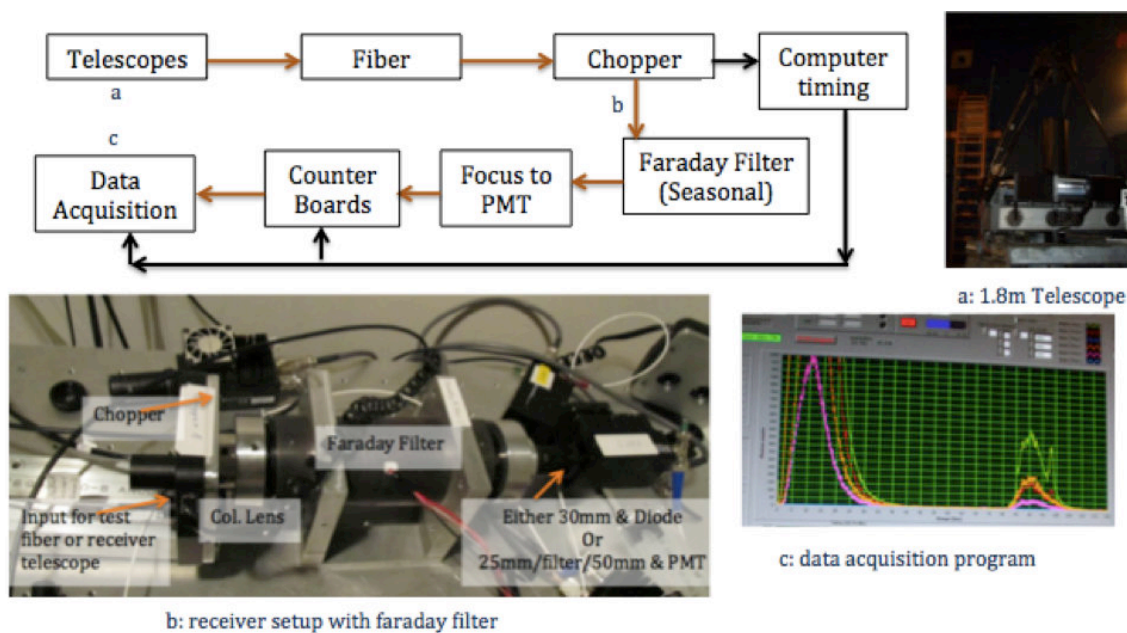


Figure 3.13: A system overview of the lidar receiver

3.2.5 DEEPWAVE Sodium Lidar

Unlike the Weber Sodium Lidar at ALOMAR, the DEEPWAVE sodium lidar was designed using a CW laser having a primary wavelength at the sodium D2a line. This lidar has two beams that scan or pulse the CW beam to yield higher power or shorter pulses allowing for improved range resolution respectively. The research discussed in this thesis utilized the pulsed beam, so this lidar method will be discussed here.

The light for the pulsed beam was pulsed using an AOM, resulting in an effective pulse length of 3 km. The laser operated in either a single or dual frequency mode during the duration of the DEEPWAVE campaign. In the two-frequency mode, the laser was switched between each frequency every 12 s. Densities were calculated assuming a constant background temperature that was obtained from averaged AMTM measurements. Temperatures were calculated utilizing a two-frequency lookup table assuming that vertical winds were zero. Measurements using only

one frequency (density only) resulted in a spatial resolution of ~6 km. Measurements using two frequencies resulted in spatial resolution of ~18 km.

The following subsections discuss the errors associated with the specific DEEPWAVE sodium lidar and instrument-specific assumptions. In order to calibrate the instrument and determine the potential errors due to the pulse length averaging and two-frequency temperature measurement, model output from a nonlinear, compressible, 2D model of time dependent GW propagation developed by Dr. Jonathan Snively and applied by Dr. Chris Heale was used. Two situations are shown for calibration purposes, which include a large-amplitude propagating GW and a breaking GW. The winds and temperatures for these two cases are shown below in the panels in Figure 3.14.

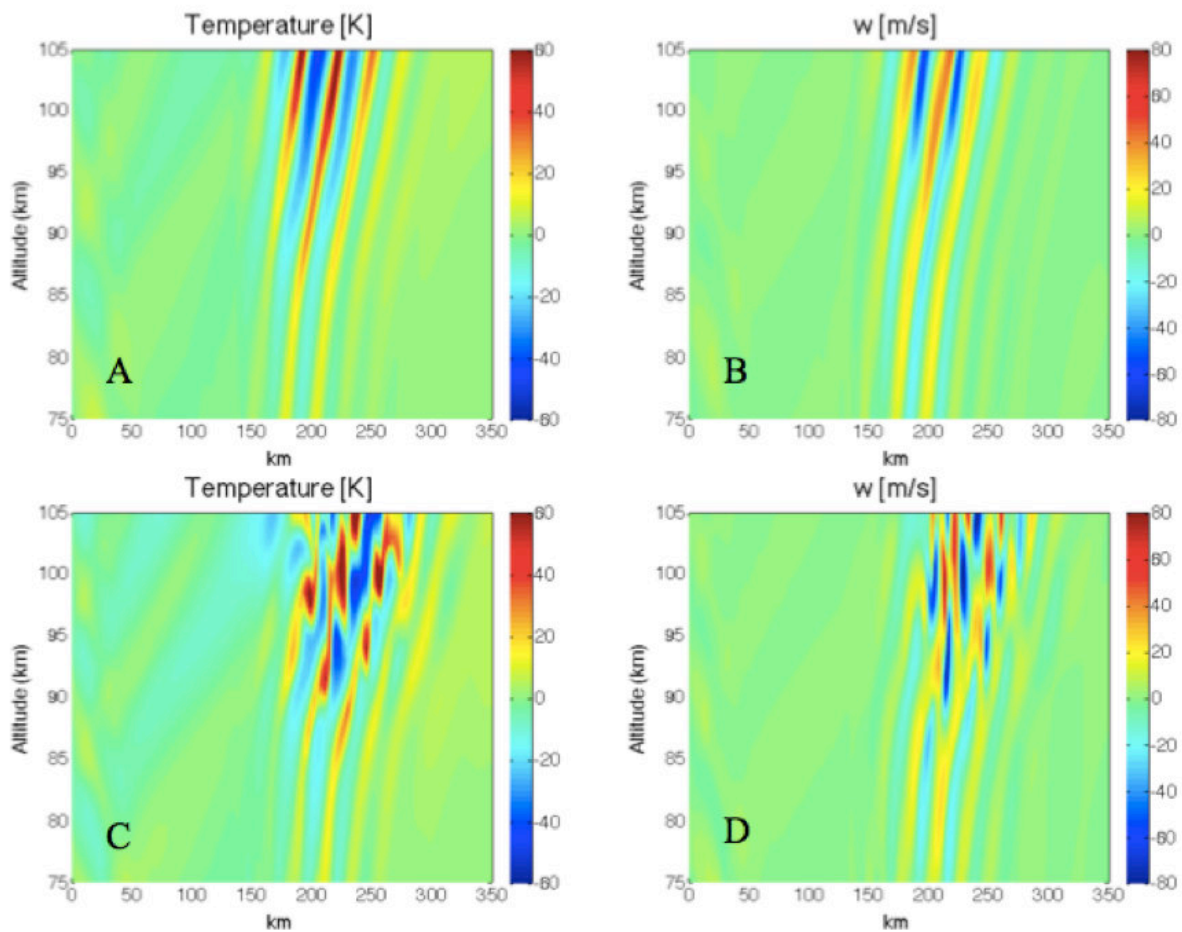


Figure 3.14: Simulation output of large-amplitude wave temperatures and winds are shown in plots A and B. Simulated output of breaking wave temperatures and winds are shown in plots C and D.

Pulse Effects

The equivalent pulse length in altitude is 3 km. This pulse has a sharp edge, allowing for vertical features to more clearly be defined. Essentially the returns from the DEEPWAVE sodium lidar represent a convolution of atmospheric features and the pulse shape. Thus vertical features of less than 3 km are still able to be defined. However, there are larger errors associated with features that have less than a 3-km scale. This calibration test shows the error between the actual temperature and what is measured with the 3-km pulse for both the large-amplitude wave and the breaking wave. The results are shown in Figure 3.15.

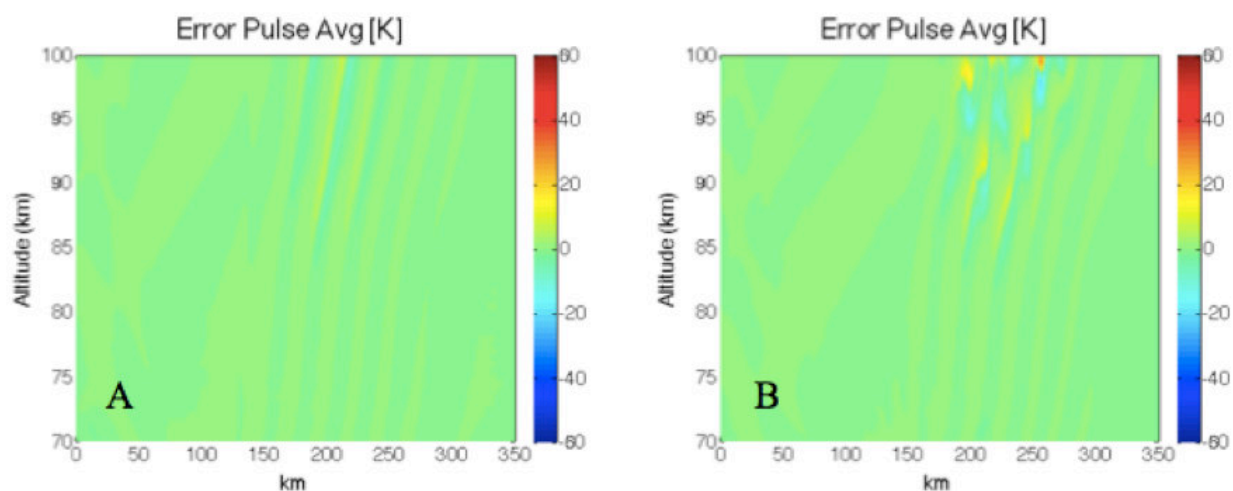


Figure 3.15: Error due to 3 km pulse averaging. Plot A shows pulse averaging error for the large amplitude GW and plot B show the pulse averaging error for the breaking GW.

Vertical Wind Effects

In order to calculate the temperature using only two frequencies, assumptions must be made about the vertical wind. Over large intervals of time, the vertical wind in the atmosphere is on average $\sim 0 \text{ ms}^{-1}$. However, the effects of vertical wind perturbations due to GWs can be quite significant on short time scales. For an ideal propagating GW that is well-resolved in time by the lidar measurements, the assumption that vertical winds are near zero may only have a small effect on the phase of the measured GW and not on the temperature amplitude, as wind and temperature are in quadrature for propagating GWs following the polarization relations (e.g. equation 2.18). However, as GWs break, they become nonlinear, and various effects may arise that can contribute to large measurement errors. The following simulations shown in Figure 3.16 address these potential errors. These errors are slightly larger in magnitude than the pulse averaging errors and are generally biased towards either warmer or cooler temperatures depending on the direction of the second frequency (+/-) used from the peak frequency.

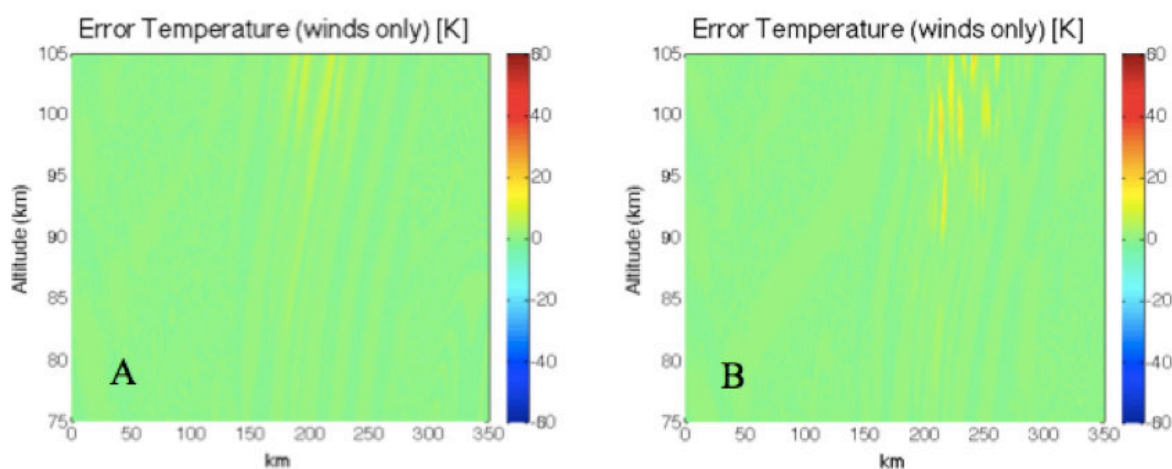


Figure 3.16: Error due to vertical wind $\sim 0 \text{ ms}^{-1}$ assumption. Plot A shows the error for a large amplitude wave and Plot B shows the error for a breaking wave.

Combined Pulse and Wind Errors

Combining these error sources a total instrument specific error is obtained. These combined error plots are given in Figure 3.17. It is important to note that these error measurements are wave amplitude dependent, and should thus be discussed in percentage error. For comparison, line plots at 100 km are given for comparison in Figure 3.18. These measurement errors are ~5-10% and generally less than 10%. Additionally, the predicted measurement correctly characterizes the observed wave field, placing more confidence on actual measurements.

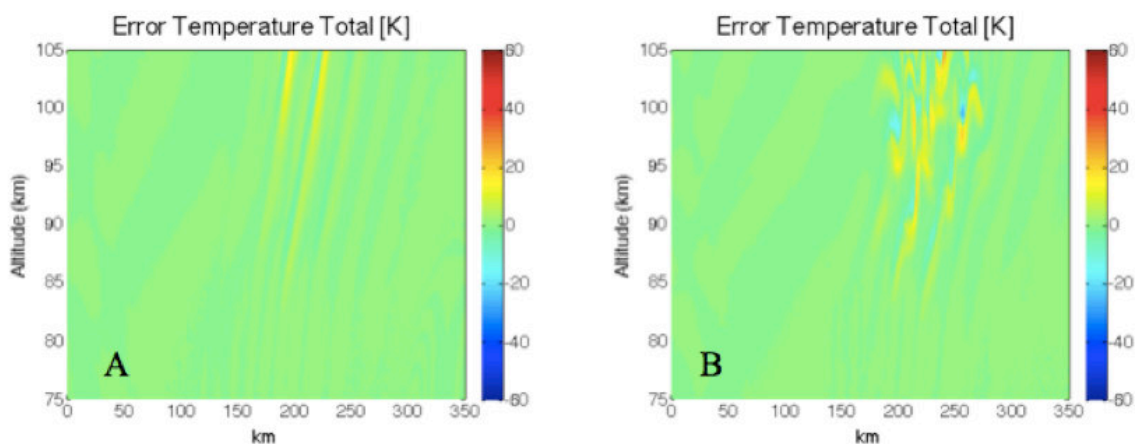


Figure 3.17: Combined DEEPWAVE instrument specific errors. Plot A shows the total errors for the large amplitude wave and Plot B shows the total errors for the breaking wave.

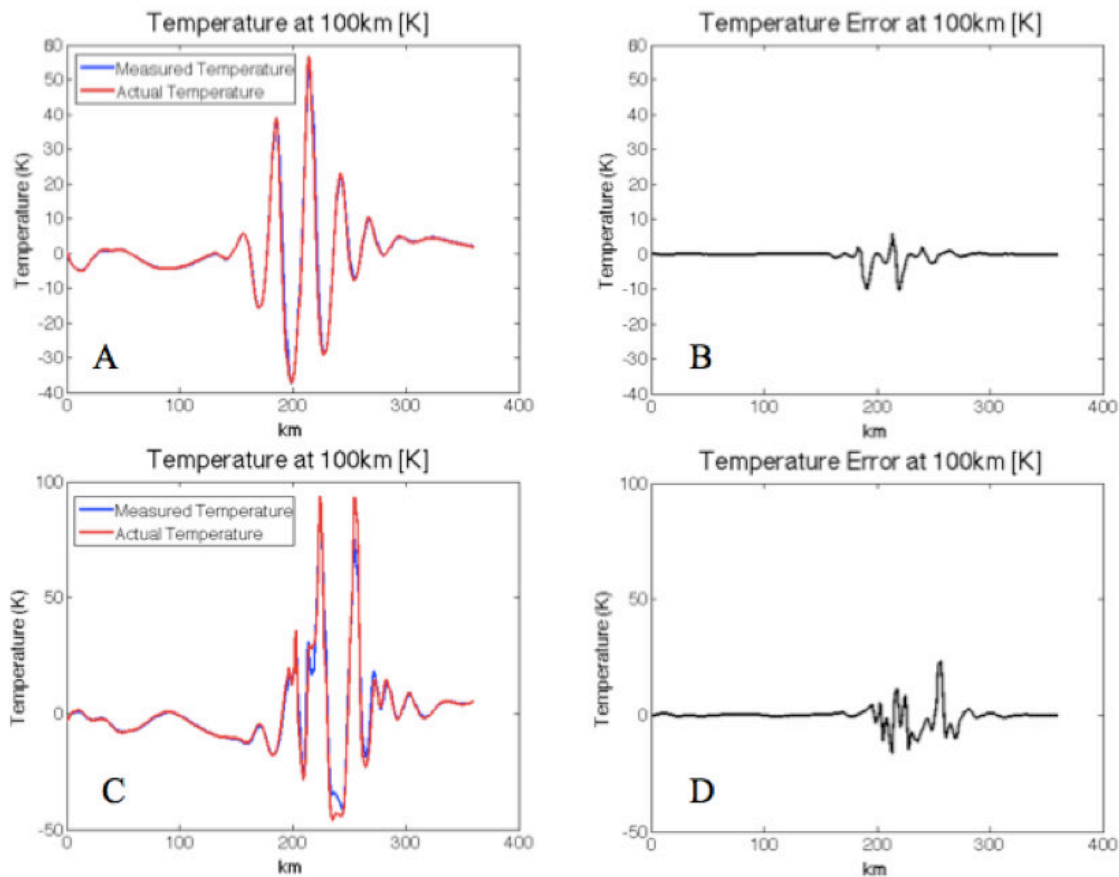


Figure 3.18: Predicted measured versus actual modeled temperature and the associated temperature errors at 100 km. Plots A and C show the measured and actual temperatures for the large amplitude and breaking waves. Plots B and D show the associated temperature error at 100 km.

Timing Errors

Of importance to the DEEPWAVE mission is the timing associated with measurements. This is especially due to the high aircraft speed resulting in a fast spatial coverage. For the measurements taken during the research flights, frequencies were switched for sodium between f_0 and f_1 every 12 seconds. This means a 3 km difference between the frequency measurements. Here, an extreme case is given for the implications of this timing on high-resolution measurements using a ~ 40 km GW example output from the same model previously used for the

above calibration examples. The densities and temperatures for this simulation are shown in Figures 3.19 and 3.20 respectively.

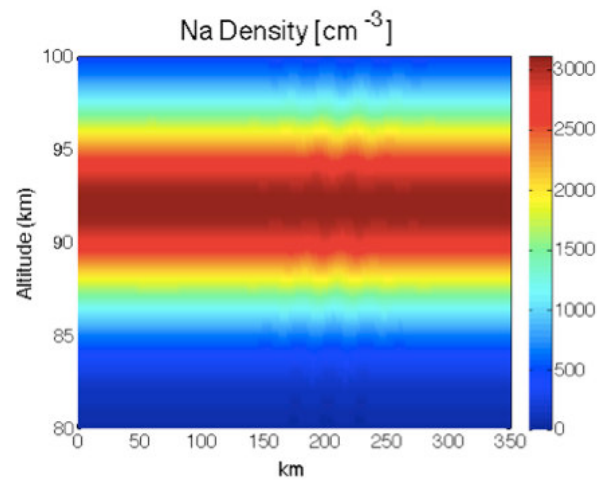


Figure 3.19: Sodium densities for a low amplitude ~ 40 km horizontal GW

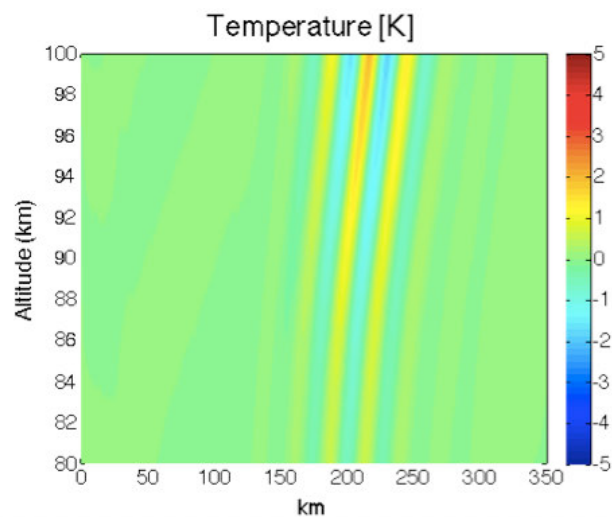


Figure 3.20: Temperature perturbations for the simulated ~ 40 km horizontal GW

For measurements that have been offset by 3 km, the measured density by f_1 and f_0 will differ. To examine the effects on temperature retrieval, three ratios were calculated and these are shown in Figure 3.21. Plot A gives the ratio F_1/F_0 solely based on scattering cross section due to winds and temperatures. Plot B gives the ratio between the sodium density measured by frequency 1 3 km ahead of frequency 2. Plot C gives the corrected ratio that accounts for this sodium density difference. The ratio in plot C is what would be measured by return photons. While the difference in sodium density is only a few percent, this has a large effect on the ratio of normalized counts measured by the lidar that is used to calculate the temperatures. Furthermore, this effect is more pronounced at the edges of the layer where the percent density perturbations relative to the background sodium are largest. The corresponding temperature measurements with comparison to the original temperatures are given in Figure 3.22.

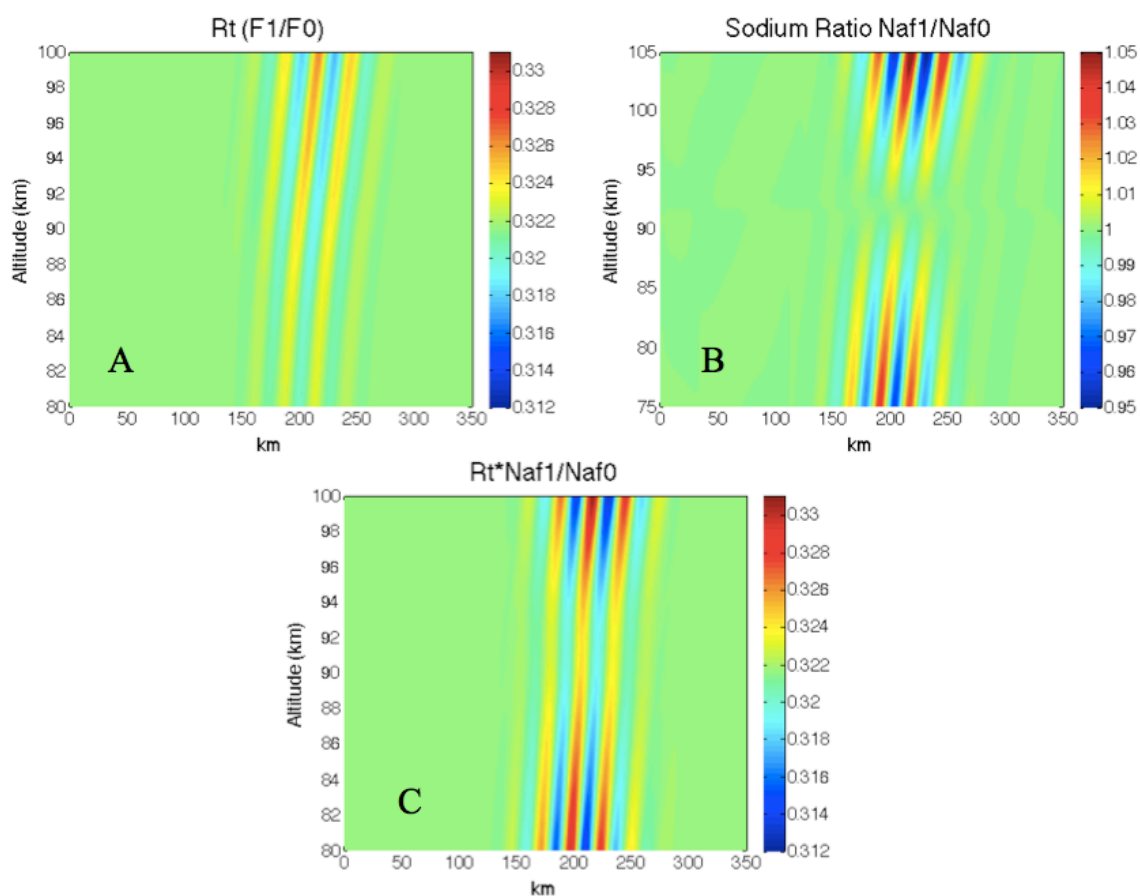


Figure 3.21: Plot A shows the simple ratio of the scattering cross sections for F1 and F0 based on the winds and temperatures measured alone. Plot B gives the ratio of sodium densities measured at the two different averaging times for F1 and F0. Plot C shows the corrected ratio accounting for the difference in sodium densities and scattering cross sections as would be measured by return sodium counts along a flight track.

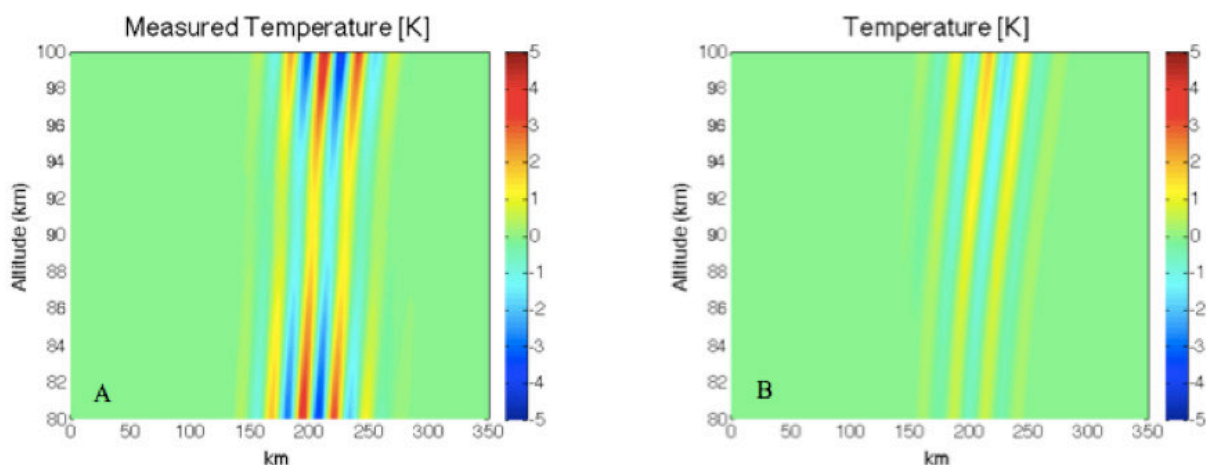


Figure 3.22: Plot A shows the measured temperatures for a timing offset resulting in a 3 spatial measurement difference for each frequency for a 40 km horizontal GW. Plot B shows the actual temperature perturbations of the 40 km horizontal GW.

The largest temperature errors take place at the bottom of the sodium layer. Towards the center of the layer, the temperature errors are minimal due to this potential measurement timing effect. It should be noted that this demonstrates a case with no averaging for a small horizontal scale GW at the edge of detectable resolution for the DEEPWAVE mission. Additionally, it may be possible to mitigate these errors, especially for larger horizontal scales, by fitting the background density and accounting for the density differences measured by each frequency.

The errors discussed above do not include typical lidar error sources. The following section discusses errors that can arise with any sodium lidar and are not necessarily specific to one instrument.

3.2.6 Lidar Sources of Error and Noise

This section discusses some of the errors that can arise with the lidar system setup and data analysis.

Telescope Overlap

The telescope overlap function at ALOMAR has been calculated for both of the larger IAP 1.8m telescopes as well as the smaller telescope that is positioned at 20° West. The calculated overlap function was done assuming a Gaussian beam shape. Figure 3.23a shows the overlap function for the 1.8m telescope using a 0.6mrad field of view. Figure 3.23b shows the overlap function for the smaller 0.5m 20° W telescope with a 0.5mrad field of view. Both cases assume a beam divergence of 0.5mrad and a distance between the transmitted beam and telescope of 2.2m. With the new telescope setup in the process of being implemented, the west beam and west telescope will have a separation of less than 1m. However, the data presented in this thesis was taken using the 2.2m separation between the beam and telescope.

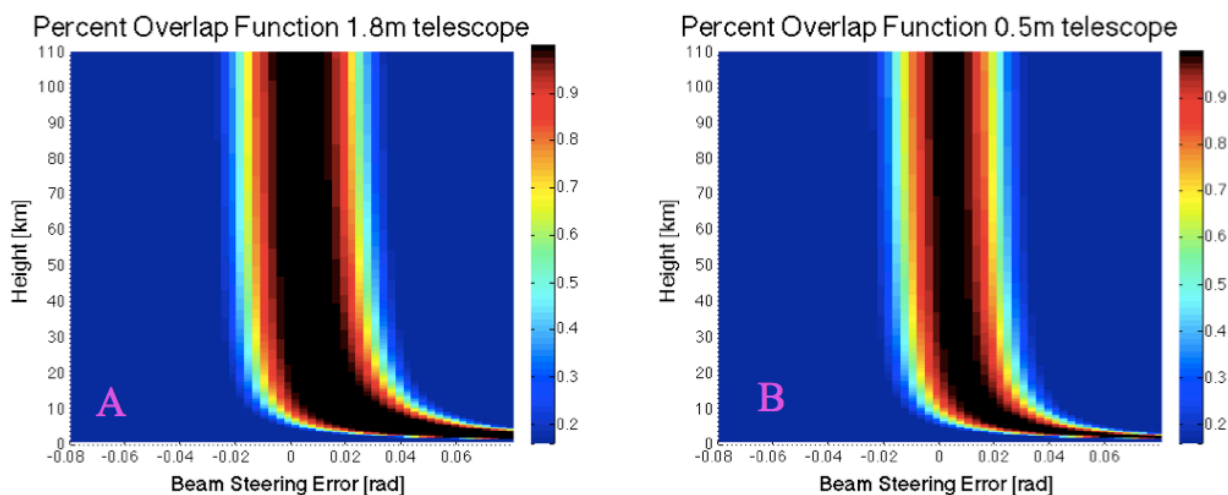


Figure 3.23: Plot A shows the 1.8m telescope overlap function and plot B shows the 0.5m telescope overlap function

The telescope overlap functions show that the beam can be aligned with the telescope for 100% overlap even if there is a slight offset in beam steering. One issue to take into account is that there may be apparently reasonable overlap at 20-40 km, but if there is a larger error in beam

steering, the percentage overlap at higher altitudes would be less than at lower altitudes. This would cause errors in Rayleigh normalization, which will be discussed in the following section.

Rayleigh Normalization

Sodium densities are obtained from normalized photon counts as given in equations 3.9 and 3.10. Since the density calculation is dependent on photon returns from Rayleigh altitudes, any errors in these returns can cause errors in sodium density calculations. As seen in figures 3.14 and 3.15 in the above section, errors resulting from telescope overlap can contribute to 10-20% overlap offset if using Rayleigh normalization near 30 km. While this will cause errors in the sodium density calculation, this can also result in temperature errors due to incorrect extinction correction. This will be discussed in the following section.

Another source of constant offset error can be in the densities used for Rayleigh normalization. The density in the Arctic stratosphere fluctuates throughout the year. According to the basic MSIS model, the density near the Rayleigh normalization altitudes (~32 km) can vary by 50% between the winter and summer. Furthermore, events such as stratospheric warmings can perturb the density from what MSIS may predict. For this reason it is important to recognize the time of year as well as other events which may cause changes in the density at Rayleigh normalization altitudes.

Another factor in Rayleigh normalization is the noise that normalization can introduce to data at the sodium layer altitude. While normalization should be chosen at an altitude about aerosols (which can cause Mie scattering) and above altitudes at which the chopper is still opening or the beam is not fully overlapped with the telescope, higher altitudes present the issue of signal to noise. Care must be taken to choose a normalization altitude with sufficient signal to noise to avoid introducing significant errors into the data.

Extinction Correction

As light travels through the sodium layer, photons are lost due to absorption. This is dependent on the density of the sodium layer, and when extinction is not accounted for, it appears that fewer photons are returned from the upper side of the layer. This becomes problematic when calculating temperatures as the three frequencies used to calculate the temperature ratio are not absorbed at the same rate. Thus, the temperature calculated will be warmer than the actual temperature within the layer. This can be demonstrated using the absorption cross section of sodium which is shown in figure 3.24. The three frequencies used for the calculation of winds and temperatures are drawn as orange lines. It can be seen that these three frequencies will be absorbed differently through the sodium layer.

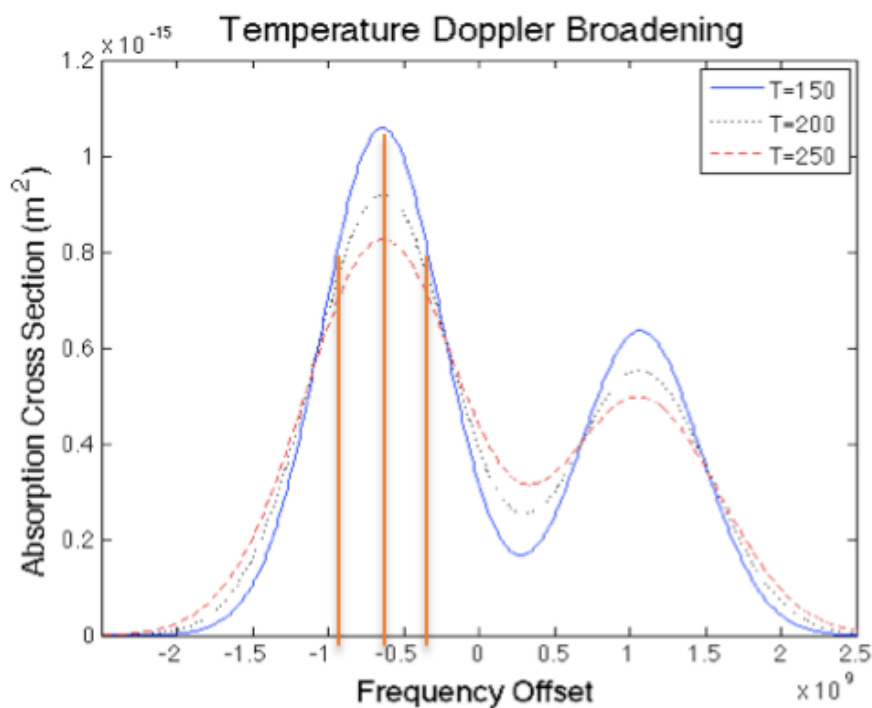


Figure 3.24: The three frequencies used for sodium lidar (shown in orange) correspond to different absorption cross sections

As shown in equation 3.9, extinction should be accounted for in the normalized counts at each frequency before generating a ratio of frequencies that can be used to calculate temperature. The extinction should be calculated for the transmitted frequency as well as the return extinction, which should be calculated for a range of frequencies that are all re-emitted by the sodium. The equations to calculate extinction are given by 3.9 and 3.10.

$$E_{up} = \exp\left[-\int_{z_{bot}}^z n_c(z)\sigma_{eff}^{Tot}(f)dz'\right] \quad (3.9)$$

$$E_{down} = \sum_{n=1}^{10} \left\{ A_n \exp\left[-\int_{z_{bot}}^z n_c(z)\sigma_{eff}^n(f)dz'\right] \right\} \quad (3.10)$$

To show the importance of extinction correction, data from a night in January 2012 is plotted showing the temperature difference between not correcting for extinction and correcting for extinction. This is shown in figure 3.25a. Figure 3.25b shows the cumulative column abundance of sodium with height for the corresponding night.

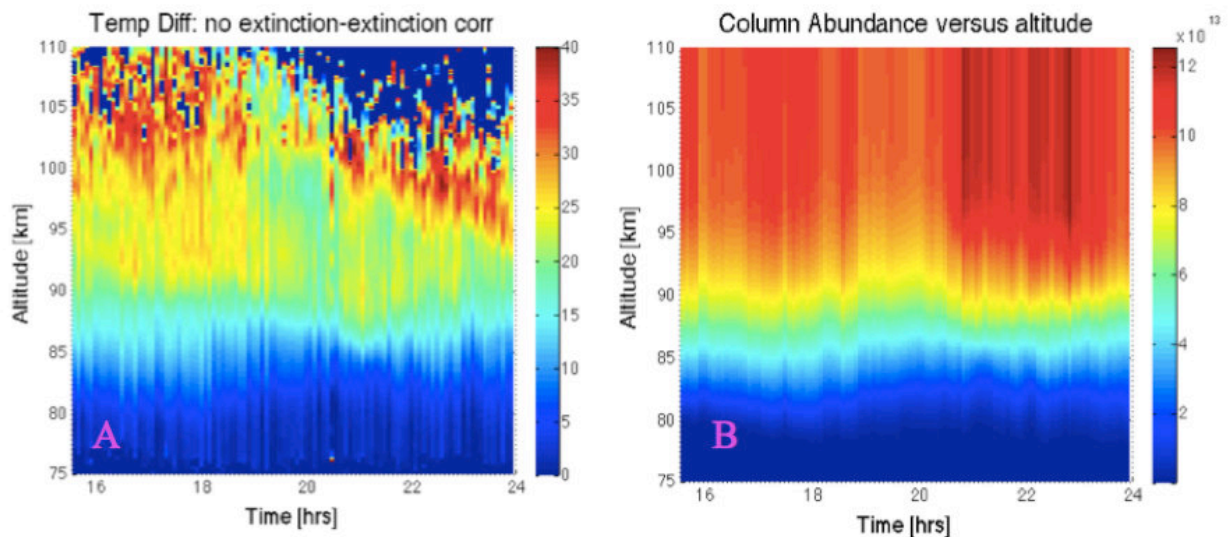


Figure 3.25: Plot A on the left shows the temperature error from no extinction. Plot B on the right shows the corresponding cumulative sodium column abundance at each altitude.

It is apparent from Figure 3.25 that not correcting for extinction can cause large errors in temperature measurements near the topside of the layer, especially on days/times where the sodium density is high, such as in the polar wintertime. This temperature offset can cause errors calculating the background environment stability when using calculations such as the buoyancy frequency.

3.3 Combined Sodium and AMTM measurements: An Overview

The AMTM provides a spatial view of GWs allowing for GW horizontal wavelengths and phase speeds, orientations, and packet durations to be easily obtained. Additionally, the AMTM provides direct measurements of GW amplitudes in temperature (with caveats, see below). The lidar provides vertical profiles of sodium densities, temperatures, and winds. Figure 3.26 gives an example of these measurements.

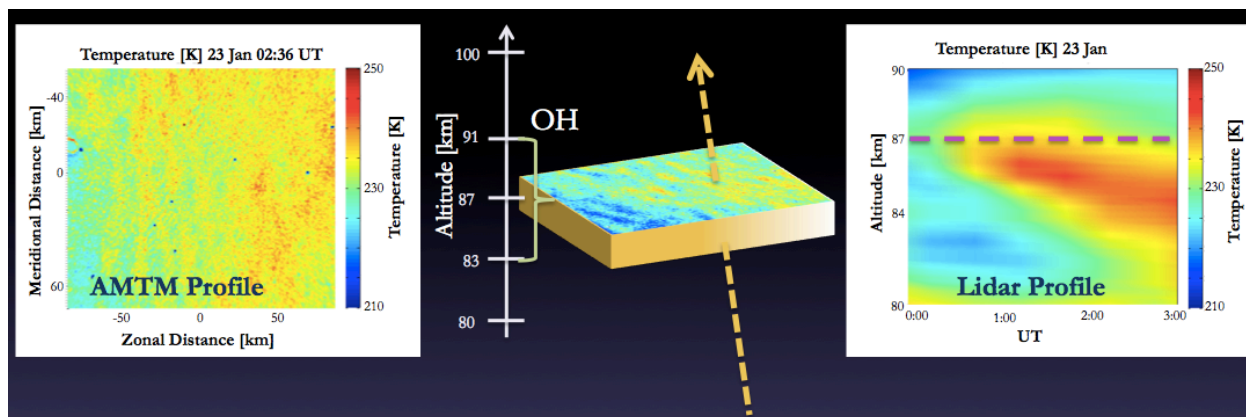


Figure 3.26: An overview of combined lidar and AMTM measurements.

Since the OH layer has an approximate Gaussian distribution with a typical full-width half-maximum of ~ 8 km, there is always averaging over the brightness distribution associated with the observations. Thus, the AMTM will only be sensitive to GWs observed in the sodium layer where there is an overlap with the OH layer. Figure 3.27 provides an overview of this overlap.

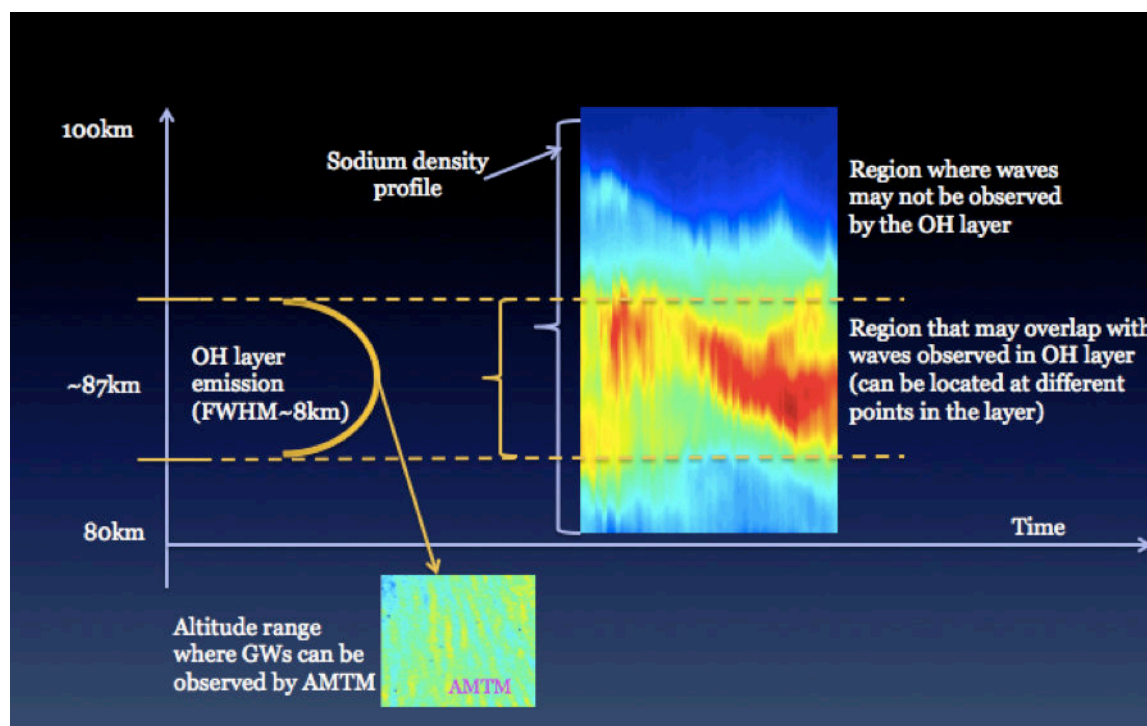


Figure 3.27: A diagram of sodium layer and OH layer overlap observations.

The OH layer shape and altitude can be approximated by weighting and averaging lidar temperatures over the approximate OH layer altitude and shape. Figure 3.28 shows an example of lidar and OH temperature matching for an OH layer altitude of 86 km and FWHM of 8 km.

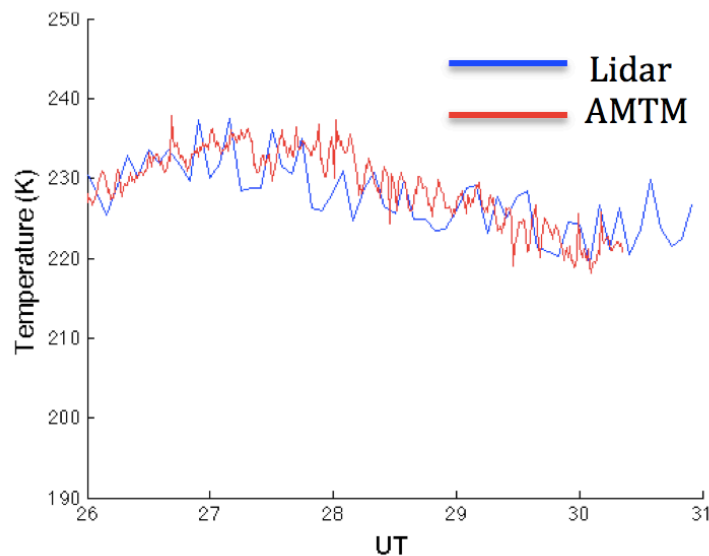


Figure 3.28: Lidar weighted temperature and AMTM temperature

The combination of the sodium lidar and AMTM provides a more complete capability for characterizing and quantifying GWs in the MLT region as these collective measurements provide all necessary parameters to calculate GW MF. The measurement suite includes vertical profiles of temperature and horizontal wind as well as direct measurements of the GW temperature perturbation, horizontal wavelength, and ground-relative phase speed. The following sections discuss the research performed using these instruments allowing for studies of small-scale GWs, their propagation environments, and their influences on the MLT.

4. Gravity Wave Propagation Influences Due to Variable Background Environments

Multi-instrument measurement capabilities provided by combining a sodium lidar, the AMTM, and in some cases radar winds, allow for the identification of key GW dynamics. These observations and corresponding analysis provide an assessment of GW propagation and GW momentum transport, and their dependence on the background environment. Propagation environment strongly influences the impact the GW MF has within certain areas of the atmosphere, and studying this allows further insight into momentum deposition within the MLT. The following sections discuss measurement and characterization of small-scale GWs in variable propagation environments, multi-scale GW propagation environments, and critical levels that cause GWs to break in the MLT.

4.1 Small-scale GW propagation and characterization in variable environments

The larger-scale environment determines whether various spectra of GWs can be propagating, are ducted, or may be approaching a critical level. The polarization relations discussed in section 2 provide a means to use measured parameters to calculate various perturbation quantities. The methods for these calculations are discussed below and taken from [Bossert *et al.*, 2014].

Background Environment Parameters and calculations

Conditions under which GWs are freely propagating or ducted are calculated using the GW and mean parameters inferred from lidar and AMTM data for various events. To determine the propagation characteristics of observed GWs, the vertical wavenumber given in its simple form by equation 2.21 must be calculated. This requires estimates of k , c , \bar{u} and N . Of these, k and c are provided by the AMTM, whereas u and N require sodium lidar and possibly radar measurements (for u). The squared buoyancy frequency was calculated using equation 2.15, shown below for reference.

$$N^2 = \frac{g}{T} \left(\frac{dT}{dz} + \Gamma \right) \quad (2.15)$$

T is the average temperature obtained with the sodium lidar, dT/dz is the temperature gradient, $g=9.54\text{ms}^{-1}$ is the gravitational acceleration near 87 km, and $\Gamma= 9.5 \text{ Kkm}^{-1}$ is the appropriate adiabatic lapse rate.

The vertical wavenumber, m , allows for a distinction to be made between GWs that are freely propagating in the vertical ($m^2 > 0$), GWs that are evanescent at all observed altitudes ($m^2 < 0$), or gravity waves that are trapped or ducted in a region where $m^2 > 0$ but bounded by regions having $m^2 < 0$ [Isler *et al.*, 1997]. The vertical wavenumber squared can be estimated from the dispersion relation neglecting wind shear and curvature terms (see equation 2.21). However, in regions having variable horizontal winds, it is often important to account for these additional influences [Simkhada *et al.*, 2009]. For the purposes of this study, the more complete version of m^2 given by equation 2.22 is used and shown below for reference.

$$m^2 = \frac{N^2}{(c-u)^2} + \frac{1}{(c-u)} \frac{d^2u}{dz^2} - \frac{1}{H(c-u)} \frac{du}{dz} - \frac{1}{4H^2} - k^2 \quad (2.22)$$

As above, N and \bar{u} are measured from the lidar, and k and c are obtained from the AMTM.

Error Calculations

As both N^2 and m^2 depend on measured quantities with inherent uncertainties, we have employed an error propagation analysis to assess the expected uncertainties in the N^2 and m^2 profiles. Averaging was employed for the various fields to achieve a reasonable compromise between precision and uncertainty in estimates. The error for N^2 is given by

$$\Delta N^2 = N^2 \sqrt{\left(\frac{1}{\left(\frac{T_2 - T_1}{z_2 - z_1} + \Gamma \right)} \right)^2 \left(\frac{\sqrt{2}\Delta T}{(z_2 - z_1)} \right)^2 + \left(\frac{\Delta T}{\bar{T}} \right)^2} \quad (4.1)$$

The error calculation for m^2 is dependent on uncertainties arising from measurements of the GW horizontal phase speed and horizontal wavelength, errors in the calculated buoyancy frequency given by equation 4.1 and the wind shear and curvature terms. A general equation for the m^2 error calculation may be written as

$$\Delta m^2 = \sqrt{\left(\frac{\partial m^2}{\partial N^2} (\Delta N^2) \right)^2 + \left(\frac{\partial m^2}{\partial \hat{c}} (\Delta \hat{c}) \right)^2 + \left(\frac{\partial m^2}{\partial k^2} (\Delta k^2) \right)^2 + \left(\frac{\partial m^2}{\partial u_z} (\Delta u_z) \right)^2 + \left(\frac{\partial m^2}{\partial u_{zz}} (\Delta u_{zz}) \right)^2} \quad (4.2)$$

where \hat{c} denotes the GW intrinsic phase speed, u_z denotes wind shear, and u_{zz} denotes wind curvature. The full error calculation for m^2 as calculated from equation 4.2 is given by

$$\Delta m^2 = \sqrt{\left[\frac{1}{\hat{c}^2} (\Delta N^2) \right]^2 + \left[\left(\frac{-2N^2}{\hat{c}^3} - \frac{u_{zz}}{\hat{c}^2} - \frac{u_z}{H\hat{c}^2} \right) (\Delta \hat{c}) \right]^2 + \left[\frac{8\pi}{\lambda^3} (\Delta \lambda) \right]^2 + \left[\left(\frac{1}{H\hat{c}} \right) \left(\frac{\sqrt{2}}{dz} \Delta u \right) \right]^2 + \left[\left(\frac{1}{\hat{c}} \right) \left(\frac{2\Delta u}{(dz)^2} \right) \right]^2} \quad (4.3)$$

Sodium Density as a Tracer for Small-scale Dynamics

As a further means to describe GW responses to their propagation environments, perturbations in the sodium density are used to track vertical displacements more accurately than can be inferred from lidar and AMTM wind and temperature measurements. Sodium density perturbations due to GWs have previously been simulated [Swenson *et al.*, 1998; Shelton *et al.*, 1980] using a relation derived by Chiu and Ching [1978]. Sodium density perturbations can be derived from the sodium continuity equation [Bossert *et al.*, 2014] and are given by:

$$\rho_s' e^{-i\omega t} = \left[\left(\frac{w'}{i\hat{\omega}} \right) \left[\frac{\bar{\rho}_s}{H} + \frac{\partial \bar{\rho}_s}{\partial z} \right] + \bar{\rho}_s \frac{\rho'}{\bar{\rho}} \right] e^{-i\omega t} \quad (4.4)$$

Here ρ_s' is the sodium density perturbation, $\bar{\rho}_s$ is the mean sodium density at each altitude, $\bar{\rho}$ is the mean density at each altitude, ρ' is the atmospheric density perturbation at each altitude, $\hat{\omega} = \omega - ku$ is the intrinsic frequency, and ω is the frequency as observed by a ground-based observer.

Lidar temperature measurements do not achieve the small uncertainties required to define temperature and vertical wind perturbations associated with small-amplitude, short-period GWs with high confidence. However, the AMTM provides high-precision temperatures averaged over the OH layer near 87 km at high horizontal and temporal resolution. These temperatures provide

accurate estimates of the temperature perturbations for GWs having sufficiently large vertical wavelengths, e.g. significantly greater than the FWHM of the OH layer, to avoid large phase cancellation across the OH airglow layer depth. [Snively *et al.*, 2009].

Equation 4.4 can be re-written in terms of the temperature perturbations measured with AMTM by using the Boussinesq polarization relations to relate wind, temperature, and density perturbations. This form is given below:

$$\rho_s' e^{-i\omega t} = \left[\left(\frac{g}{N^2} \frac{T'}{T} \right) \left[\frac{\bar{\rho}_s}{H} + \frac{\partial \bar{\rho}_s}{\partial z} \right] - \bar{\rho}_s \frac{T'}{T} \right] e^{-i\omega t} \quad (4.5)$$

The complete derivation of equation 4.5 is given in Appendix C.

The AMTM only provides temperature measurements at the OH layer. However, an observed GW in the AMTM can be assumed to be propagating with similar character at all altitudes, and a prediction of the sodium density perturbations if that observed GW in the OH layer were to be propagating at all altitudes in the sodium layer can be obtained. Additionally, GW momentum flux must be constant with altitude for a steady, monochromatic, non-dissipating, vertically-propagating GW, which gives the following relation:

$$\rho(z)u'(z)w'(z) = \rho(z_o)u'(z_o)w'(z_o) \quad (4.6)$$

The background density in equation 4.6 varies with altitude as

$$\rho(z) = \rho_o e^{-z/H} \quad (4.7)$$

Using equations 4.6 and 4.7 and assuming a propagating GW and stable environment (e.g. $N^2 > 0$ and $\hat{\omega} < N$), a relation between the temperature perturbation measured by the AMTM and temperature perturbations at other altitudes can be obtained. This relation is given by:

$$\frac{T'(z)}{\bar{T}(z)} = e^{(z-z_0)/(2H)} \sqrt{\frac{N^3(z)}{N_o^3(z)} \frac{T'(z_0)}{\bar{T}(z_0)}} \quad (4.8)$$

Equation 4.8 yields a vertical profile of T' , or ρ_s' from equation 4.5 for GWs satisfying the above assumptions. Altitudes at which a GW has a vertically-propagating character should yield close agreement with the predicted altitude variations in T' and ρ_s' . However, altitudes at which the predicted sodium density perturbations do not closely resemble the measured sodium density perturbations imply a region where the GW structure in the vertical *does not* conform to the above assumptions. In this way, the measured sodium density profiles can allow us to distinguish between GWs that are vertically propagating and those that may be evanescent or ducted at specific altitudes.

4.2 Influences of Propagation Environments

The following studies investigate the GW background environments that lead to various propagation conditions within the MLT.

4.2.1 Gravity Wave Ducting

On January 22-23, 2012, a long-lived (> 9.5 hrs) short-period ($T < 15$ minutes) GW event was observed throughout the night using our collocated instruments at ALOMAR. The GW was apparent during several time intervals in the AMTM from around 19:00 UT on January 22 to 5:30 UT on January 23. Figure 4.1 shows several AMTM images of the GW structure throughout the night. The GW appeared to be propagating almost entirely from the east to the west. For a short period during the night, a second GW was also observed (an example of this is shown in

the figure at 22:38 UT). However, these results will focus on the primary GW that was observed for the majority of the night moving from east to west.

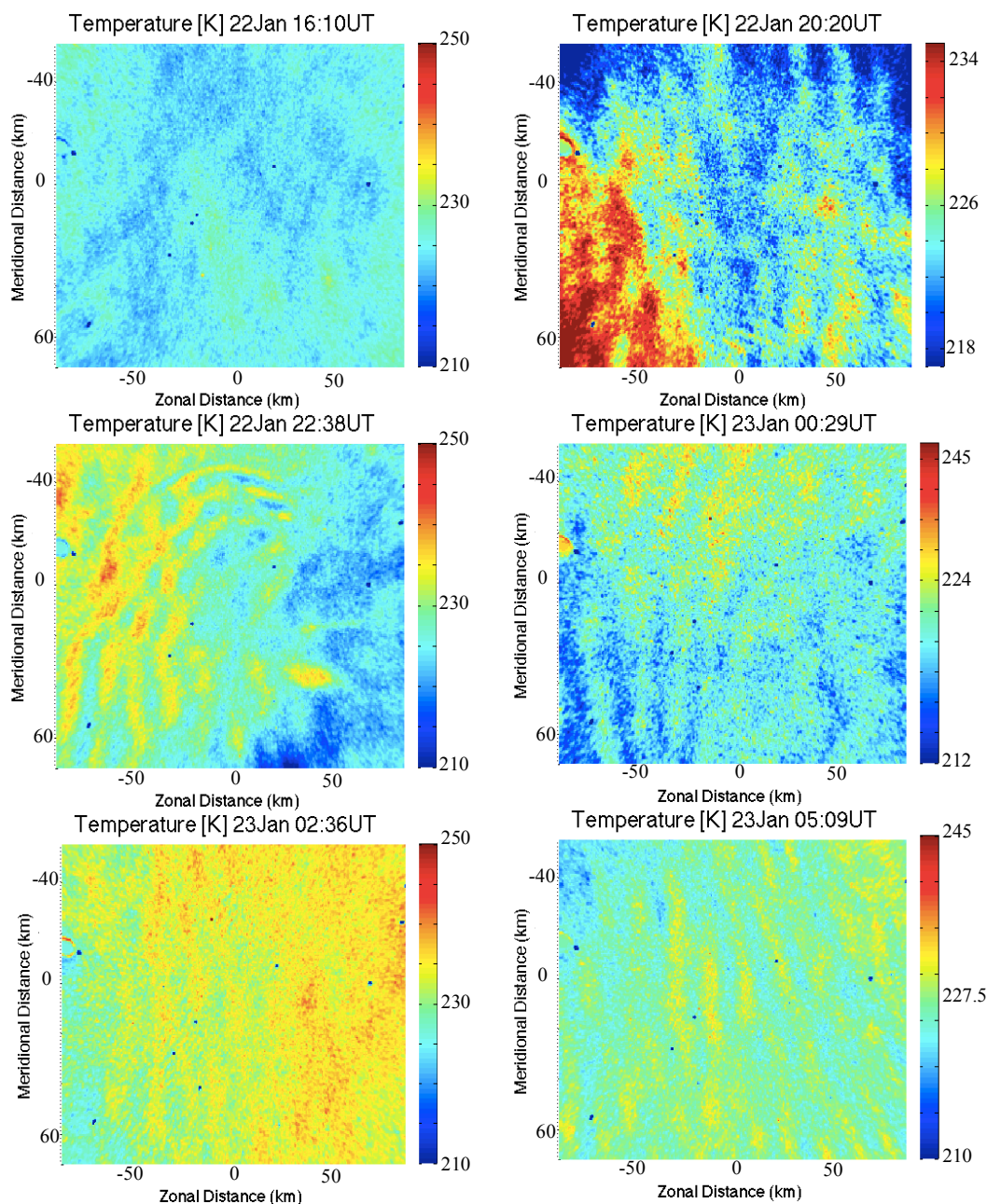


Figure 4.1: AMTM spatial temperature maps show observed waves throughout the night of January 22-23, 2012 starting shortly after 20UT. Times are shown at the top of each panel. North and East are up and to the right. Note the differing temperature scales in each panel.

Using successive AMTM images, the average horizontal phase speed of the GW was measured at several times throughout the observation interval and was determined to be $\sim 34.5 \text{ ms}^{-1} \pm 3.4 \text{ ms}^{-1}$ to the west. The mean wavelength of the GW was $18.9 \text{ km} \pm 1.5 \text{ km}$. These estimates result in observed GW periods of $T_{\text{obs}} = \lambda/c = 9.1 \pm 1.5 \text{ min}$. The temperature perturbation for this GW was estimated from multiple AMTM images throughout the night by evaluating the temperature amplitude of the GW using cross sections from the AMTM images. For this night, the average temperature perturbation was found to be $2.5 \text{ K} \pm 0.6 \text{ K}$.

Sodium densities were calculated using an integration time of 1 min and are shown throughout the night in Figure 4.2. The calculated error for the 1 min sodium densities between 79 km and 96 km is $\sim 10^8 \text{ m}^{-3}$. Measured sodium density perturbations were observed with amplitudes on the order of $\sim 1 \times 10^9 \text{ m}^{-3}$, which is several times the calculated error for this integration. Winds and temperatures were calculated averaging two lidar beams using 1-hr averaging with a 10-min sliding window and vertical averaging of 1.128 km with a 0.141 km sliding windows. The resulting average errors for the 1.128km and 1hr averaged temperature and wind based on photon noise between 79 km and 96 km are 0.19 K and 0.32 ms^{-1} . These errors calculated from photon noise are used in the error calculations for N^2 and m^2 . Estimated temperatures and horizontal winds in the westward direction of observed GW propagation for the night are shown in Figures 4.3 and 4.4.

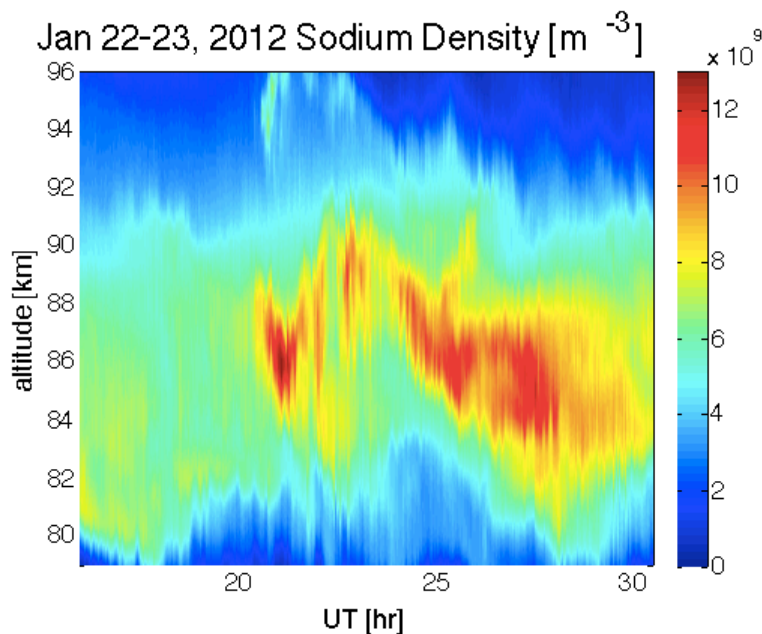


Figure 4.2: Sodium densities measured with the sodium resonance lidar at ALOMAR using a 1-min integration and 150-m range resolution on 22-23 January 2012.

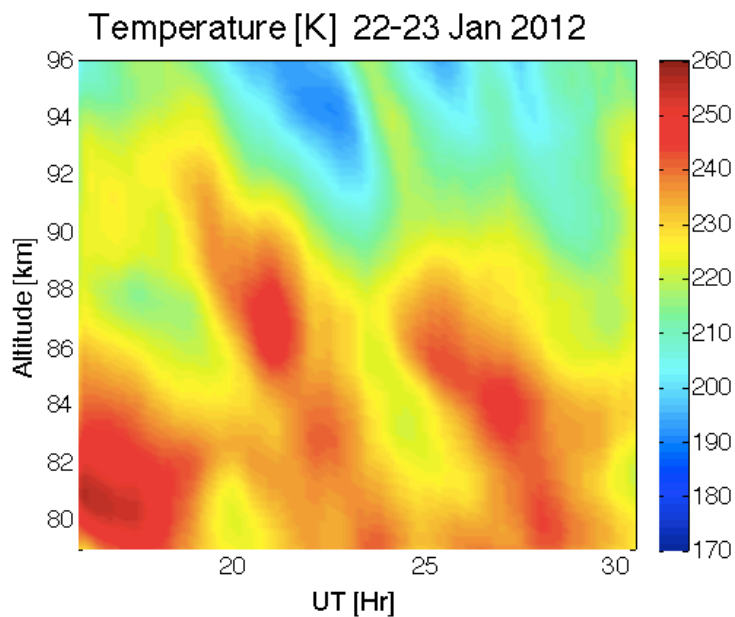


Figure 4.3: Temperature profiles measured with the sodium lidar using 1.128 km and 1-hr averaging on 22-23 January 2012.

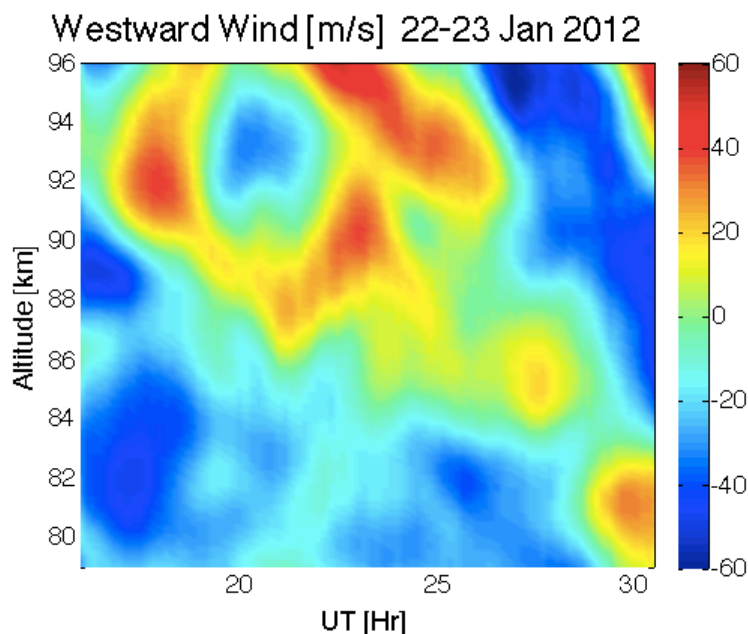


Figure 4.4: As in Figure 3 but for winds in the direction of GW propagation from east to west. Radial winds were converted to horizontal winds assuming vertical winds are zero for a 1-hr average.

Temporal and vertical estimates of N^2 are shown in Figure 4.5. A value of $N^2 < 0$ implies a statically unstable atmosphere. On this night, the atmosphere was found to be relatively stable. However, there are several regions of small N^2 that can possibly lead to an unfavorable propagation environment for the GW when the buoyancy period is larger than the intrinsic GW period. The median percentage error for N^2 between 79 km and 96 km was found to be 2.9% using the 1-hr and 1.128 km averaging from both lidar beams. A plot of the errors associated with the N^2 calculation is shown in Figure 4.6. Using these N^2 values, calculations for m^2 were made.

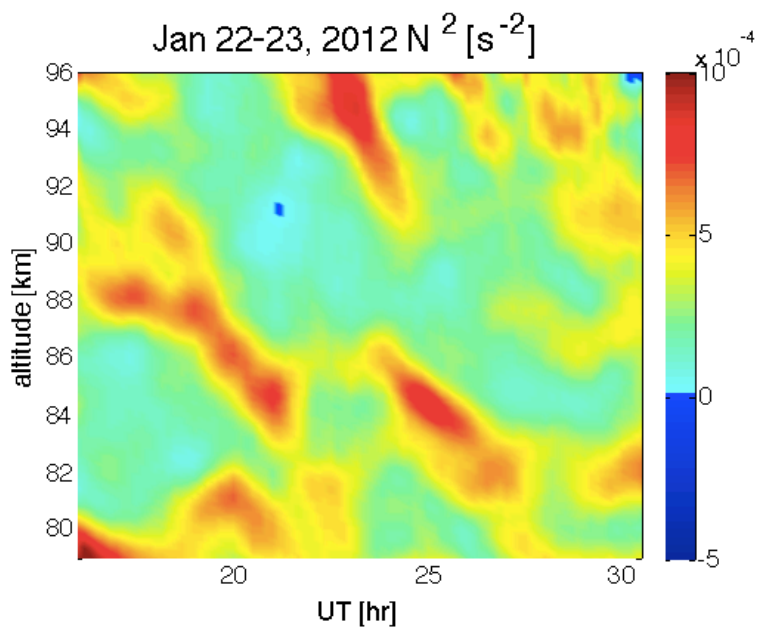


Figure 4.5: N^2 calculated using the temperatures shown in Figure 3

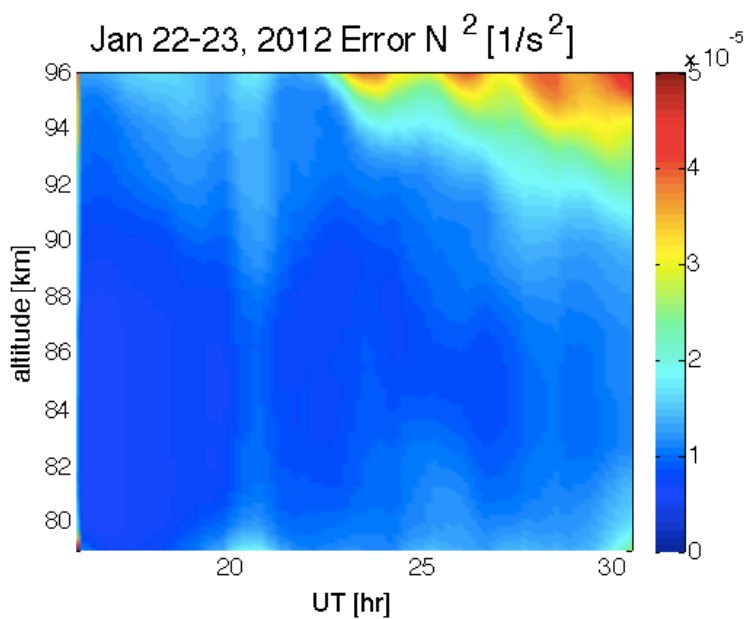


Figure 4.6: Errors calculations from equation 4.3 associated with N^2 calculated from equation 4.1

The m^2 values were calculated to correspond to a GW with a horizontal wavelength $\lambda=18.9$ km and a phase speed $c = 34.5$ ms^{-1} towards the west, so that an average of the observed parameters could be provided. These m^2 values were calculated using Equation 4.2. The resulting m^2 values are given in Figure 4.7. The errors for these m^2 values were calculated using Equation 10 and a plot of these errors is given in Figure 4.8. The median percent error associated with m^2 between 79 km and 96 km is 47.3%.

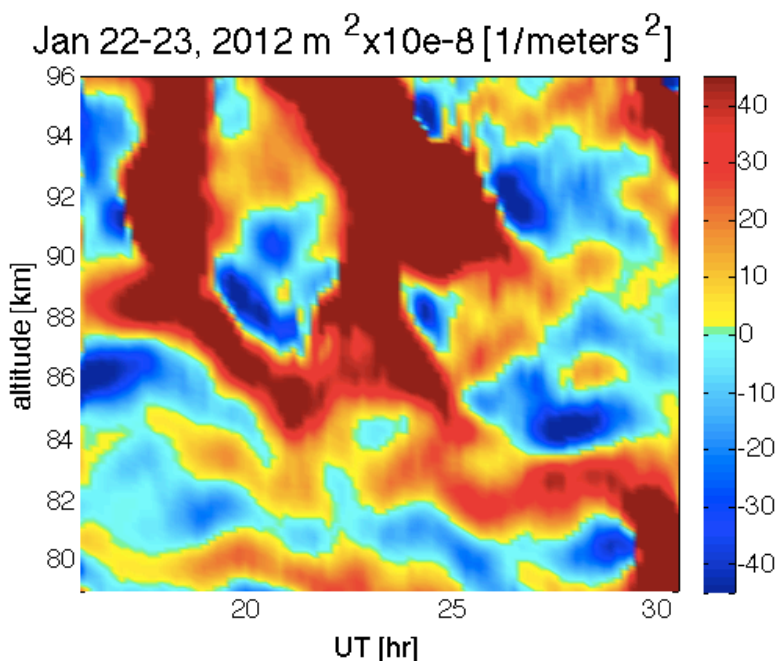


Figure 4.7: m^2 values calculated including the wind shear and curvature terms.

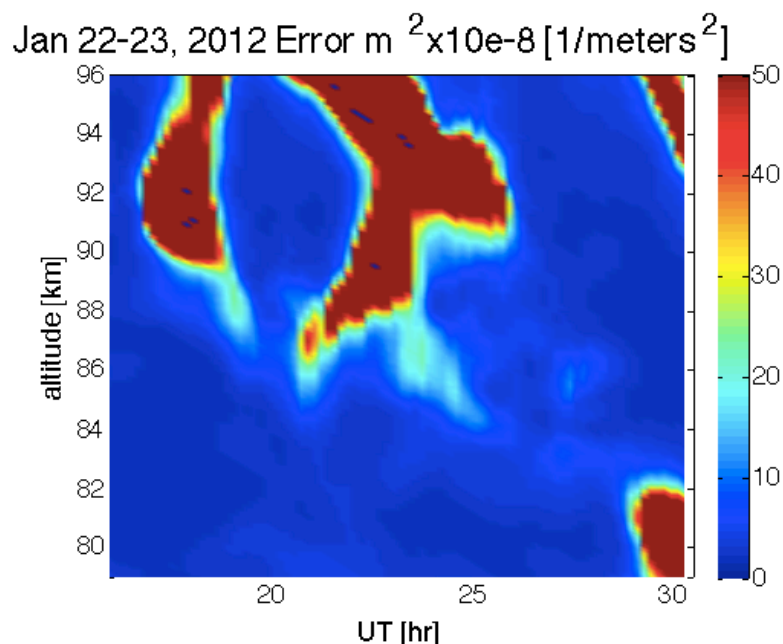


Figure 4.8: Error calculated from equation 4.5 associated with m^2 calculation using equation 4.2

ρ_s' estimates were obtained using calculated values for N^2 , the GW temperature perturbation estimates from the AMTM, and the vertical sodium density gradient obtained from a 20-min smoothed sodium density profile. The OH layer peak was found to be at 86 km with a FWHM of 8 km, so measured temperature perturbations from the AMTM are assumed to correspond to this center altitude. Predicted ρ_s' were calculated by conforming to the relation given by equation 4.5, and assuming that the GW was propagating in a stable environment at all altitudes and times. Additionally, phases imposed on the predicted density perturbations are relative and assumed to have no variations in altitude over a range of a few km (as if the vertical wavelength is very large, for convenience). Assuming a specific smaller vertical wavelength and corresponding phase variation with altitude would also be possible, but it would not alter the pattern of time-height variations of ρ_s' we intend to compare with observations. The period for the density perturbation is calculated using observed phase speeds from the AMTM.

It is expected that there will be phase changes in ρ_s' in altitude that vary depending on m^2 where a GW is propagating [Vadas and Nicolls, 2009]. However, these are necessarily small for vertical wavelengths larger than the vertical extent of reliable lidar ρ_s' measurements, typically spanning <20 km. As noted, though, this analysis emphasizes comparisons of the amplitudes of predicted versus measured ρ_s' to interpret where GWs have propagating versus evanescent behavior.

Plots for the predicted and measured ρ_s' for three different periods during the GW event throughout this night are shown in Figure 4.9 together with the corresponding calculated m^2 values. The left plots in Figure 4.9 show the predicted ρ_s' calculated from equation 4.7 using the smoothed background density, N^2 values, and GW parameters measured by the AMTM. The predicted ρ_s' was calculated using the average measured GW parameters and temperature perturbations for the entire the night. The center plots show the measured ρ_s' . These are obtained by subtracting the smoothed sodium density profile from the raw density profile. The right plots show the zoomed views of the corresponding m^2 values calculated from lidar winds and temperatures and AMTM GW parameters that were previously shown for the entire night in Figure 4.7. In these three cases, regions of good agreement between the amplitude of the predicted and measured ρ_s' indicate the GW is either propagating with similar characteristics to the GW observed from the AMTM or distributed across ducting regions. Regions where there is poor matching between the amplitudes of predicted and measured ρ_s' indicate that the GW is likely not propagating in that region. For example, if the perturbation amplitudes are smaller at an altitude above the OH layer, it could indicate that the wave has decayed, or is evanescent in that region. These areas of similar or differing predicted versus measured ρ_s' amplitudes can be

compared to calculated m^2 values which show regions of $m^2 > 0$ or $m^2 < 0$ indicating more likely altitudes for propagating or evanescent responses. In this way, assessments of locations of GW propagation in time and altitude can be made.

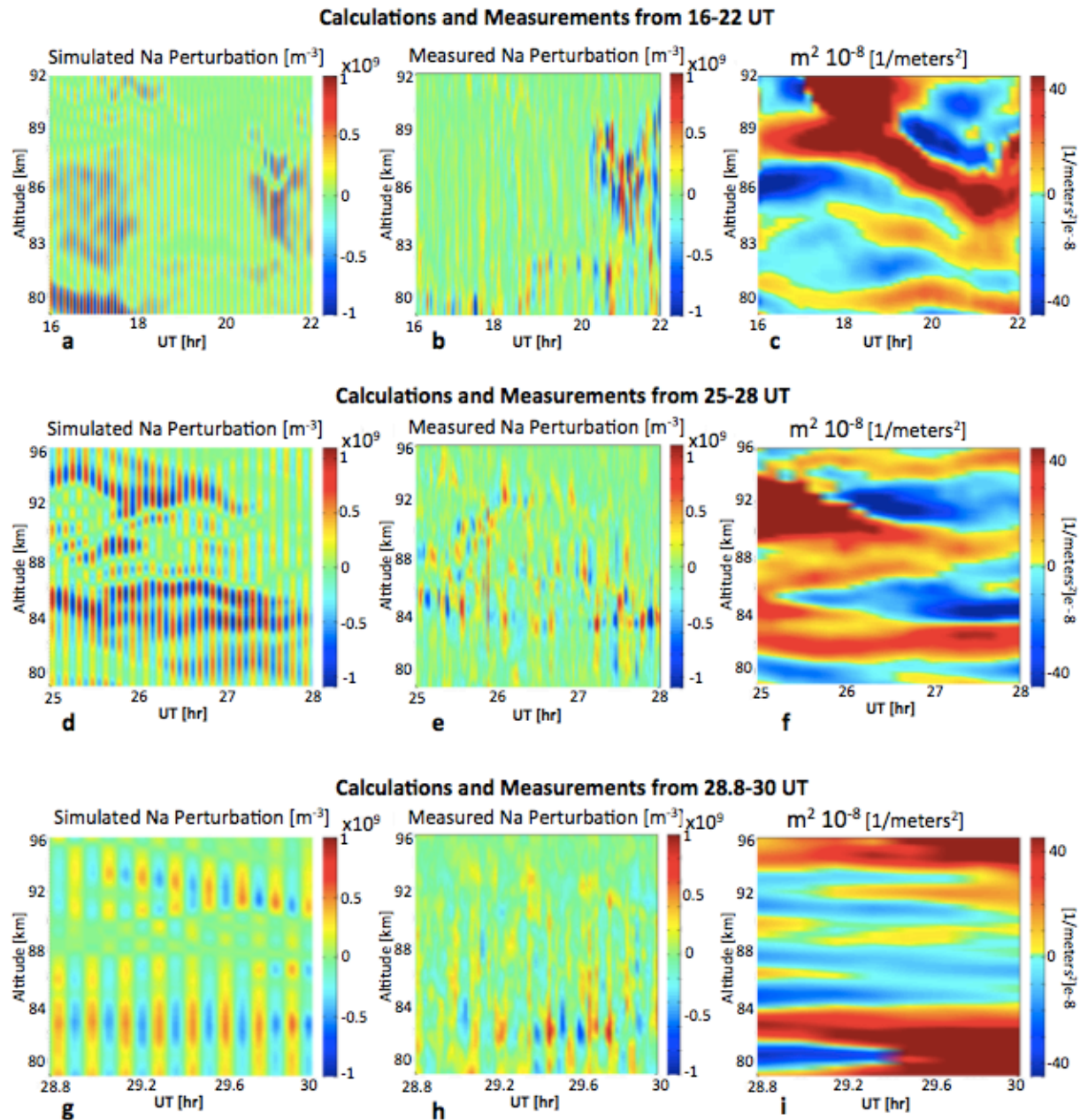


Figure 4.9: (Left panels) Predicted density perturbations using a constant temperature perturbation in altitude and time, the smoothed background sodium density, and average GW parameters measured over the night. (Middle panels) Measured sodium density perturbations. (Right panels) m^2 values for the corresponding time and altitude intervals. (left to right) Time intervals from 16 to 22 UT, 25 to 28 UT, and 28.8 to 30 UT. Calculations were made using an average of GW parameters observed throughout the night.

Figures 4.9a-c show predicted and measured ρ_s' and m^2 from 16UT-22UT. Figure 4.9a shows the predicted ρ_s' for an assumed propagating GW with a temperature perturbation of 2.5 K at 86 km. It should be noted that temperature perturbations were first observed in the AMTM just before 19 UT. However, a GW with a temperature perturbation of 2.5 K was imposed on the background sodium density field for the entire interval. In the simulated ρ_s' shown in Figure 9a, if a GW were to be propagating between 16 and 18 UT with a T' amplitude of 2.5K at 86 km, ρ_s' would be easily observable near 80 km, and still moderately observable from 82 km-88 km. Conversely, the measured ρ_s' in Figure 9b shows measured ρ_s' that are smaller in amplitude at 80 km than the predicted, and measured ρ_s' that are largely unobservable above this point. This implies that a GW may have been present at lower altitudes but did not yield significant displacements extending to higher altitudes. During this period, the AMTM did not observe any GWs, which also suggests that the GW observed in the sodium layer near 80 km did not extend to altitudes near the OH layer peak. The m^2 fields displayed in Figure 9c show that the atmospheric conditions lead to a largely evanescent region between 81-87 km for this particular GW, including a very strongly evanescent region near 86 km. Given that this evanescent region is large in vertical extent, and the ρ_s' observed at 80 km are much smaller than those predicted for a T' of 2.5K, it seems likely that the GW observed in the measured ρ_s' was ducted at a lower altitude and had decayed in amplitude to the point where it could no longer be observed in the AMTM at 86 km due to evanescence.

Continuing with this interval, measured ρ_s' were observable near 82 km from 19 UT to later times. However, the background sodium density had a nearly constant mixing ratio at somewhat higher altitudes, so that if a GW were to be propagating, it would not be observable in the sodium density layer above 82 km at 19UT. The AMTM observed a GW starting slightly

before 19 UT, which indicates that the GW associated with the ρ_s' at 82 km and 19 UT may also be present with measurable amplitudes at higher altitudes. One reason this GW began to be observable in the AMTM around 19 UT is that a region having $m^2 > 0$ appeared after this time from 82-84 km where the environment had been largely evanescent before. This region appears to have allowed the GW to reach higher altitudes than before by tunneling between regions having $m^2 > 0$. Somewhat after 20UT, the characteristics of the background sodium density layer allowed for observable GW ρ_s' , and these perturbations clearly revealed the GW to extend to 86 km near the peak of the OH layer, which is also a region of $m^2 > 0$ according to Figure 4.9c. The analysis of this interval provides evidence that while large regions of evanescence in altitude can prevent a GW from reaching higher altitudes, alternating regions of evanescence and vertical propagation over a few kilometers in altitude can allow a ducted GW to achieve a much larger vertical extent.

Figures 4.9d-f show times from 25-28 hours (1-4 UT on January 23, 2012). During this time it appears that the predicted ρ_s' in Figure 4.9d overestimates the measured ρ_s' near 86 km. Additionally, the measured ρ_s' shown in Figure 4.9e decrease as altitude increases. This is especially apparent near 94 km where the predicted ρ_s' are strong, but the measured ρ_s' are very weak. Figure 4.9f exhibits a strong evanescent region starting near 25 hours and 90 km. It is possible at this time that a GW was propagating at a lower altitude but failed to penetrate multiple evanescent regions at higher altitudes, which would cause a much lower measured ρ_s' above 94 km. The comparison between the measured and predicted ρ_s' suggests that the GW observed in the AMTM may have been intermittently propagating and evanescent at the OH layer at these times due to multiple evanescent regions below 87 km.

Figures 4.9g-i show data from the end of the night when the GW was still visible in the AMTM data. ρ_s' predictions in Figure 4.9g show small-amplitude perturbations throughout the layer that can be seen clearly at 94 km. However, the measured ρ_s' in Figure 4.9h are only easily apparent near 82 km and quite faint above this region. Investigation of the m^2 values in Figure 4.9i show a mostly evanescent region from 84-94 km. Additionally, a region of large $m^2 > 0$ is seen below 84 km. Given the altitude of the most easily observed ρ_s' , it seems likely that the GW is ducted below 84 km and evanescent above this region. The GW T' measurements from the AMTM are averaged over regions having larger and smaller dT'/dz , which results in an underestimate of T' when significant variations in dT'/dz are within the airglow layer. This accounts for the stronger than predicted measured ρ_s' at 82 km and weaker than predicted measured ρ_s' at higher altitudes where the wave may be evanescent for the assumed GW T' based on the AMTM estimate.

Each of the three cases described above shows evidence of a GW that may have been propagating at lower altitudes, or in the lower altitude range of the sodium density profile, and was likely evanescent at several altitudes throughout the sodium density layer from 79 km to 96 km. The conditions varied throughout the night in the three cases, and at various times the evanescent regions extended over a large depth, preventing the GW from reaching higher altitudes. All three cases showed evidence of a GW that was ducted or confined at some altitude given the evanescent regions in the m^2 profile.

These measurements utilizing the sodium lidar are only available over a range of ~20 km, so it is difficult to predict the origin of the observed waves. The observed GW or GWs could be propagating from a nearby region, or these GWs could have been ducting over a significant horizontal range. Given the complexity of the region observed from 79 km to 96 km, it is

possible that the GW could be propagating through multiple ducting regions. It is interesting that this GW, or multiple similar characteristic GWs persisted throughout most of the night despite the changing atmospheric conditions. During all times of the night, there were observable evanescent regions in addition to regions of $m^2 > 0$ (ducts), which gives evidence that ducting regions may provide stable enough environments for GWs to propagate for extended periods of time.

The results discussed above suggest that this measurement and analysis technique employing measured and computed ρ_s' enables more quantitative characterization of GW propagation environments than without such a comparison. In particular, it provides a method for distinguishing evanescent GWs from propagating GWs in complex and temporally-evolving environments. Specifically, comparisons of m^2 values and sodium density perturbations permit assessments of the altitudes at which observed GWs exhibit evanescent or ducted behaviors as opposed to propagating vertically.

Calculated and measured ρ_s' suggest that calculated values of N^2 , m^2 , and AMTM temperatures provide valuable insights into GW propagation behavior. Utilization of the Na density measurements thus provides another layer of validation to these measurements for studies of small-scale GW structure and behavior.

This study has also revealed that the ducting environment can vary significantly in time, while continuing to support GWs having similar character as the ducting environment evolves. Dual lidar and AMTM measurements also allow more spatially precise predictions of ducting given their combined sensitivity to both horizontal and vertical variations of the GW and mean fields. We expect that applications of these methods will also be of value at other sites benefiting from correlative lidar and MTM measurements.

4.2.2 Small-scale Gravity Wave Propagation

The background environment can have very strong effects on the propagation of small-scale GWs. The following study focuses on an event from ALOMAR in which multiple scales of GWs were observed, including a large *MF*, small-scale GW. This section focuses on the propagation environment for the smallest-scale GW observed. Figure 4.10 shows a keogram from 27-28 January 2014. On this night, multiple different period waves were observed [Fritts *et al.*, 2014] including ~12-hr, 4-hr, 1-hr, and 10-minutes, the later of which is described in more detail here. Figure 4.10 shows the keogram for the night during which these GW events were observed. The 10-minute GW appears to be strongly modulated by some of the larger-scale GWs, especially the 1-hr period GW. A spatial view of the 10-minute period GW is given in Figure 4.11.

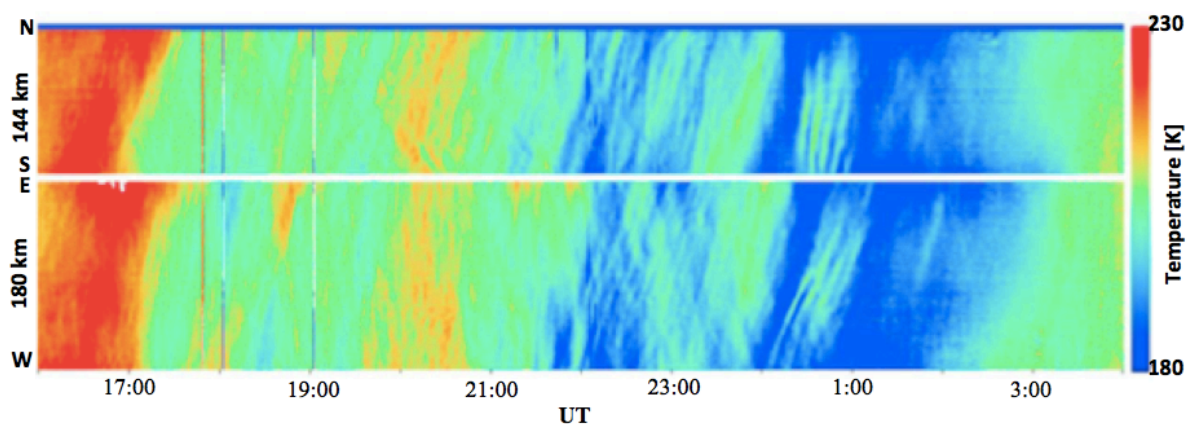


Figure 4.10: Keogram from 27-28 January 2014 showing multiple scales of GW throughout

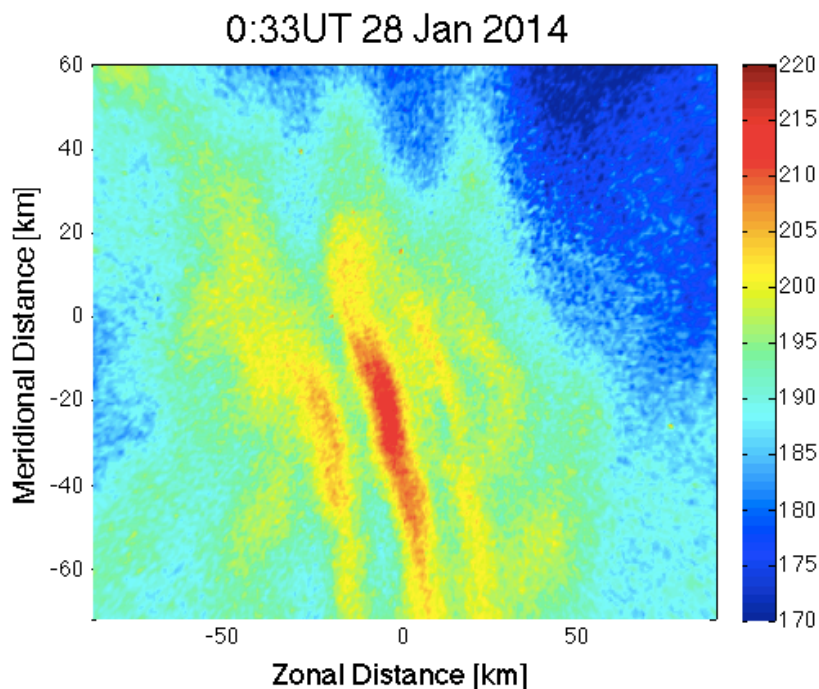


Figure 4.11: Spatial temperature map showing the 10-minute period GW

As shown by Figure 4.11, the 10-minute period GW has a horizontal wavelength of $\lambda_h \sim 24$ km. The ground relative phase speed was calculated to be ~ 45 ms^{-1} with a propagation direction $\sim 70^\circ$ ENE. The background conditions for this GW can be assessed using available sodium lidar winds and temperatures as well as SAURA radar winds. On this particular evening, the lidar was shut off slightly before 11 UT. The SAURA radar was operated for the entire duration of these observations. The lidar temperatures are shown in Figure 4.12, and the SAURA radar zonal and meridional winds are shown in Figures 4.13 and 4.14 respectively.

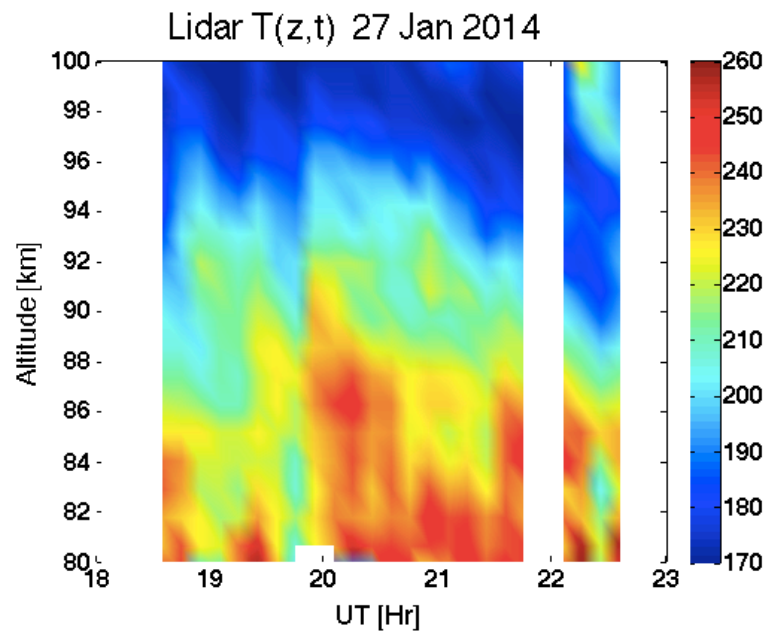


Figure 4.12: Lidar temperatures with 10 minute resolution for 27 January 2014

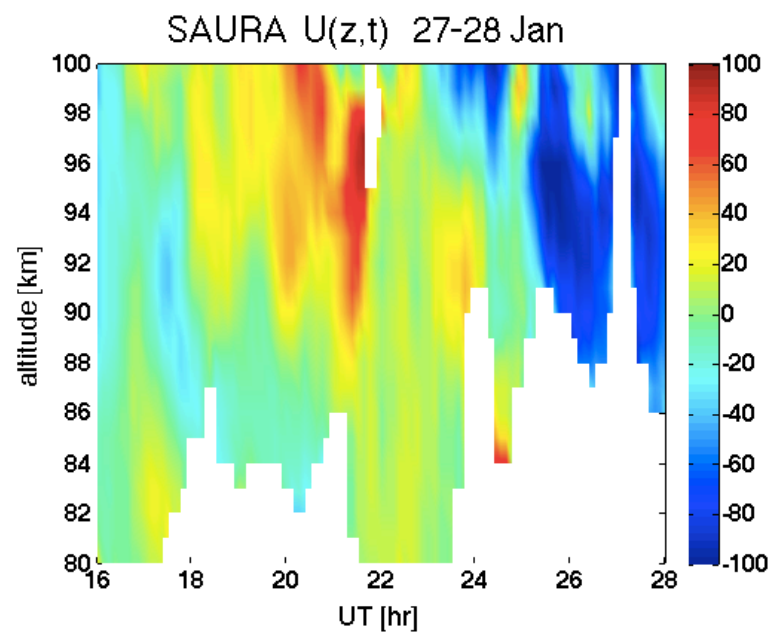


Figure 4.13: SAURA radar zonal winds with 7.5 minute resolution

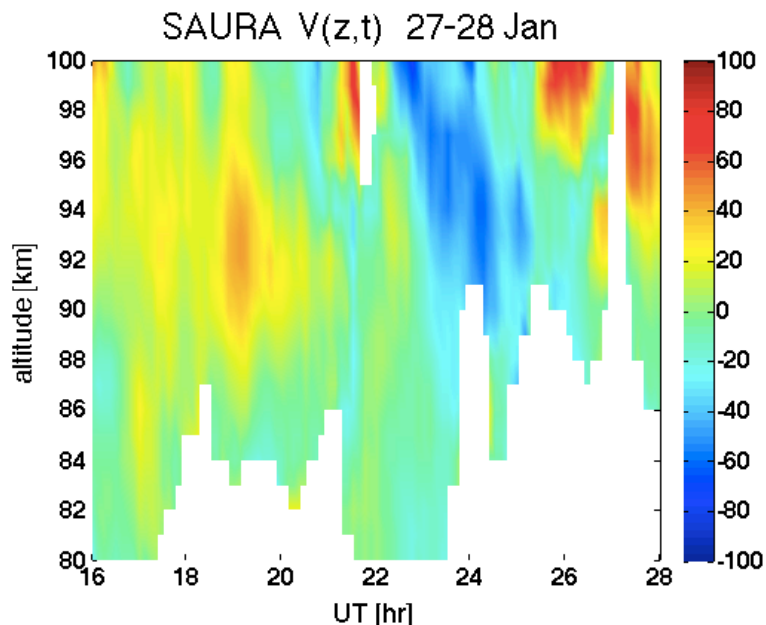


Figure 4.14: SAURA radar meridional winds with 7.5 minute resolution

Although the temperatures from the lidar are unavailable for the time period of the observed 10-minute period GW, the lidar temperatures can still be used to estimate the stability of the background atmosphere during the first portion of the evening using equation 4.1. A calculation of N^2 throughout the duration of the lidar run is given in Figure 4.15, and a nightly average of N is given in Figure 4.16. The average value of N fluctuates between 0.0145 and 0.02 s^{-1} in altitude, and for the duration of the lidar measurements, the atmosphere appears relatively stable. It should be noted that these conditions may change slightly as the evening progresses to the time when the 10-minute period GW is observed. N was estimated to be $\sim 0.0146 s^{-1}$ [Fritts *et al.*, 2014] based on lidar temperature observations and the evolutions of the larger-scale motions. This value is used for further analysis.

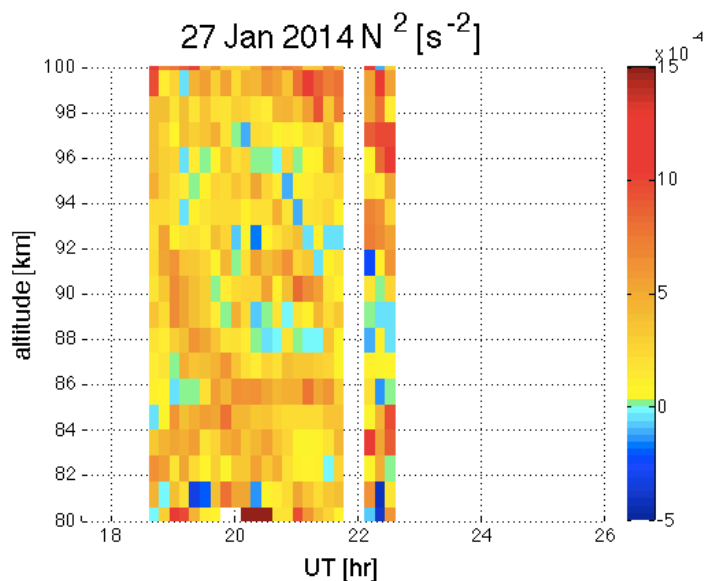


Figure 4.15: Calculation of N^2 using equation 4.1

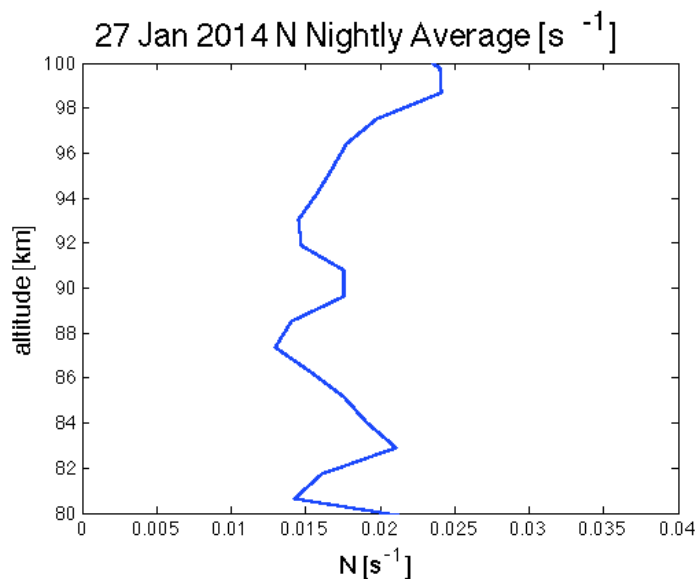


Figure 4.16: Nightly average of N calculated using the data from Figure 4.15

In order to assess the propagation environment for the 10-minute period GW, m^2 , the vertical wavelength can be calculated as was done in the previous section using equation 4.2. In this case, the average N value of 0.0146 s^{-1} is used, and the radar winds are used to calculate the background wind in the direction of GW propagation, and these have a 1 km resolution. Given

the large errors associated with the curvature and wind shear terms in equation 4.2, these terms are neglected for this calculation. The resulting estimate of m^2 for the evening that would exist for the 10-minute period GW observed between 0 and 1 UT is shown in Figure 4.17.

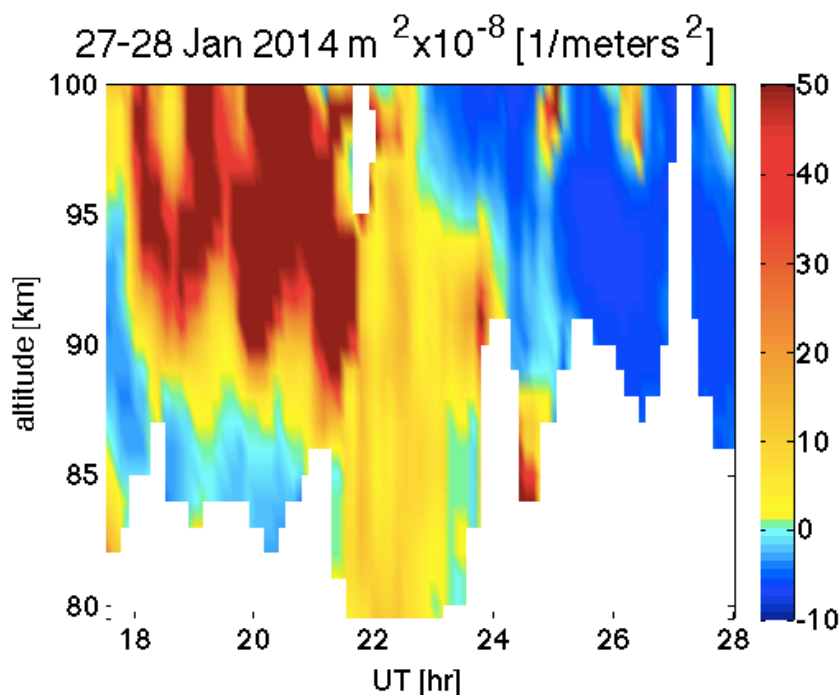


Figure 4.17: Calculated m^2 for the 10-minute period GW

From Figure 4.17 the 1-hr period GWs can clearly be seen to influence the propagation environment of the 10-minute period GWs. The phase influence of the 12-hour period wave also has visible effects. The 10-minute period GW was observed shortly after 24UT. While the radar coverage does not have extensive low altitude coverage during this time period, we see from the trends over the course of the night that the larger-scale dynamics are likely creating an environment during this time that is more conducive to small-scale GW propagation. Between 18-21 UT it appears that there is a region of unfavorable region of propagation below the

favorable region above 90 km produced both by the 12-hr and 1-hr period GWs. After 22UT, the conditions change at lower altitudes and would allow for the shorter 10-minute period GW to propagate. It appears near 24 UT the 1-hr period GW again plays a role in creating an environment conducive to propagation for the 10-minute period GW. It is just after this time that the GW was observed. Its coincidence with the 1-hr period GW is also observed in the keogram in Figure 4.10. This study shows the strong influences that larger-scale dynamics, including large-scale GWs, can have on smaller-scale GW propagation.

4.2.3 Gravity Wave Critical Levels

Critical levels formed by the background wind speed create boundaries to GW propagation that often lead to breaking and dissipation. Observations of such occurrences during the DEEPWAVE campaign are discussed here in more depth. Specifically, observations over the mountains of New Zealand are discussed, and mountain waves (MWs) are a key part of this analysis.

DEEPWAVE Cross Mountain Flights

The DEEPWAVE campaign had multiple flight paths ranging from flights west of New Zealand over Tasmania, predictability flights, Southern Ocean flights, and mountain wave flights. The mountain wave flights in particular focused on MWs generated over the South Island of New Zealand with flight tracks over Mt. Aspiring (3,033 m) and Mt. Cook (3,724 m). An example flight track and corresponding rough terrain map are given in Figures 4.18 and 4.19 respectively. The critical level wave breaking events discussed in the following sections were observed on similar flight paths.

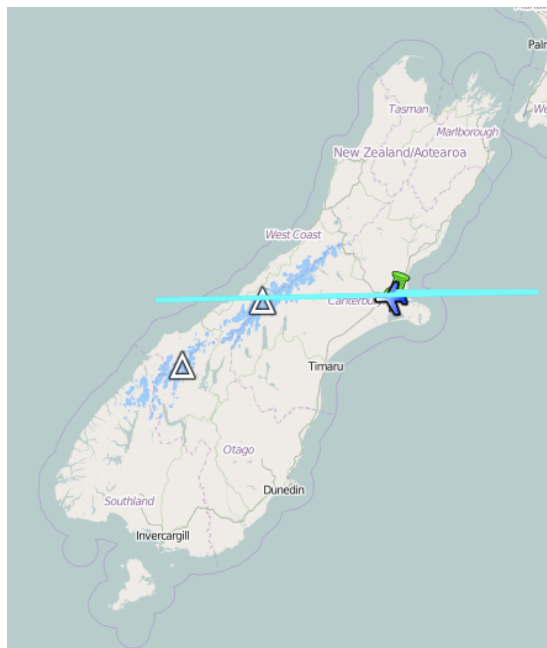


Figure 4.18: Example flight track over Mt. Cook

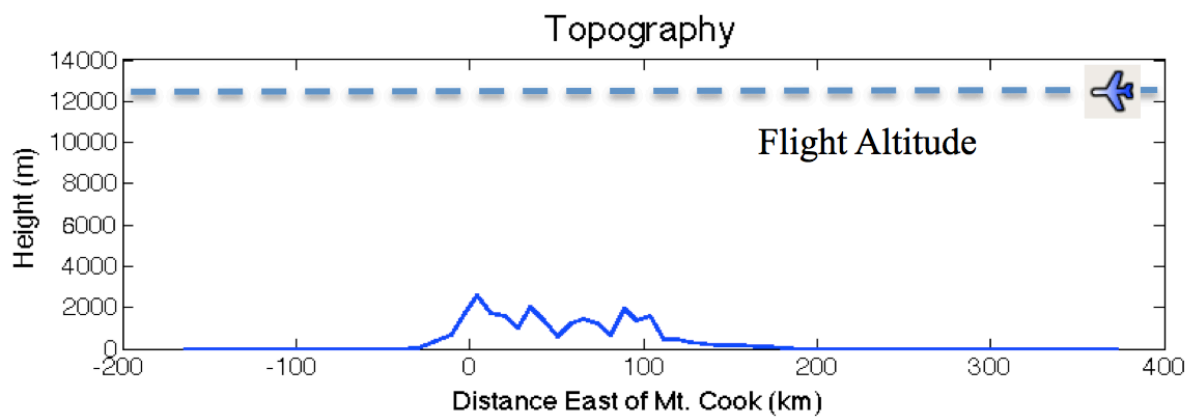


Figure 4.19: Flight diagram and approximate ground topography

An Overview of Observed MW overturning and breaking

Several apparent events of MW breaking were observed during the DEEPWAVE campaign. Some examples of these events are shown in Figure 4.20. These events are often times very clearly observed in the lower side of the sodium density layer. However, the MWs are not observed to propagate through the entire sodium layer, implying a critical level or boundary preventing these MWs from propagating to higher altitudes. The sodium density provides a tracer for the dynamics accompanying these events, and the sodium mixing ratios provide this tracer relative to the background atmosphere. Some of the sodium mixing ratios associated with these events show clear GW overturning on the bottom side of the layer, which is also an indicator of GW breaking. A region of a smaller sodium mixing ratio over a larger sodium mixing ratio indicates overturning. Figure 4.20 shows several examples of observed GW overturning during three different cross-mountain flights. Both the sodium densities and mixing ratios are shown for reference.

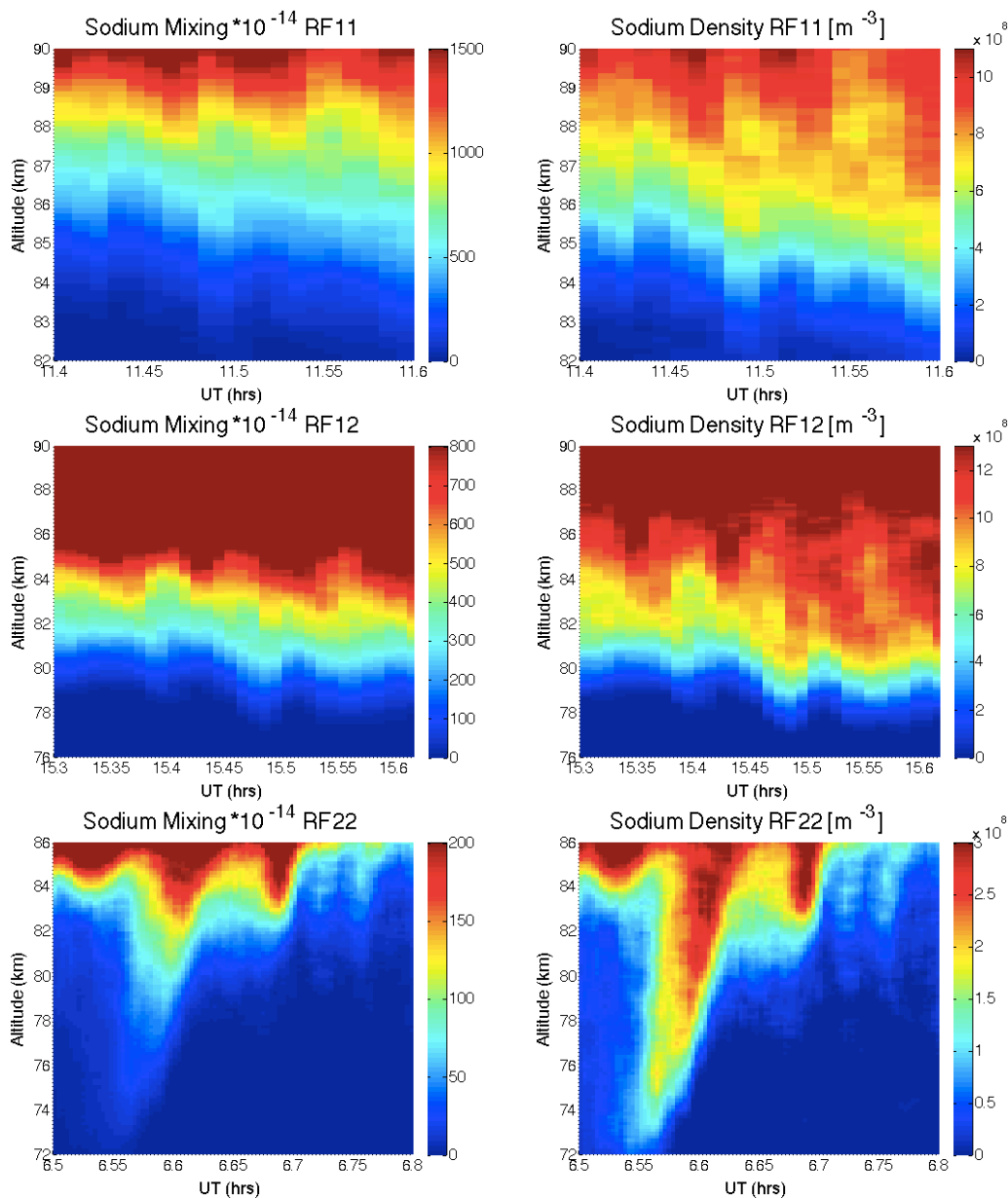


Figure 4.20: GW overturning observed in the sodium mixing ratios on three different flights during the DEEPWAVE campaign.

The overturning events shown in Figure 4.20 are associated with GW breaking. For the specific causes of this, RF 22 on 13 July 2014 is discussed in more detail in the following section.

13 July 2014 Critical Level and Large-Scale Breaking

The DEEPWAVE data set collected during research flight 22 (RF22) on 13 July 2014 (described in [Bossert *et al.*, 2015]) consisted of a Rayleigh lidar, sodium lidar, AMTM, and two side-viewing OH airglow cameras onboard the GV aircraft. Additionally, radar data was available from the meteor radar on Tasmania, and ground-based Rayleigh lidar measurements were available only on the preceding and following days of the campaign because weather prevented ground-based measurements during the flight time. The DEEPWAVE campaign also utilized forecasts for flight planning from the European Center for Medium-range Weather Forecasting (ECMWF) and various other forecast models. This particular flight day was predicted to be a low forcing event with weak MW activity in the lower atmosphere.

The flight track consisted of four passes over Mt. Cook as shown in Figure 4.18. The four cross-island GV flight segments on RF22 occurred between 6:15 and 9:10 UT (18:15-21:10 local time), and were each ~530 km in length. Each flight segment was sufficiently long to identify approximately two wavelengths of a stationary, large-scale MW seen in both the Rayleigh lidar temperatures from 20-60 km in altitude and in the AMTM and IR camera OH brightness at the OH layer altitude (~87 km). The side viewing OH brightness images confirm that the phase fronts of the large-scale MW were indeed stationary along each pass. The slightly extended (east-west) imaging data suggest a MW λ_h varying from ~200 km at the eastern side of each flight segment to ~300 km at the western side, with a mean of λ_h ~240 km.

The 240-km MW observed by the Rayleigh lidar is shown as a $T'(x,z)$ zonal-vertical cross section for flight segment 4 in Figure 4.21. $T'(x,z)$ was obtained by subtracting an averaged background temperature for the segment. This MW exhibits a pronounced increase in both its amplitude and its vertical wavelength with increasing altitude. T' varies from a few K at the

lower altitudes to ~ 15 K or larger at ~ 52 km and above. We expect amplitude growth with altitude for conservative GW propagation. At lower altitudes between ~ 20 - 55 km, the growth with altitude is a factor of ~ 8 - 10 , which is expected for a GW with a mean scale height of $H \sim 6$ - 7 km that is growing in amplitude without significant dissipation. λ_z likewise increases with altitude from ~ 10 km or less below ~ 30 km in altitude to ~ 20 - 30 km at the higher altitudes. The changing vertical wavelength of the $\lambda_y \sim 240$ km MW is consistent with the increase in zonal wind predicted by the ECMWF model (see equation 2.21 for relation of horizontal winds to vertical wavelength). For reference, Figure 4.22 shows the averaged zonal winds from ECMWF for the duration of the flight, and the minimum and maximum values throughout the ECMWF domain. The increasing ECMWF zonal winds correlate with the increasing vertical wavelength observed in the Rayleigh lidar above 20 km. It should be noted that a decreasing mean temperature above the stratopause would cause a smaller N and an increase in λ_z with altitude, whereas an expected reduction of the zonal wind would cause a decrease in λ_z with altitude.

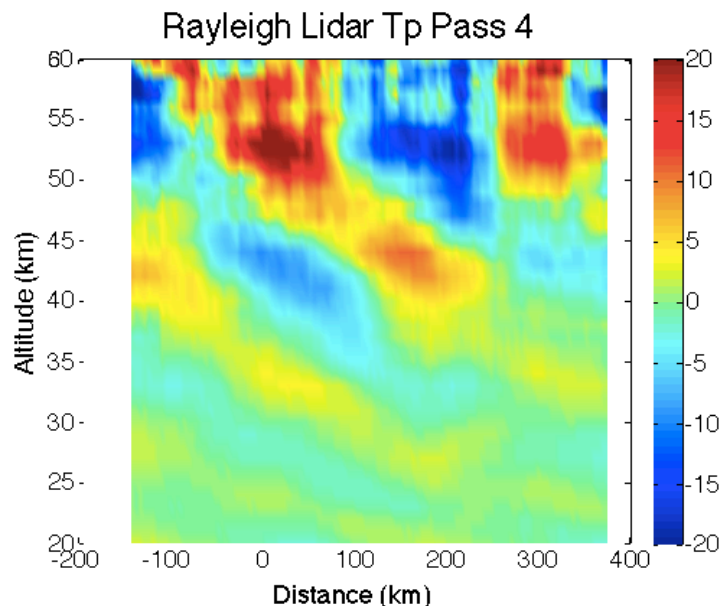


Figure 4.21: Rayleigh lidar temperature perturbations from the fourth pass show a vertical wavelength of ~ 20 km.

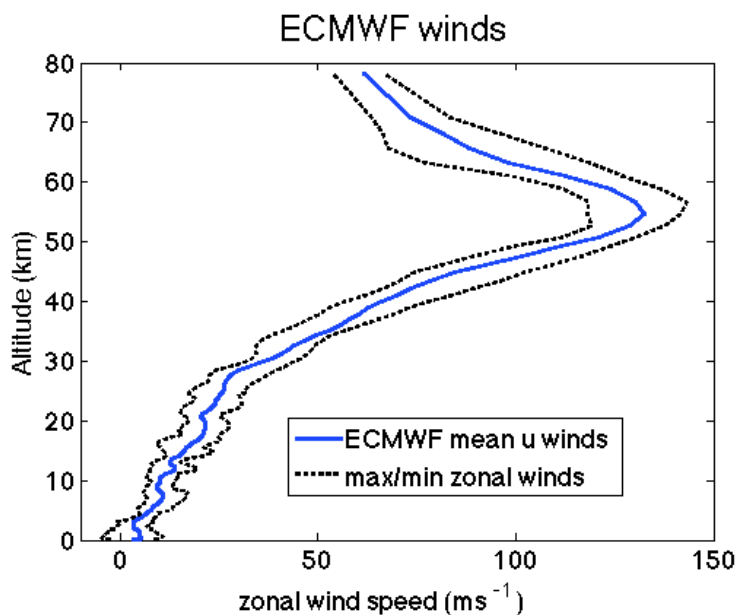


Figure 4.22: ECMWF winds averaged over the duration of the flight with the maximum and minimum winds included for reference.

DEEPWAVE forecasts by the ECMWF model agree reasonably well with the T' fields obtained with the Rayleigh lidar and suggest refraction to somewhat smaller $\lambda_z \sim 20$ km above

60-km altitudes, apparently in response to the influences of weakening zonal winds above. Additionally, ECMWF predicts that the particular conditions allowing the large-scale ~ 240 km MW to propagate to high altitudes existed for approximately two days, beginning on the 12th of July. Figure 4.23 shows ECMWF winds at 43° S along the flight path during the approximate time of RF22.

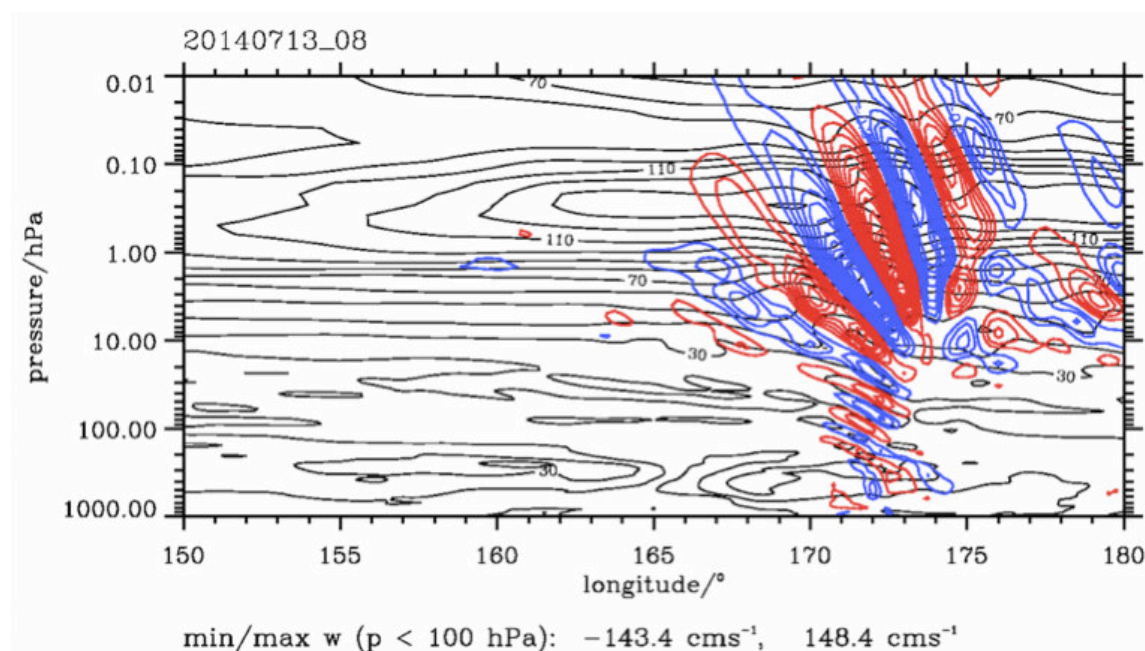


Figure 4.23: ECMWF wind perturbation output at 43°S during the time of RF22

While data from the Rayleigh lidar at the nearby Lauder station were unavailable during the RF22 flight, these data were available for the 12th of July. These provide a good estimate of local temperatures between 60 and 85 km during RF22, given that ECMWF predicts that this event extends over these two days. Furthermore, SABER temperatures are available nearby at $\sim 12:30$ UT on the 13th of July, just a few hours after the RF22 flight. These temperatures also provide an estimate of the large-scale temperature environment within which these DEEPWAVE measurements were performed. Differences of the Lauder lidar profiles from the SABER profiles

then provide indications of local variations that may be largely due to MWs. Figure 4.24a shows the individual mean temperature profiles for the two SABER profiles. Figure 4.24b shows the nightly average of the Lauder Rayleigh lidar temperatures with the mean SABER temperatures. Both the lidar and SABER show a strong negative gradient in temperature between ~ 70 -80 km. However, this differs in altitude between the two measurements. The lidar shows this low stability layer to extend from ~ 70 -77 km and SABER shows it to extend from ~ 77 -82 km. Both the lidar and SABER show a positive temperature gradient from ~ 80 -90 km. The difference between these measurements likely indicates local influences of the MW in the lidar data, which likely makes little contribution to the limb-averaged SABER profiles. The weakly stable layer in the lidar profile between ~ 70 -80 km, suggests the likely occurrence of MW breaking at these altitudes during these times.

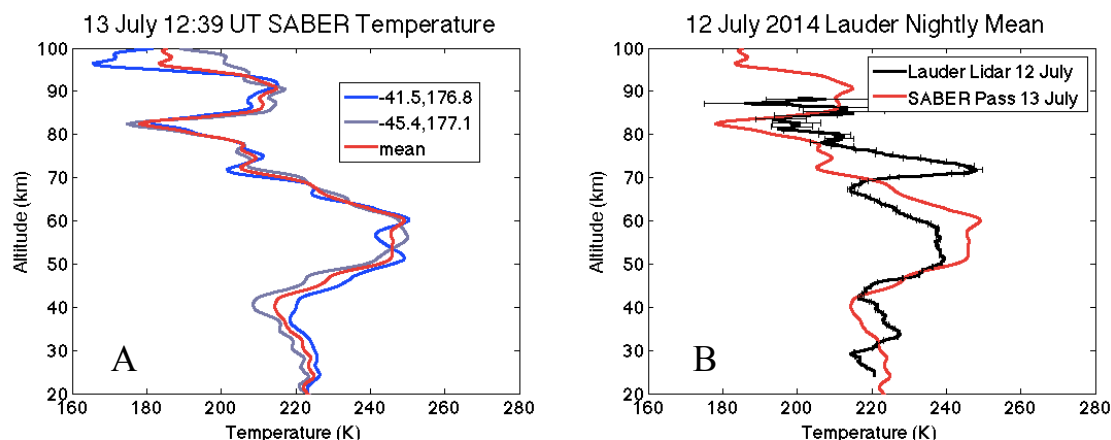


Figure 4.24: Plot A shows Saber temperatures from two passes on 13 July 2014 at 12:38:21 and 12:39:31, and the averaged temperature between these passes. Plot B shows the nightly average from the Lauder Rayleigh Lidar on 12 July 2014 plotted with the averaged SABER temperature from plot A.

The hydroxyl layer images shown in Figure 4.25 include the GV AMTM and wing camera horizontal map of OH airglow brightness along and across the flight track for flight segment 4. The horizontal dimensions of this field are ~600 km east-west and ~900 km north-south. Seen clearly are three large-scale bright regions oriented nearly north-south, with the stronger central feature crossing the center of South Island. Temperature keograms from the AMTM are shown for each pass in Figure 4.26. Comparing the brightness and temperature fields for flight segment 4, the regions of warmest temperatures correspond closely to the regions of maximum brightness. The particular features of greatest interest in this paper also occur in the brightest, and apparently warmest, and largest amplitude, phase of the ~240 km MW. The along-track AMTM temperatures reveal the presence of smaller-scale GWs with $\lambda_h \sim 25\text{-}28$ km primarily within the bright and warm phases of the ~240 km MW on each flight segment. These smaller-scale features and their corresponding *MF* contributions will be discussed in chapter 5. However, it is important to note here their interesting presence in the warm phase of the ~240 km MW.

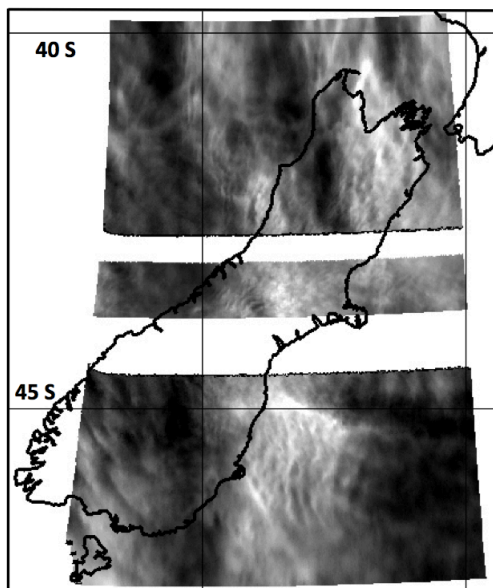


Figure 4.25: Imager intensities from the fourth pass of RF22 using the AMTM and side viewing IR cameras. These intensities show the ~240 km MW positioned over the South Island of New Zealand and spanning ~900 km meridionally.

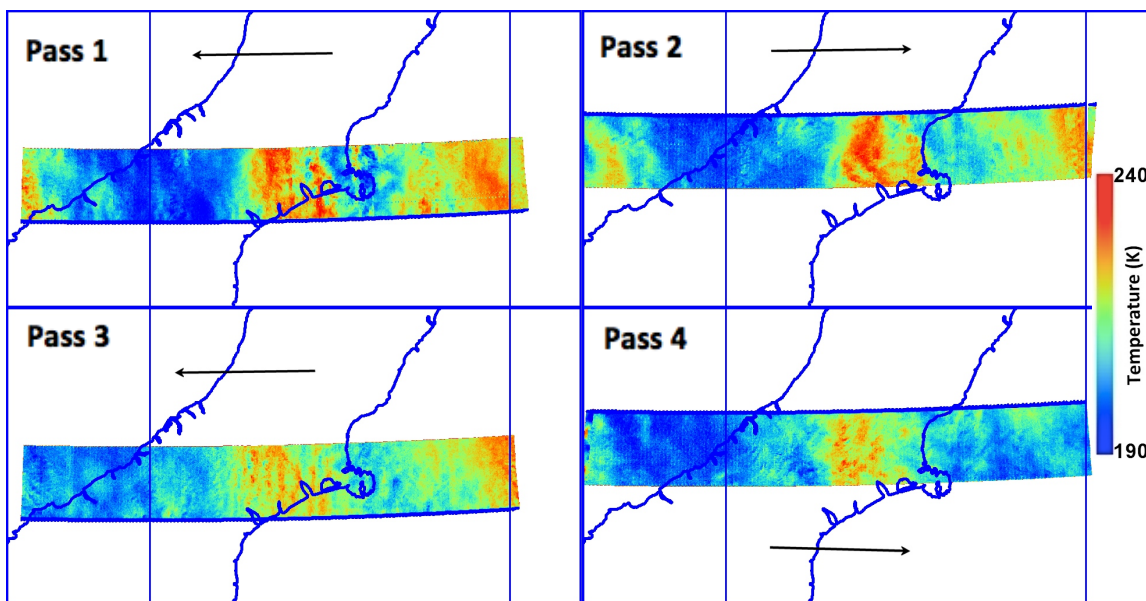


Figure 4.26: AMTM spatial keograms showing both the 240 km MW centered over New Zealand and several smaller-scale GWs.

A rough prediction of winds for the time period of RF22 is obtained from the Kingston meteor radar over Tasmania. While these radar winds are ~ 2000 kilometers away from the measurements over New Zealand, they provide a reasonable estimate of the mean winds and tidal influences at the altitudes, latitude and local time of measurements made with the GV. A 6-hr mean wind starting at 6:00 UT is shown in Figure 4.27. These measurements suggest a mean wind of about $\sim 25 \text{ ms}^{-1}$ towards the east near 87 km at the peak of the hydroxyl layer. These measurements shown in Figure 4.26 reveal a wind that decreases to near $\sim 0 \text{ ms}^{-1}$ close to 90 km. This near zero wind implies a critical level for MW approaching the MLT. As shown by equation 2.21, the vertical wavenumber becomes infinite as $c \rightarrow u$, which causes the vertical wavelength to approach zero.

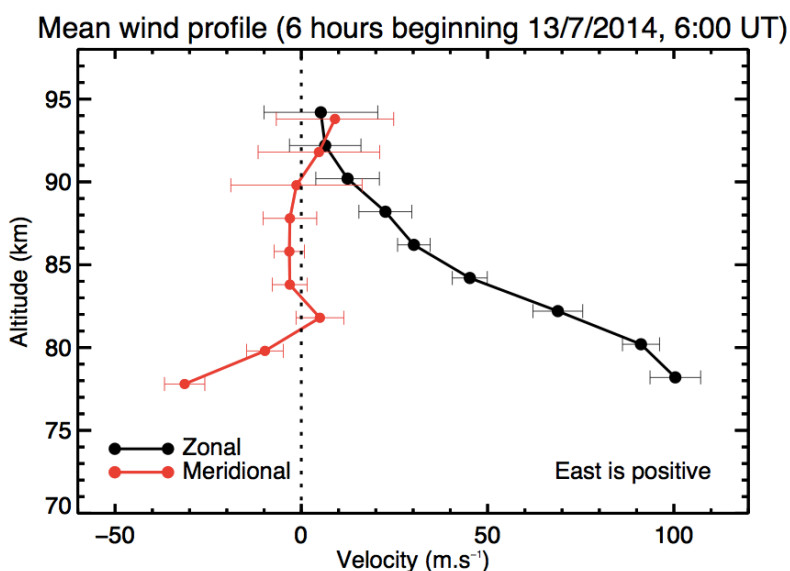


Figure 4.27: Kingston meteor radar wind 6-hour mean starting at 6 UT on 13 July 2014 show winds of 45 ms^{-1} towards the east at 84 km and 25 ms^{-1} towards the east at 87 km.

Sodium mixing ratios computed along this flight provide additional insights into the evolution of the ~ 240 MW in altitude and time. For this section, the sodium mixing ratios are provided for pass 1 and 4 to provide an idea of the vertical propagation conditions that the ~ 240 km GW is undergoing. The sodium mixing ratios and their use in estimating the MF for each pass are discussed in more depth in chapter 5. Figure 4.28 shows the sodium mixing ratio contours for which a horizontal averaging of ~ 45 km has been employed. While these contours do not have the resolution to show smaller-scale GW activity, they clearly demonstrate the ~ 240 km MW observed on each pass. The contours show that the large-scale MW has an appreciable amplitude up to ~ 80 km but has largely dissipated by ~ 87 km. The inferred decrease of the ~ 240 km MW amplitude over this altitude interval, and the near-vertical Na mixing ratio contours suggest possible MW breaking and overturning, and appear to be consistent with the observation by both the Lauder lidar and SABER of a layer of low stability located near ~ 70 - 80 km, and the observation by the Kingston radar of a critical level for MWs near 90 km altitude.

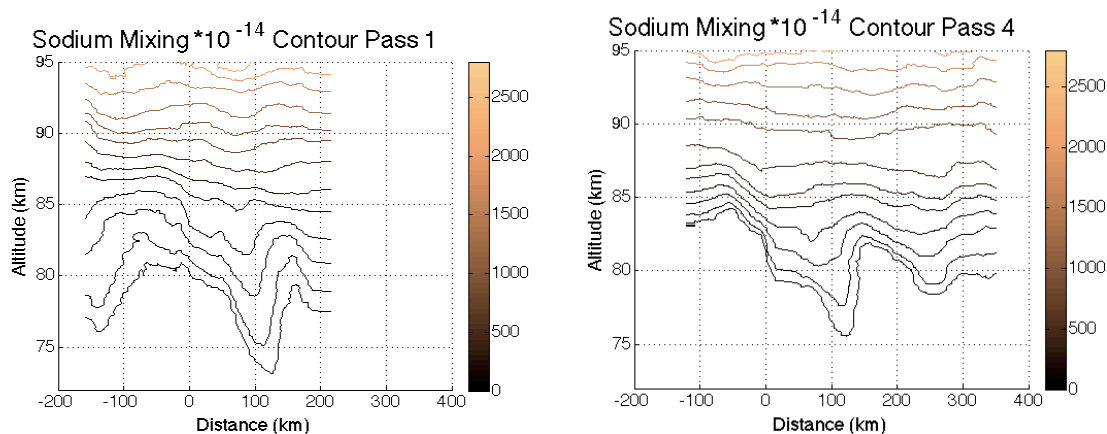


Figure 4.28: Sodium mixing ratio contours for Passes 1 and 4 during 13 July 2014 flight.

The sodium mixing ratios show dissipation of the ~240 km MW and evidence of a critical level as predicted by the radar winds. This near zero wind close to 90 km would also create a critical level for other smaller scale GWs and MWs with similar phase speeds and characteristics to the ~240 km MW. Other small-scale GW events were observed during this research flight. During the fourth flight pass a smaller-scale GW with zero phase speed was observed. This GW appeared to have a more incoherent structure. Figure 4.29 shows the overhead AMTM view of this GW from pass 4 next to the corresponding sodium densities and sodium mixing ratios from the same horizontal flight section as well as the keogram for the flight pass for comparison.

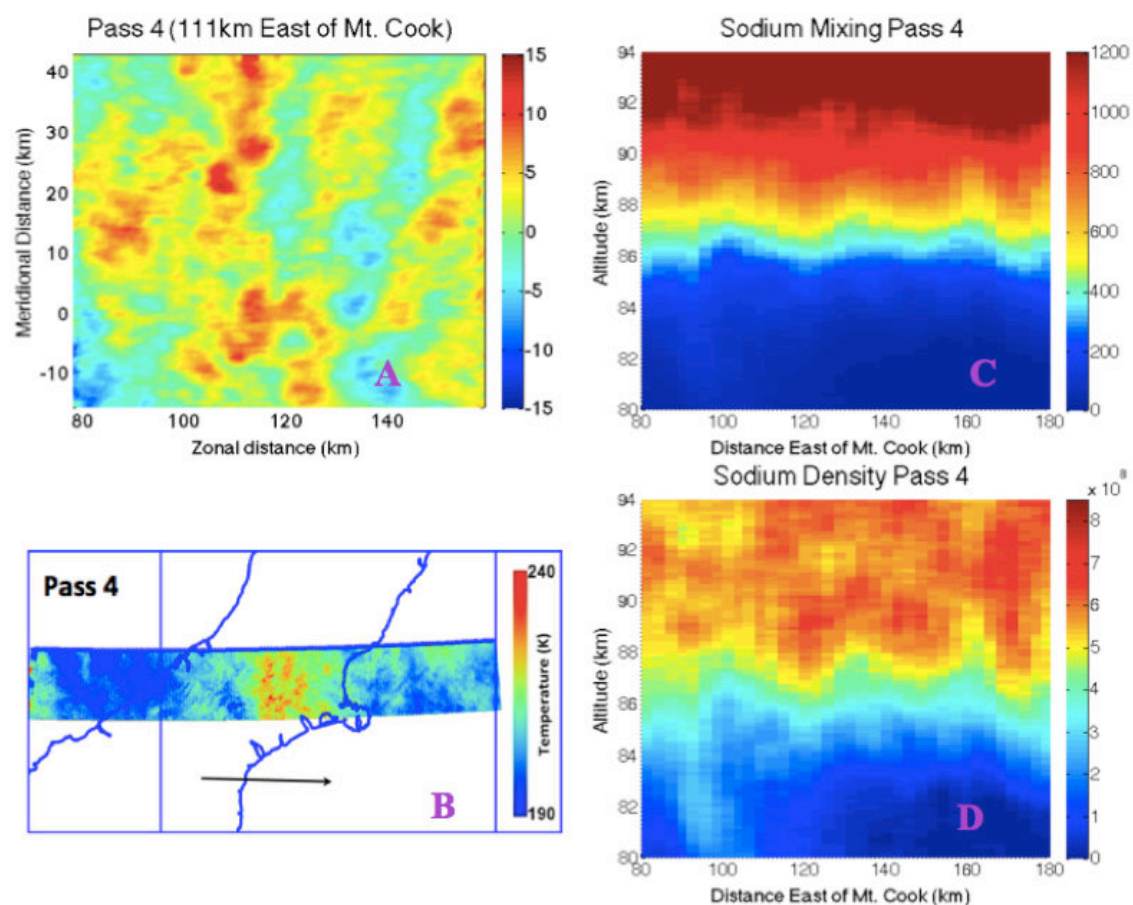


Figure 4.29: Small-scale GW observation from pass 4 during the 13 July 2014 flight. Figure A shows the AMTM observation of the overhead GW. Figure B shows the keogram for comparison. Figures C and D show the sodium mixing ratio and sodium density for the corresponding horizontal cross section of the AMTM spatial view.

The sodium densities and mixing ratios in Figure 4.29 use a 6 km horizontal averaging and 1.2 km vertical averaging so that smaller-scale features can be observed. These densities show clear perturbations corresponding to a horizontal wavelength of $\sim 25\text{-}30$ km, which is similar to the observed GW in the AMTM. It is difficult to make a direct association between the AMTM and the sodium mixing ratios given the variable extent of the GW observed in the AMTM, and the aspect that the sodium data was taken over a range of times whereas the AMTM

image is at one single time. However, it is still clear that there is small-scale GW activity of similar scale in both the AMTM and the sodium mixing ratios. Furthermore, the GW observed in the AMTM has a phase speed of $\sim 0 \text{ ms}^{-1}$ meaning that it would likely be approaching critical level near 90 km similar to the $\sim 240 \text{ km MW}$. Assuming that the GW observed in the sodium densities is of similar character, it would also be approaching a critical level. As seen in Figure 4.29 C and D, perturbations are clearly seen in the sodium densities near 86 km, but these perturbations have largely dissipated by 92 km. Figure 4.29 D shows some evidence of a shallowing vertical wavelength above 86 km also indicative of a critical level approach. Given these observations, it is reasonable that this smaller-scale GW observation is also approaching a critical level similar to the $\sim 240 \text{ km MW}$.

These observations show the important role that background environment plays in GW propagation and breaking, and the contributions that critical levels make to GW breaking in the MLT. Additionally, the small-scale GWs analyzed for the flight segments all occurred in the warm phase of the $\sim 240 \text{ km MW}$, implying a significant influence of the $\sim 240 \text{ km MW}$ on the small-scale GW propagation and refraction with altitude. These cases are very similar to that observed at ALOMAR on 27-28 January 2014. In that case, the larger GW scales within the multi-scale GW field were found to strongly modulate the smaller-scale GW occurrence and amplitude, also leading to a very large momentum flux estimate. Thus these observations of similar dynamics during DEEPWAVE appear to be further evidence of the importance of such multi-scale dynamics that likely play major roles in the composition of the GW spectrum with altitude and the determination of the GWs that contribute most to momentum fluxes in the MLT.

1 July 2014 Observed Critical Level

During the first few passes of lidar observations on 1 July 2014 (RF14), a MW was observed in both the AMTM and the sodium lidar with a horizontal wavelength of ~ 100 km. This MW appeared to displace to the sodium layer down to ~ 74 km in some instances, but was not visible above ~ 84 km. There were also several scales of smaller GWs present as well, which are visible in both the AMTM and sodium lidar, but sodium displacements below 80 appear to largely correspond to the ~ 100 km MW. Figures 4.30 and 4.31 show panels of sodium lidar densities, mixing ratios, and temperatures, and AMTM temperature keograms for the first two passes across the island where the lidar was running. The MW is most clear during the first pass, and becomes less defined during the next pass. This MW is not clear in the sodium temperature measurements, however it is difficult to make an assertion about whether or not these temperatures are accurate because they are not continuous spatially at altitudes where the MW is most visible below 82 km, and the errors are larger at these lower altitudes where the densities are smaller. The AMTM gives a low end estimate of temperature perturbations including averaging over the layer, and shows peak to peak temperature perturbations of up to ~ 17 K on the first pass and ~ 12 K on the second pass. The AMTM keograms also show this MW to have phase fronts aligned North-South, implying a zonal propagation.

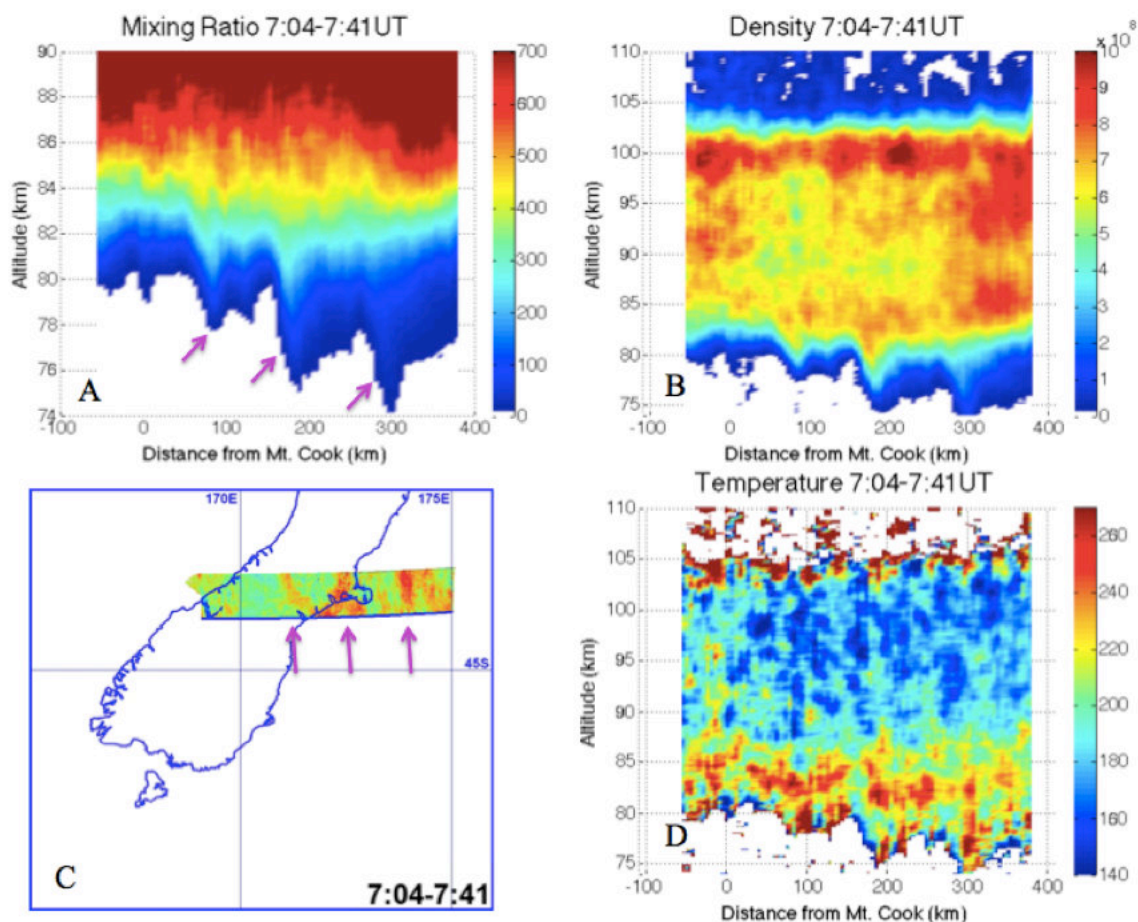


Figure 4.30: Above plots show data from the 1 July 2014 flight. Plot A shows the sodium mixing ratio indicating large perturbations for the ~100 km MW below 82 km, and no signal of this MW above 84 km. Plot B similarly shows density perturbations of the ~100 km MW that extend down to 74 km but are not visible above 84 km. Plot C clearly shows the ~100 km MW temperature perturbations in the AMTM. Plot D shows the corresponding lidar temperatures, which indicate no temperature perturbations due to the ~100 km MW above 84 km.

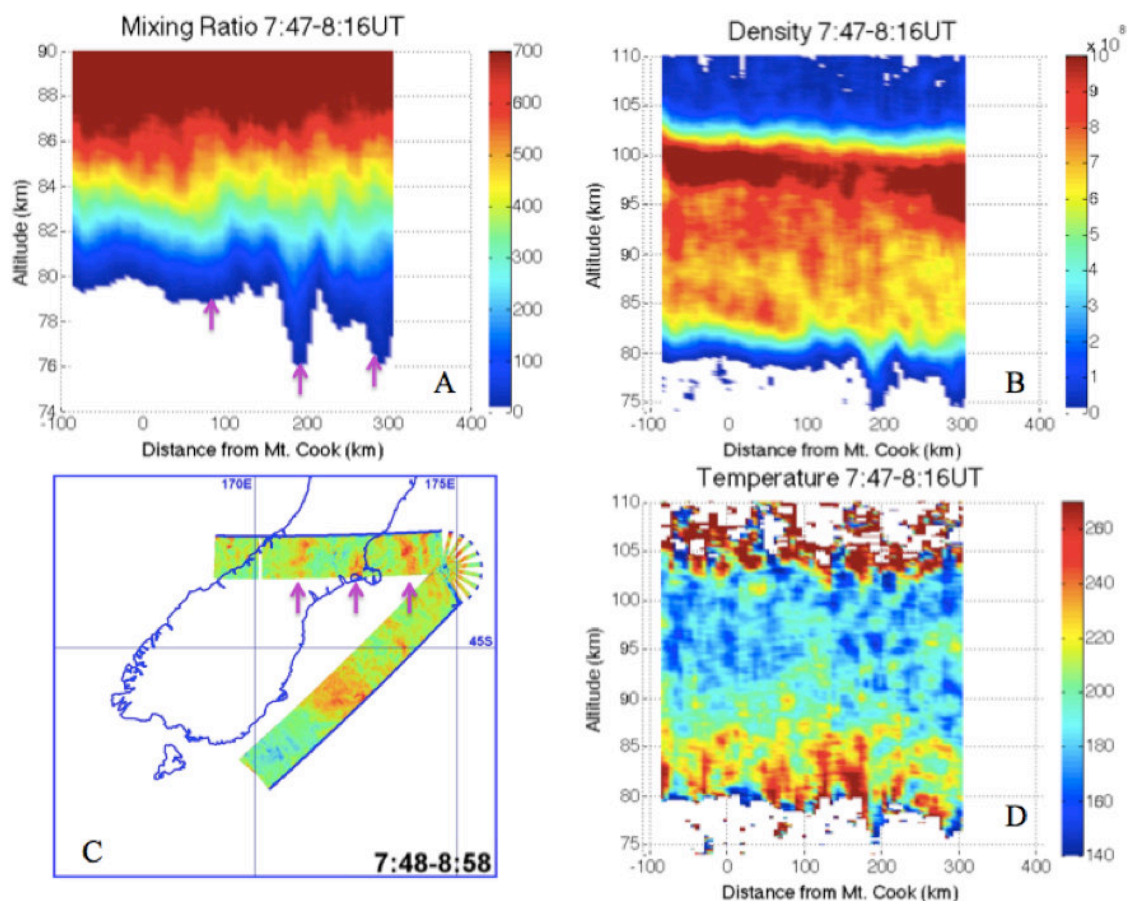


Figure 4.31: Same Figure 4.30, but for the return pass over the island during the 1 July 2014 flight. These plots indicate a less defined ~ 100 km MW, but evidence is still visible in the sodium densities and AMTM temperatures.

As was previously used for the 13 July analysis, the Kingston meteor radar gives an idea of mean winds and tidal structure for this approximate latitude. Figure 4.32 shows a 6-hour average of these winds surrounding the time of these measurements, as well as a 6-hour average two hours ahead of the measurements to account for tidal differences between the lidar measurements over New Zealand and the meteor radar measurements over Tasmania.

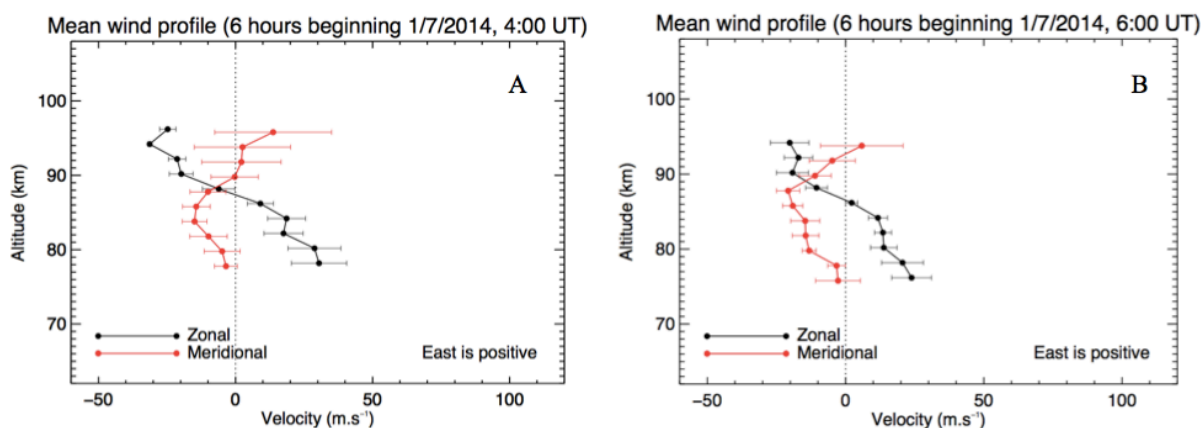


Figure 4.32: Kingston meteor radar winds on 1 July 2014 both at the time of the measurements during the observed MW, and two hours ahead of the measurements to account for tidal differences between the meteor radar site at Tasmania and the South Island of New Zealand. Both measurements show a clear critical level for MW aligned zonally near 85 km in altitude.

The meteor radar winds show a distinct critical level at 85 km for zonally propagating MWs during both averaging time segments. The measured winds also show a wind environment with stronger winds that would be conducive to MW propagation near 80 km. These measurements match with lidar observations for this time period, which clearly show strong MW perturbations in the sodium densities below 82 km, but no evidence of the MW above 84 km. A critical level at 85 km would account for the rapid dissipation of the observed MW up to this altitude.

4 July 2014 Observed Critical Level

The research flight that took place on 4 July 2014 occurred during a high forcing day. During some passes of this research flight (RF16), it appears that some of the MWs generated during the high forcing event reached the MLT region. These observations were strongest during the times between 8-10UT. Figure 4.33 shows temperatures, densities, and mixing ratios observed by the sodium lidar, and corresponding OH images for the pass from 8:20-8:50 UT which saw the strongest MW response. The following pass from 9:00-9:44 UT observed multiple smaller scales of GWs overhead, some propagating, and a few phases of a stationary MW towards the western edge of the pass. In the north viewing OH camera for this second time period, a sharp saw tooth MW was observed, indicative of MW breaking. These OH images and the corresponding sodium densities, which resolve the smaller scale features that sodium temperatures cannot resolve, are shown in Figure 4.34. For comparison, OH imager keograms from passes earlier and later in the evening are shown in Figure 4.35. These keograms indicate that there was not pronounced MW activity before and after these observations of strong MW activity in the MLT region.

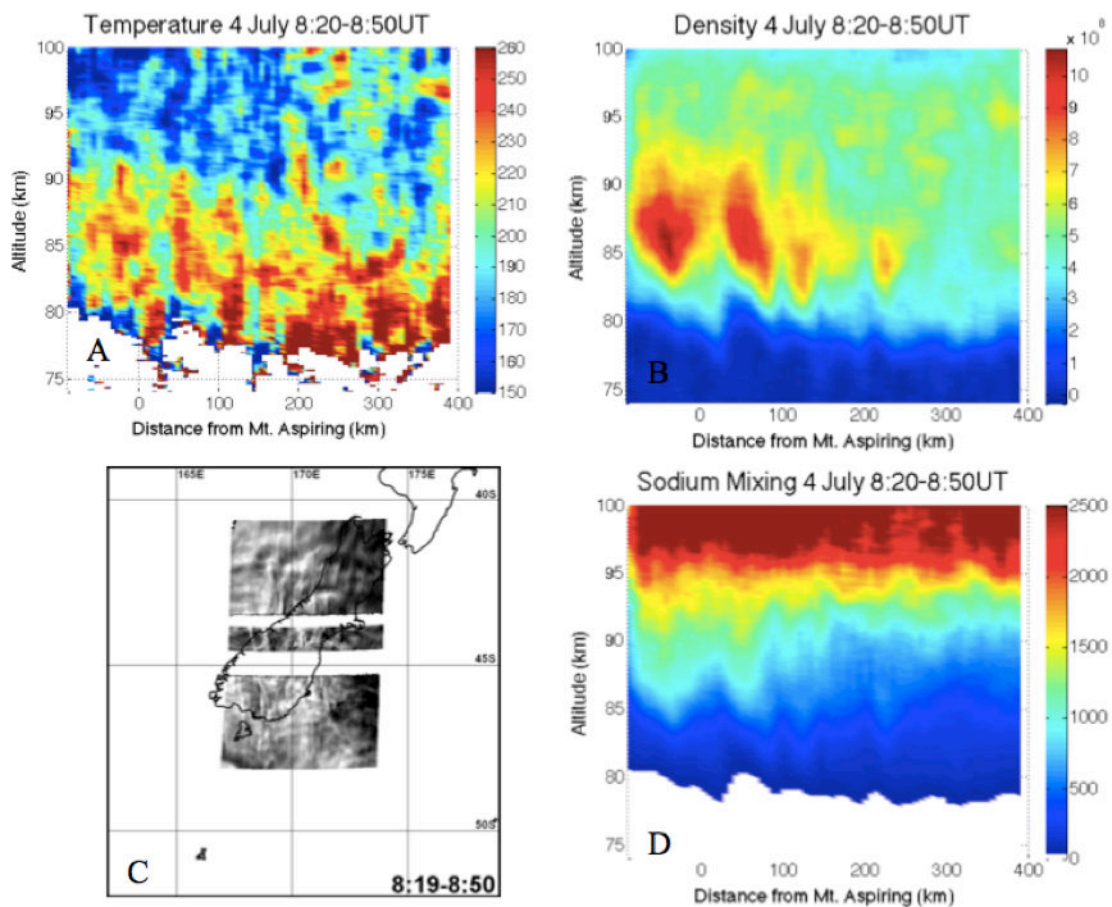


Figure 4.33: Plots for the 4 July 2014 flight. Plot A shows temperatures measured from the sodium lidar. Plot B shows the sodium densities and D shows the mixing ratios computed from these densities. Plot C shows the OH imager keograms.

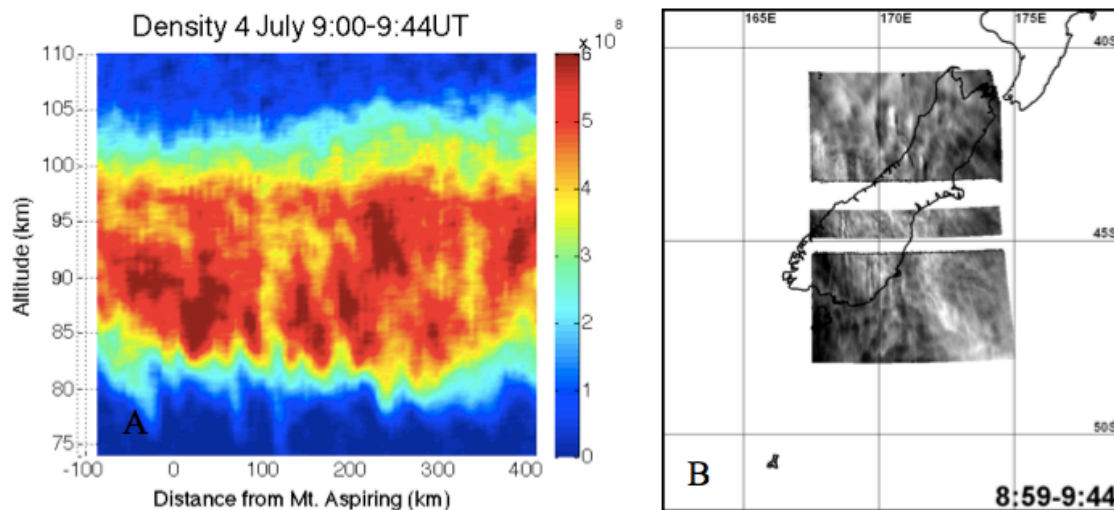


Figure 4.34: Plots from the 4 July 2014 flight. Plot A shows sodium densities. Plot B shows the corresponding OH imager keogram.

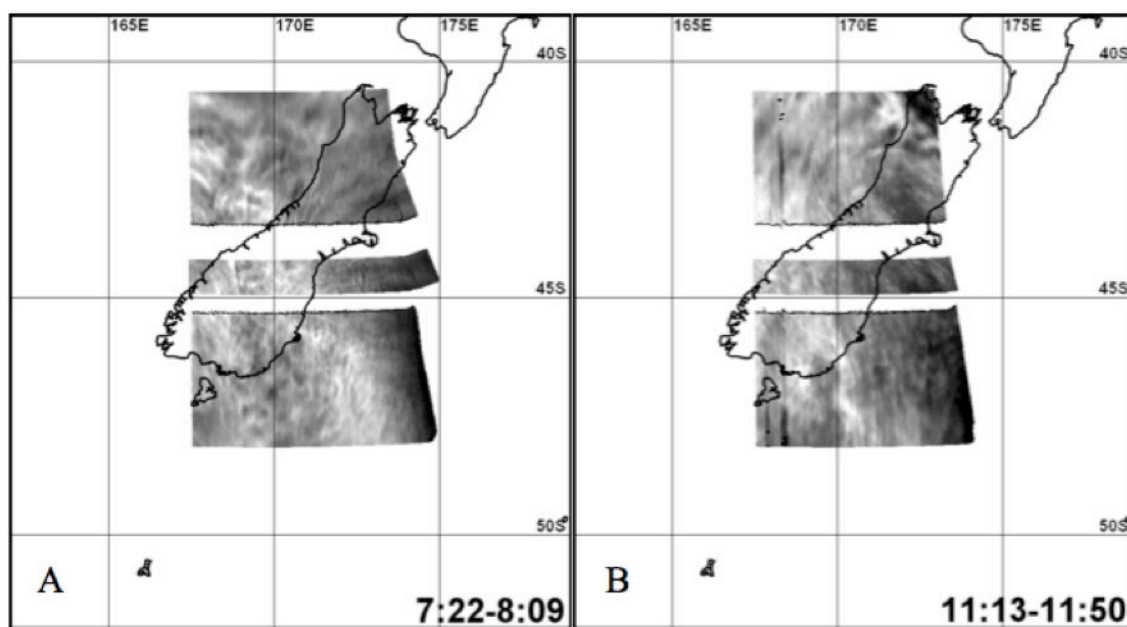


Figure 4.35: Plots A and B show the OH imager keograms at times before and after the observed strong MW activity on 4 July 2014.

The winds observed by the Kingston radar on this evening are shown in Figure 4.36a. The radar shows relatively weak eastward winds throughout the evening. Two 6-hour averages are given, both at the time of observations and 2 hours ahead to account for tidal differences shown in Figures 4.36b and 4.36c.

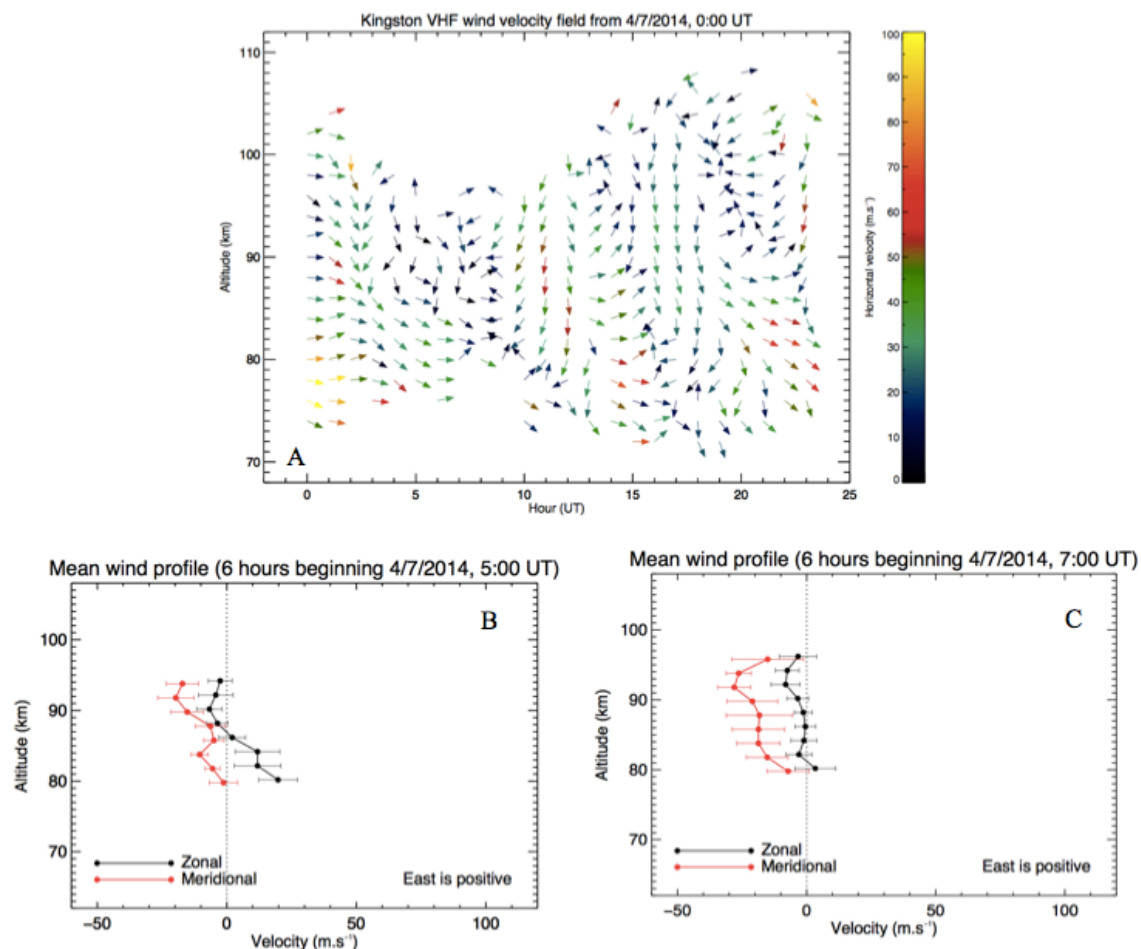


Figure 4.36: Plots of Kingston meteor radar winds during 4 July 2014. Plot A shows wind vectors for the entire night. Plot B shows a 6-hour average surrounding the time of observation. Plot C shows a 6-hour average 2 hours ahead of the MW observation time to account for tidal differences between the DEEPWAVE observations and Kingston radar observation site.

The radar wind averages indicate almost no wind in the eastward direction, or a critical level between 80 and 90 km. Given the MW observations, it is clear that there must be an eastward wind for some time through altitudes up to 90 km. However, this need only be intermittent and not for the longer measurement period of the radar. As shown in Figure 4.34b, a MW is observed only in certain regions of the FOV of the OH imager, indicating that conditions even across a spatial extent on one given pass can vary significantly enough to alter the conditions to either allow or prevent MW propagation to this region. Furthermore, strong MW activity was not observed at earlier or later times during the flight, which is to be expected for near zero winds in the MLT. Both Figures 4.33 and 4.34 show sharp sawtooth patterns in the imager, which is seen with breaking GWs. Also, the sodium densities and temperatures show little evidence of the large MW observed from 8:20-8:50 above 90 km. Given the background wind conditions, it is likely that the winds allowed for these MWs to propagate to higher regions within the MLT for a period of time, and that these MWs were encountering a critical level somewhere near 90 km or lower.

4.3 Summary of Gravity Wave Propagation Due to Variable Background

Environments

The above studies yield insight into different propagation conditions for GWs, and the conditions under which momentum is transported into the MLT region of the atmosphere. Complex and evolving MLT environments can cause small-scale GW to be ducted over large scales and time periods. These GWs can be readily resolved in the AMTM, and may even appear to be propagating over the observation altitude of the AMTM. However, it is important to note

the wider vertical conditions of the background atmosphere that may lead to ducting conditions. These observed ducted GWs should not be mistaken for freely vertically propagating GWs as ducted GWs do not make contributions to the vertical *MF*. The sodium lidar provides further insight through both wind and temperature measurements as well as high-resolution density measurements that can depict where small-scale GWs may be propagating within the layer.

Larger-scale dynamics can also provide ideal conditions for small horizontal-scale, high *MF* GWs to propagate into the MLT. This is evidenced by the 27-28 January 2014 observation at ALOMAR where the 1-hr and 12-hr GWs both strongly influence the propagation environment of the 10-minute period GW. In addition to this observation, the DEEPWAVE research flight on 13 July 2014 also noted smaller-scale GWs that similarly appeared to be correlated within a phase of a larger-scale GW. This implicates the role of multi-scale dynamics with contributing to the GW spectrum observed within the MLT.

Many environmental conditions also lead to GW breaking in the MLT, which in turn deposits momentum. Critical levels provide a boundary to GW propagation, as shown by several DEEPWAVE observations. The events on the 1st and 4th of July 2014 demonstrate that decreasing winds within the MLT create a critical level that can prevent MW propagation to higher altitudes. The event on 13 July 2014 showed that low forcing conditions allowed for a sustained MW to reach MLT altitudes before breaking due to the critical level conditions within this region. The momentum deposition of the multi-scale GWs during the 13 July event, and the impact this has on the MLT will be discussed in the following chapter.

5. Small-Scale GW Forcing in the Mesosphere and Lower Thermosphere

GWs having horizontal wavelengths of a few 100km or less account for significant MF . As equation 2.23 shows, as horizontal wavelength decreases, k increases, and the overall MF increases for other parameters constant. Similarly, as the vertical wavelength increases, the MF increases. Thus small horizontal-scale GWs with large vertical wavelengths are believed to make a major contribution to the total MF throughout the atmosphere.

Mean MF estimates in the MLT have been obtained using various instrument techniques. Radar measurements have yielded mean MF magnitudes of $\langle u'w' \rangle \sim 1-20 \text{ m}^2\text{s}^{-2}$ [Vincent and Reid, 1983; Fritts and Vincent, 1987; Reid et al., 1988; Tsuda et al., 1990; Wang and Fritts, 1990; Hitchman et al., 1992; Fritts et al., 2010; Murphy and Vincent, 1993; Nakamura et al., 1993]. Various satellite instruments have yielded global MF means ranging from $\sim 1-8 \text{ m}^2\text{s}^{-2}$ in the MLT [Ern et al., 2011].

An example of a small-scale GW attaining a large MF is seen in the 27-28 January 2014 ALOMAR case of the 10-minute period GW discussed in section 4.2.2. The MF estimate for this GW is discussed by Fritts et al. [2014]. The GW, shown in Figure 4.11, had a temperature perturbation T' of 19.3K and a vertical wavelength $\lambda_z = 17.6 \text{ km}$, and additional parameters discussed in chapter 4 ($N \sim 0.0146 \text{ s}^{-1}$, $\lambda_h = 24 \text{ km}$, $c = 45 \text{ ms}^{-1}$, and propagating towards 70° E of N). The result was a MF of $\sim 940 \text{ m}^2\text{s}^{-2}$, which is possibly 50-100 times typical mean MF estimates for this altitude. Measurements like this reveal the importance of small horizontal-scale GWs in the MLT momentum budget. The following sections provide more in-depth studies of localized, small horizontal-scale GW events and their associated MF s.

5.1 GW Momentum Transport in a Multi-Scale Environment

(13 July 2014 DEEPWAVE Campaign)

The DEEPWAVE research flight on 13 July 2014 over Mt. Cook observed a sustained ~240 km MW as well as multiple small-scale GWs during each pass. There were 4 successive flights over Mt. Cook between 6 UT and 9 UT. The ~240 km MW observation and the critical level that this MW encountered near 90 km were discussed in chapter 4. In the following subsections, the environment and the observed GWs are further characterized, and the corresponding *MFs* are assessed.

Background environment

The background temperature profile was estimated given the information from the Lauder Rayleigh lidar and SABER temperature measurements. Above the nearly adiabatic layer from ~70-80 km, a weakly positive temperature gradient above 80 km is assumed. The nightly average from the AMTM was found to be 212 K, and that from the Lauder Rayleigh lidar at ~80 km was ~195 K. SABER measurements at 12:39 UT and located at -41.5° , 176.8° and -45.4° , 177.1° as previously shown in Figure 4.24 showed a temperature of 194 K at 80 km and 211 K at 87 km. While both of these measurements include smaller-scale fluctuations, especially localized MWs in the Lauder lidar data, a reasonable approximation to the background temperature gradient can be inferred. Using SABER, AMTM, and lidar measurements, an approximate mean temperature gradient from 80-87 km of $\sim 2.5 \text{ K km}^{-1}$ is inferred. This results in an estimate of the mean buoyancy frequency between ~80 km and 87 km of $N \sim 0.023 \text{ s}^{-1}$ (e.g from equation 2.15).

The background wind was obtained using the Kingston radar. For the purposes of this analysis, it is assumed that the stationary MWs are largely observed towards the bottom side of

the OH layer near 84 km, as these MWs are likely approaching a critical level near 90 km where the mean winds approach 0 ms^{-1} . Furthermore, the sodium mixing ratios confirm that the amplitude of the $\sim 240 \text{ km}$ MW decreases rapidly above 85 km as was previously shown in Figure 4.28. For the smaller-scale waves, it is assumed that those with observable phase speeds towards the east (not MWs) are weighted towards the center of the OH layer as they are not approaching a critical level. For this reason, a background wind at two different altitudes is assumed depending on the GW analysis; 87 km and 84 km, where the winds are ~ -25 and -45 ms^{-1} respectively.

240 km MW characterization and MF estimation

The temperature perturbations for the $\sim 240 \text{ km}$ MW were found by subtracting the mean temperature for each flight segment. Smaller-scale perturbations were removed from the $\sim 240 \text{ km}$ GW using a smoothing spline fit to generate a low-pass output of the $\sim 240 \text{ km}$ MW and an estimate of the temperature perturbations. It can be assumed that the temperatures measured by the AMTM are largely weighted towards the MW perturbations seen below $\sim 85 \text{ km}$ because of the expected strong phase averaging at higher altitudes. These temperature perturbations are thus likely to be a significant underestimate of the actual temperature perturbations between 80-85 km due to averaging within the OH layer. However, given the lack of information about the shape of the OH layer in the complex mixing environment accompanying breaking and dissipation at these altitudes, a correction factor may provide an inaccurate and potentially large overestimate of the temperature perturbation. Thus, the *MF* for the $\sim 240 \text{ km}$ MW for each pass was calculated using equation 2.23, the observed AMTM temperature perturbations, and other parameters specified above. The $\sim 240 \text{ km}$ MW parameters and corresponding *MF*s calculated from the AMTM are summarized in Table 5.1. These varied from $3\text{-}6 \text{ m}^2\text{s}^{-2}$ and are similar to mean values

at this altitude. As noted above, however, these values are likely significant underestimates of the MF of the ~ 240 km MW where its amplitude is larger than the estimates from the AMTM listed in Table 5.1.

Table 5.1: 240 km MW temperature perturbations and corresponding MF near 84 km

Pass number	$\langle T' \rangle$ [K]	MF [$m^2 s^{-2}$]
1	8	6
2	7	5
3	6	3
4	8	6

The sodium mixing ratios provide an alternate means of estimating temperature perturbations of the ~ 240 km MW at these altitudes. The sodium mixing ratios calculated for each of the four flight passes are given in Figure 5.1. The mixing ratio yields a relative parcel displacement, and from this a temperature perturbation can be calculated. The displacements of mixing ratio contours at ~ 83 km for each pass are summarized in Table 5.2. Using an adiabatic lapse rate of 9.5 K km^{-1} and the background temperature gradient of $\sim 2.5 \text{ K km}^{-1}$, a temperature perturbation estimation can be obtained, and these estimates are also given in Table 5.2. The winds near ~ 83 km are used, which are 55 ms^{-1} towards the east, in order to calculate the MF here. The MF values are summarized in Table 5.2. These values are larger than mean MF values and range from $17\text{-}68 \text{ m}^2\text{s}^{-2}$, which suggest strong variations in propagation conditions of the ~ 240 km MW on each pass. The differences in temperature measurements between the AMTM and sodium mixing ratio are due to the averaging associated with the AMTM, and its likely small contribution from the lower altitudes where the ~ 240 km MW is large, given that the OH layer appears to be centered where we see little to no perturbations in the sodium mixing ratios.

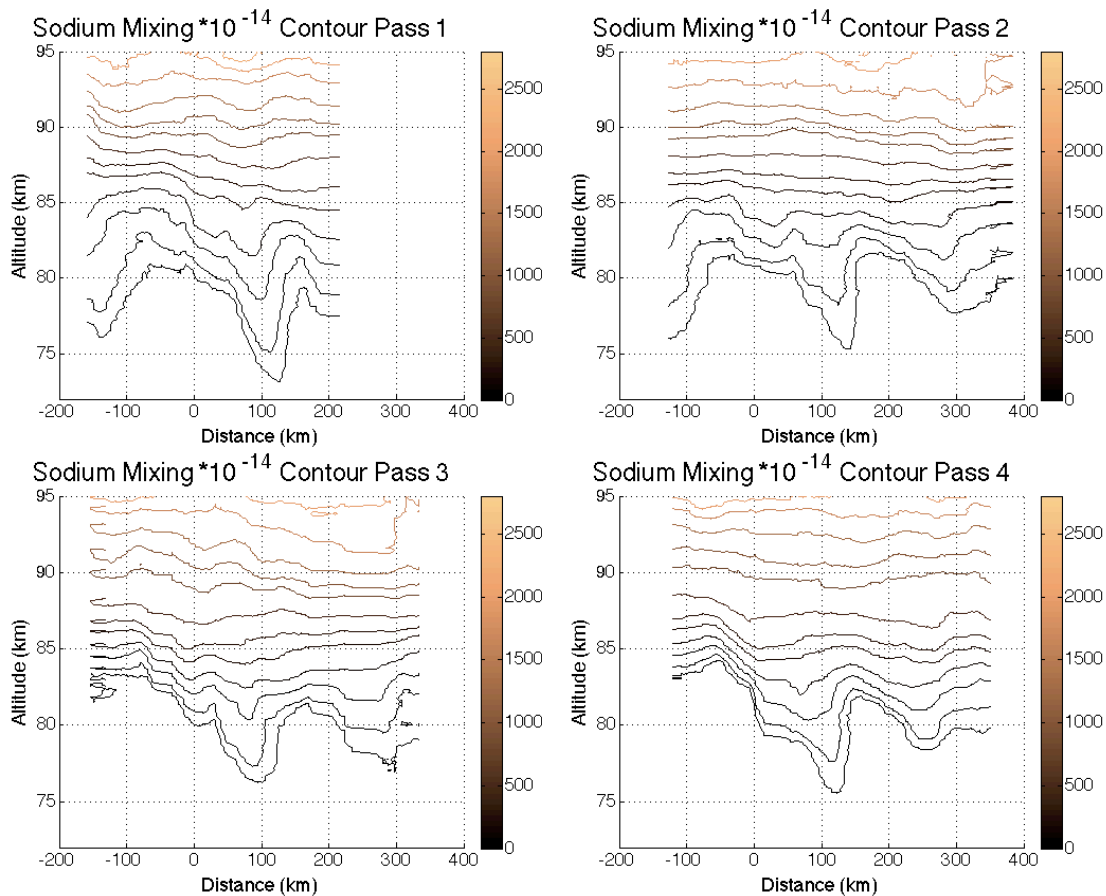


Figure 5.1: Sodium mixing ratios from the GV sodium lidar for the four RF22 flight segments on 13 July 2014 clearly show the ~ 240 km MW below 85 km, and strong dissipation of this MW above 85 km.

Table 5.2: 240 km MW mixing ratio vertical displacements near 83 km.

Pass #	dz [km]	T' [K]	MF [$m^2 s^{-2}$]
1	2	24	68
2	1.5	18	38
3	1	12	17
4	1.5	18	38

It is important to place bounds on MF measurements, especially with the errors that can arise in each aspect of individual measurements. As discussed above, a direct measurement of T' from the AMTM gives an underestimate of the actual T' of the GW due to averaging over the OH layer. In this way the AMTM measurement allows a lower bound to be placed on MF measurements. However, there may still remain significant errors that cannot be addressed with traditional error analysis. Propagation of error assumes a small error perturbation about the mean or true value, and very large errors result in this method being an inaccurate way to bound measurements. While the AMTM measurements may provide us with a lower estimate of MFs , an upper bound can be assessed using the environmental conditions of GW propagation, and the upper limit imposed by GW saturation as discussed in Fritts [1984b] where $u' < (c-u)$.

In this case, MWs approaching a critical level at ~ 90 km imply that the peak MF will occur near where $u' = (c-u)$ and will decrease as the critical level is approached. The resulting upper bound MF estimates at 83, 84, and 87 km are summarized in Table 5.3. These suggest maximum MFs ranging from $\sim 96 \text{ m}^2\text{s}^{-2}$ at 83 km to less than $\sim 10 \text{ m}^2\text{s}^{-2}$ at 87 km. The calculations given by both the methods in Table 5.2 and 5.1 are within these bounds, and the measurements are also consistent with the strong dissipation that must be occurring as the MWs approach the critical level near 90 km.

Given the strong dissipation of this MW up to 85 km, and very weak influences above, it is assumed for further analysis, that the ~ 240 km MW does not have large wind and temperature perturbations affecting the propagation environment of small-scale GWs observed at the altitude of the AMTM. However, it should be acknowledged that this MW most likely has a strong influence on small-scale GW propagation at lower altitudes where its amplitude is large.

Table 5.3: Estimated upper bound MF values for the ~ 240 km MW approximated from 83-87 km

Altitude [km]	$c-u$ [ms ⁻¹]	λ_z [km]	MF limit [m ² s ⁻²]
83	55	15.2	96
84	45	12.4	52
87	25	6.8	9

Small-scale GW characterization and MF calculations

On each segment of the RF22 flight, there were smaller-scale dynamics observed over the South Island. Each of these occurred accompanying the central brighter, and warmer, phase of the ~ 240 km MW, suggesting strong influences of the ~ 240 km MW structure on the character and vertical propagation of these smaller-scale GWs, and potential influences of this ~ 240 km MW on the production of instabilities and secondary GWs. AMTM vertical views of these four events with the large scale ~ 240 km MW background subtracted are shown in Figure 5.2. In each case, the smaller-scale dynamics were aligned principally in the zonal plane and their λ_h varied from ~ 25 -28 km.

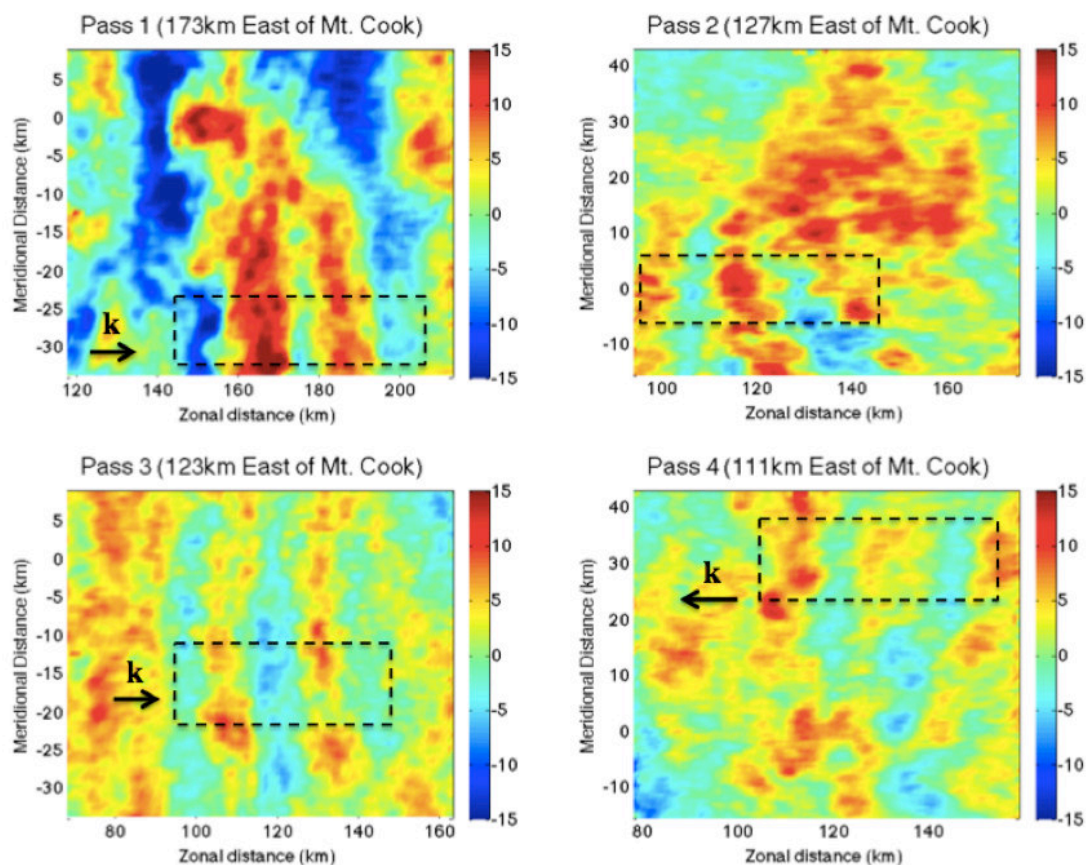


Figure 5.2: Overhead AMTM temperature maps of observed small-scale GWs during the four flight segments over Mt. Cook, NZ on 13 July 2014. The dashed boxes show the areas used for calculating temperature perturbations and wavelength using a Lomb Scargle periodogram. The arrows denote the intrinsic direction of propagation of the observed GWs.

The dotted boxes in Figure 5.2 show the regions of the images used for the calculation of T^o and λ_h . To obtain T^o , the temperature is averaged meridionally as the observed GWs are aligned in the north-south direction. These averages use 10 pixels of the AMTM, so errors due to AMTM noise are significantly reduced. The average differences between the temperature maxima and minima in the boxed areas were used to determine the approximate T^o . In order to calculate a corresponding λ_h , a Lomb Scargle periodogram was used on the images in Figure 5.2.

The smaller-scale GW analysis is limited to the FOV of the AMTM. The images in Figure 5.2 are ~45 km meridionally by ~90 km zonally, and the smaller-scale GWs analyzed in this section have a $\lambda_h < 45$ km. The phase speed c for each observation was calculated by tracing phase movement across successive images in time and compensating for the speed of the GV. From these observed phase speeds, the intrinsic phase speed, $c_i = c - u$, for each event was calculated using the mean horizontal wind, u , estimated from the radar measurements. In order to account for expected uncertainties in the local mean wind, we also calculate the MF assuming that u is larger and smaller by 15 ms^{-1} . This allows for estimates of the possible range of MF s given the inherent uncertainties in the available horizontal wind information. Given the differing nature of the small-scale dynamics, each pass is described separately below.

Pass 1

This GW was observed to be propagating with a phase speed of $\sim 100 \text{ ms}^{-1}$ towards the East. The atmospheric conditions allow for this GW to propagate to higher altitudes, so we assume propagation through the entire OH layer. The measured T^p is ~ 7 K, the horizontal wavelength is 28 km, and for a background wind of -25 ms^{-1} at 87 km, the corresponding MF is $\sim 105 \text{ m}^2\text{s}^{-2}$ which is ~ 10 - 20 times the mean at this altitude. The MF for zonal winds of $\pm 15 \text{ ms}^{-1}$ about the mean wind assumed above also yielded vertical propagation in each case, with MF ranging from ~ 70 - $200 \text{ m}^2\text{s}^{-2}$.

Pass 2

This feature appears to be largely confined to the FOV of the GV AMTM and is not seen in the side viewing cameras, it evolves somewhat in shape over the interval observed, and the relative

motion ($\sim -24 \text{ ms}^{-1}$) appears to be the same as the mean wind ($\sim -25 \text{ ms}^{-1}$). Thus, we believe these features to be instabilities that simply advect with the mean wind at this altitude.

Pass 3

Similar to the first pass, this GW is propagating with an observed phase speed of 130 ms^{-1} to the East. At the central OH altitude of $\sim 87 \text{ km}$, the measured phase speed implies that the observed GW is evanescent. However, given the significant $T^{\circ} \sim 5 \text{ K}$, it is likely that this GW is ducted at a nearby eastward wind or N^2 maximum at a lower altitude, given the wind profile implied by the meteor radar and the N^2 maximum implied by SABER from $\sim 82\text{-}85 \text{ km}$. The stronger eastward winds measured by the meteor radar just a few km below 87 km would allow this GW to be in a region of vertical propagation below the evanescent region near 87 km .

Pass 4

The GW in this case has an observed phase speed near zero, suggesting a smaller-scale MW that is also approaching a critical level. It also appears to have small-scale structure, suggesting it may be exhibiting instability accompanying its decreasing vertical wavelength and amplitude. For this reason, 84 km is used as the analysis altitude, similar to that of the $\sim 240 \text{ km}$ MW. The measured $T^{\circ} \sim 4.4 \text{ K}$ and horizontal wavelength of $\sim 25 \text{ km}$ implies a $MF \sim 21 \text{ m}^2 \text{ s}^{-2}$, with lower limits varying from $13\text{-}33 \text{ m}^2 \text{ s}^{-2}$ due to an estimated uncertainty in the background wind of $\pm 15 \text{ ms}^{-1}$. While it was assumed this is a MW because of the \sim zero phase speed and the small-scale structure at higher altitudes, the complex environment through which this GW must propagate to reach the MLT region should be noted. This GW was observed above a region of low stability and decreasing temperature as measured by both SABER and the Lauder lidar. This region is likely a layer in which MWs are breaking, and the observed GW from this pass could either be a MW contributing to the breaking dynamics and retaining a coherent structure but with smaller

amplitude as observed in modeling of GW breaking [Fritts *et al.*, 2009], or this could be a secondary GW coincidentally having the same phase speed as the source MWs.

The characteristics of each observation are summarized in Table 5.4. The MF calculations for passes 1 and 4 are summarized in Table 5.5. The MF estimates for pass 1 and 4 are very conservative as the T' is not corrected for averaging over the OH layer, which would yield a larger implied T' in all cases. As noted previously, the MW breaking environment at the bottom side of the OH layer adds complexity that makes confident estimates of the true T' challenging. These MF estimates were also performed for u increased and decreased by 15 ms^{-1} relative to the estimated u in each case. The MF values computed for changes in u (and c_i) by 15 ms^{-1} approximate the extrema of the possible MF values, given the uncertainties of the local horizontal wind u and phase speed c determinations from the AMTM.

Table 5.4: Small-scale parameters for passes 1-4 on the 13 July 2014 obtained from Figure 7

Pass #	$\langle T' \rangle$ [K]	c [ms^{-1}]	u [ms^{-1}]	c_i [ms^{-1}]	λ_h [km]	m^2 [m^{-2}]	λ_z [km]
1	7	-100	-25	-75	28	3.88E-08	31.9
2	6	-24	-25	--	28	--	--
3	5	-135	-25	-110	28	-1.23E-08	--
4	4.4	0	-45	45	25	1.96E-07	14.2

Table 5.5: Small-scale GW MF calculated without correcting for integration over the OH layer for passes 1 and 4 during the 13 July 2014 flight

Pass #	Altitude [km]	MF [m^2s^{-2}]		
		$u-15$ [ms^{-1}]	u [ms^{-1}]	$u+15$ [ms^{-1}]
1	87	68	105	212
4	84	33	21	13

Overview 13 July 2014 Momentum Flux

The *MFs* listed in Tables 5.1, 5.2 and 5.5 span a wide range of magnitudes for various observed GW scales and amplitudes. The ~ 240 km MW was estimated to have *MFs* ranging from 3 to 6 m^2s^{-2} at ~ 87 km by the AMTM, and potentially *MFs* as large as 68 m^2s^{-2} from the sodium mixing ratio displacement estimates at a lower altitude where the MW amplitude is obviously much larger. This larger value is ~ 10 times larger than mean values at this altitude, and this *MF* spans a region extending hundreds of kilometers zonally and meridionally. In comparison, the smaller-scale GWs observed in localized regions over South Island on flight segments 1 and 4 had large *MFs* with conservative estimates for pass 4 of $\sim 20 \text{ m}^2\text{s}^{-2}$, and conservative estimates for pass 1 of $\sim 100 \text{ m}^2\text{s}^{-2}$. Regardless of errors associated with these estimates, they may greatly underestimate the actual *MF* values depending on phase averaging of the small-scale GWs over the OH layer. Compared to the ~ 240 km MW, the smaller-scale GWs that were propagating had much larger *MFs*, and these range from as much as ~ 2 - 20 times typical mean magnitudes of ~ 5 - $10 \text{ m}^2\text{s}^{-2}$ expected at these altitudes. While we note that these calculations may have large errors associated with them, even very conservative estimates show that the *MF* associated with the small-scale GWs are significant. These estimates demonstrate the potentially important role of such small-scale GWs in the overall momentum budget of the mesosphere and lower thermosphere.

5.2 Momentum Transport Due to Small-Scale Mountain Waves

This section discusses several instances of small-scale MWs observed during the DEEPWAVE campaign over the South Island of New Zealand. These data were taken during times when the sodium lidar measured at two frequencies, so temperatures are available in addition to sodium mixing ratios and densities.

29 June 2014

On 29 July 2014 there was strong MW forcing due to winds over the South Island of New Zealand. Ground speed winds were measured to be between 8-16 ms^{-1} . Significant GW activity was observed in the flight level data. Few MWs were observed at MLT altitudes during this strong forcing event, likely given the atmospheric conditions and the large amplitudes of the generated MWs. One pass showed what appeared to be several periods of a GW followed by overturning of that same GW seen in the sodium density and mixing ratios shown in Figures 5.3 and 5.4. These GWs were further seen in the sodium lidar temperature measurements which are shown in Figure 5.5. These temperatures do not have the same resolution as the densities, and there is more associated noise with the temperature estimate, so they do not resolve the smaller scale features. However, the temperatures do show two phases of the GW west of where the overturning occurs. Densities were averaged for ~ 75 s and 0.6 km and temperatures were averaged for ~ 75 s and 1.8 km.

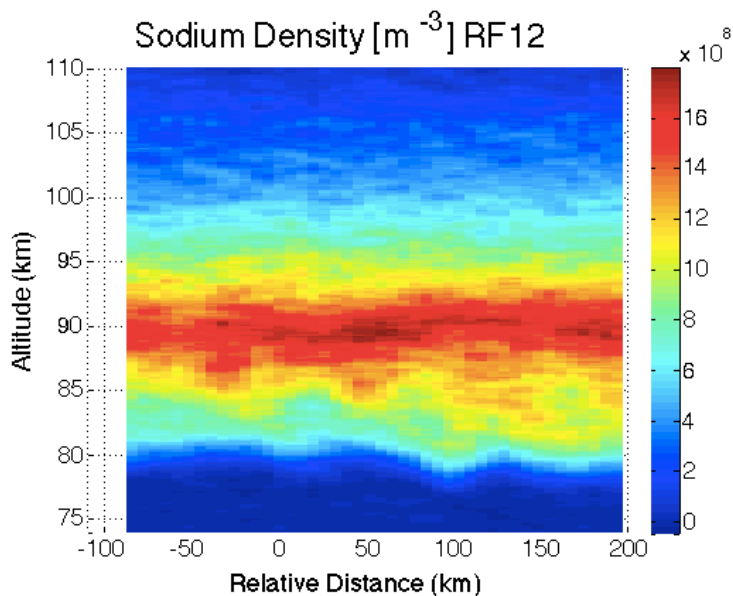


Figure 5.3: Sodium densities measured during the flight on 29 June 2014 between 15:16 UT and 15:37 UT.

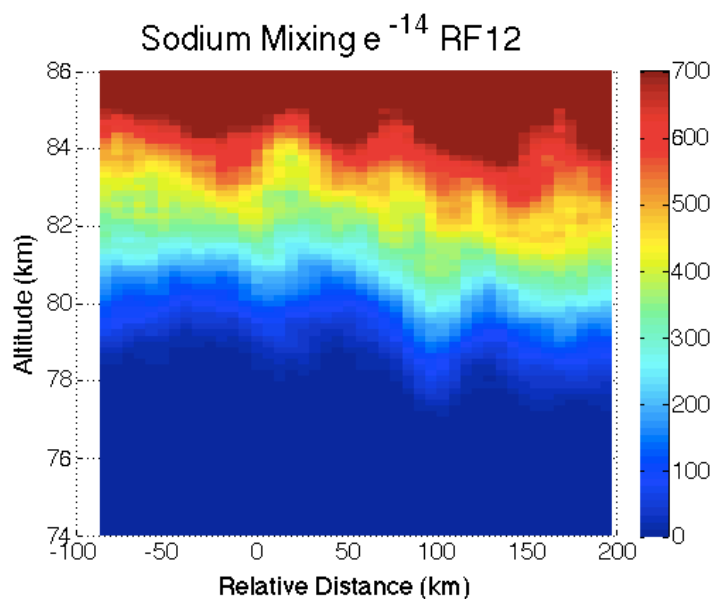


Figure 5.4: Sodium mixing ratios measured during the flight on 29 June 2014 between 15:16 UT and 15:37 UT

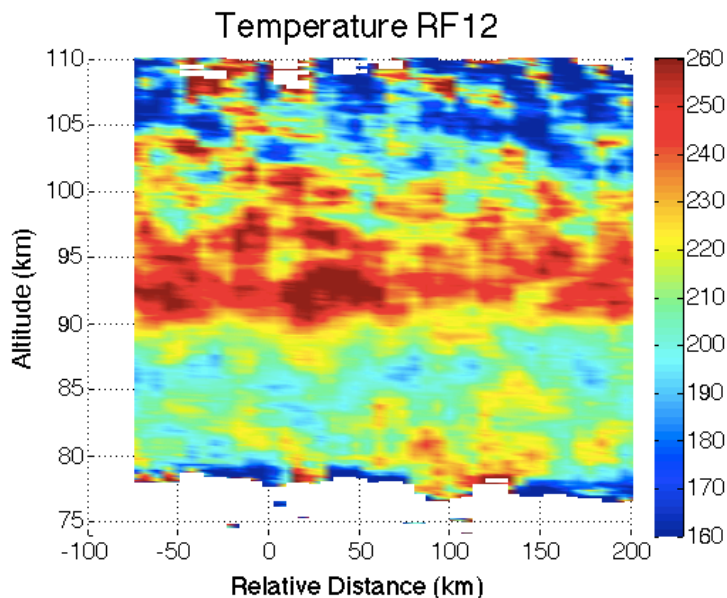


Figure 5.5: Sodium lidar temperatures measured during the flight on 29 June 2014 between 15:16 UT and 15:37 UT

The temperatures show a GW with an apparent vertical wavelength of ~ 12 km and a horizontal wavelength of ~ 70 km that appears to be undergoing dissipation. This GW is observed up to 90 km but is no longer visible in the warm layer between 90-95 km. The amplitude T' is ~ 10 K. A smoothed plot of the N^2 environment is shown in Figure 5.6. The N^2 values between ± 50 km of Mt. Cook and between 85 and 90 km indicate a very stable atmosphere with N values ranging from ~ 0.02 to 0.0265 s^{-1} with the mean being 0.0217 s^{-1} . These N^2 values were calculated using smoothed temperatures (100 km spatially and 6 km vertically) and differencing range bins for dT/dz of 900 meters.

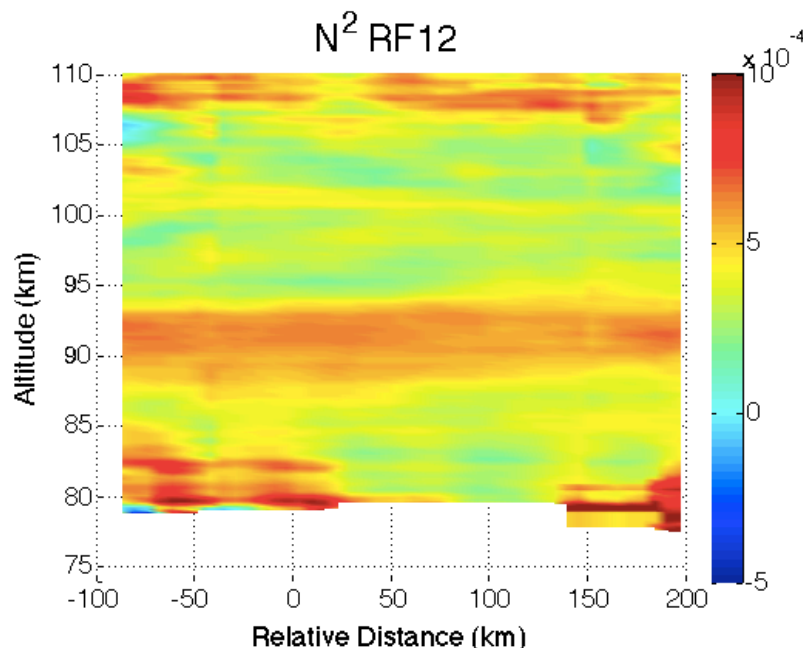


Figure 5.6: N^2 values calculated from smoothed temperatures for the flight on 29 June 2014 between 15:16 UT and 15:37 UT

The AMTM displays some evidence of GWs during this time in both the temperature map and OH imagers. These are shown in Figures 5.7 and 5.8. Lidar data are not available for the entire southern pass, so the following analysis will be done for the northern pass, and these lidar data were previously shown in Figures 5.3-5.5. Figures 5.7 and 5.8 show evidence of a GW with phase fronts aligned 30-45° NE. The clearest view of this GW was on the southern pass, which showed the phase fronts to be stationary, indicating this observed GW to be a MW. Two additional OH images are shown Figure 5.9, where the side viewing OH cameras show further indications of this MW, which persisted for less than one hour.

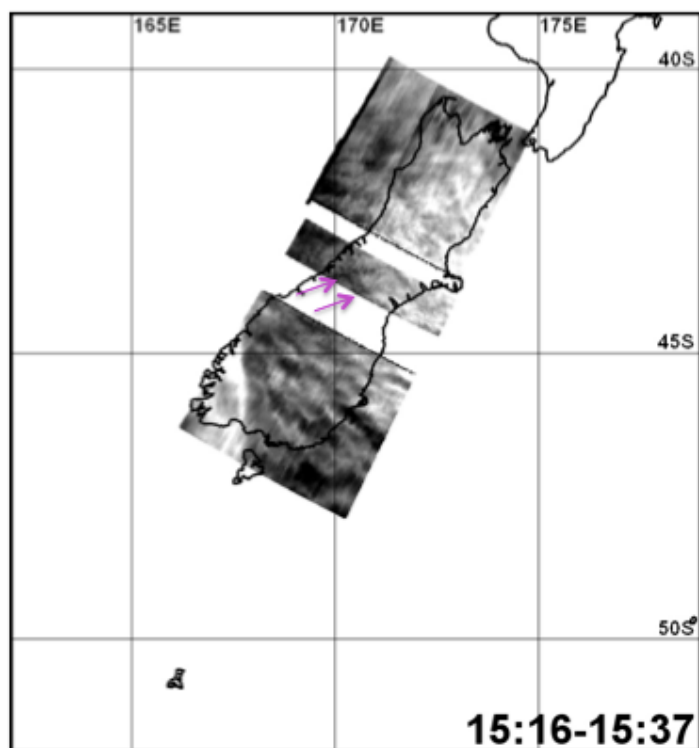


Figure 5.7: OH imager views corresponding to the lidar data from the 29 June flight. The blue arrows point out the two phases of the MW.

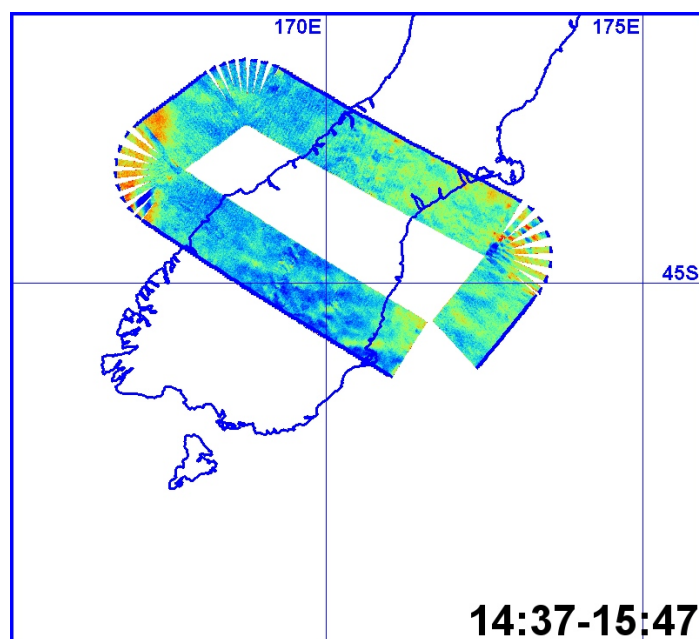


Figure 5.8: AMTM keogram corresponding to the lidar data from the 29 June flight. The northern portion corresponds to the data shown in Figures 5.3-5.7.

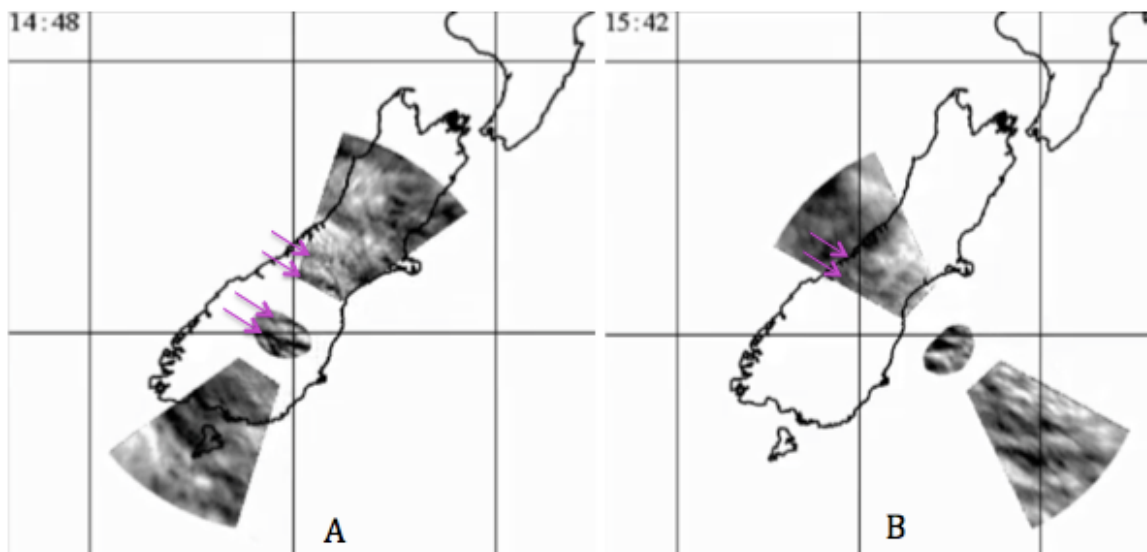


Figure 5.9: OH images from the 29 June 2014 flight. Figure A shows the MW observation on the southern pass, which is apparent in the overhead camera and in the north viewing OH camera. Figure B shows the MW observation in the west viewing camera over the region of the north flight track. A and B show the beginning and end of the MW, which persisted for ~1hr.

Figure 5.9a shows the MW towards the beginning of the observation period, and Figure 5.9b shows the MW towards the end of the observation period. Figure 5.7 also shows evidence of the MW in the overhead OH layer, although this is faint. As noted above, the AMTM averages over a significant altitude range, and shallower vertical wavelengths cause more difficulty for AMTM detection. For this particular case, the observed vertical wavelength in the lidar data was ~13 km, which would result in strong cancellation throughout the OH layer. Furthermore, the shape of the OH layer will also strongly contribute to the observed signal. On this evening, the SABER satellite passed over this region near 11 UT (~5 hours before the event). Profiles from two consecutive passes at 45.7S, 167.8E and 44.4S, 170.6E are shown in Figure 5.10. These two passes show strong variability in the OH layer just a few hundred kilometers apart. At one

location, the OH layer is observed to have two peaks at 85 km and 80 km, with a FWHM of ~11 km. At the nearby location the OH layer is observed to have a peak near 85 km with a FWHM of ~7 km. These fluctuations in the OH layer that can contribute to a wider vertical averaging combined with the shorter vertical wavelength of the MW observed in the lidar data may explain the contrast between the weaker MW signal observed in the OH layer versus the large ~20K peak-to-peak temperature differences measured by the lidar. Additionally, the breaking structure of the observed MW in the lidar, and the lack of coherent structure may also explain the difference between the AMTM and the lidar measurements.

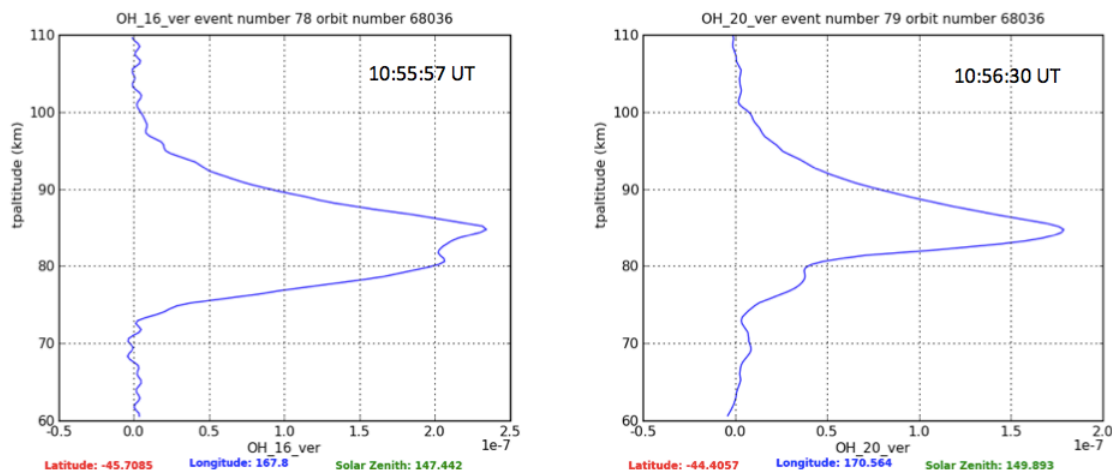


Figure 5.10: SABER data on 29 June 2014 showing the variability of the OH layer over a short distance of 1.3° latitude and 2.8° longitude. At 10:55:57, the OH layer appears to have a double peak at 85 and 80 km with a FWHM of ~11 km. At 10:56:30, the OH layer appears to be centered near 85 km with a FWHM ~7 km.

Using equation 2.16, the MF of the observed MW was calculated using parameters calculated from the lidar. The resulting MF from this calculation is $\sim 34 \text{ m}^2\text{s}^{-2}$. An overview of the parameters used to calculate the momentum flux is given in Table 5.6.

Table 5.6: Parameters for observed GW on 29 June 2014 and corresponding MF calculation

λ_x [m]	λ_z [m]	N [s^{-1}]	T' [K]	MF [m^2s^{-2}]
70	12	0.0217	10	34

The calculated MF for this particular GW is above the mean for this altitude. In this case, the observation of the MW did not persist throughout the entire research flight, which took place during a strong forcing event.

28 June 2014

The 28 June flight, or RF11, was flown starting over the South Island, then went far out over the ocean, and ended with another pass over the South Island. This was a much lower forcing day than the 29 June event. GWs were observed during the portions of this flight that took place over the island. This section focuses on the last portion of the flight where an overturning GW event was observed in the sodium lidar data. There were several phases of this GW observed before the overturning region. This GW was also observed by the overhead OH imager with an apparent near zero phase speed, implying the GW is likely a MW. For this reason, it will be referred to as such. A plot of the sodium densities showing the observed MW is given in Figure 5.11. Similarly, the sodium mixing ratios for the bottom side of the layer are shown in Figure 5.12 next to the sodium densities for the bottom side of the layer, which also clearly show the wave overturning near the eastern edge of the flight.

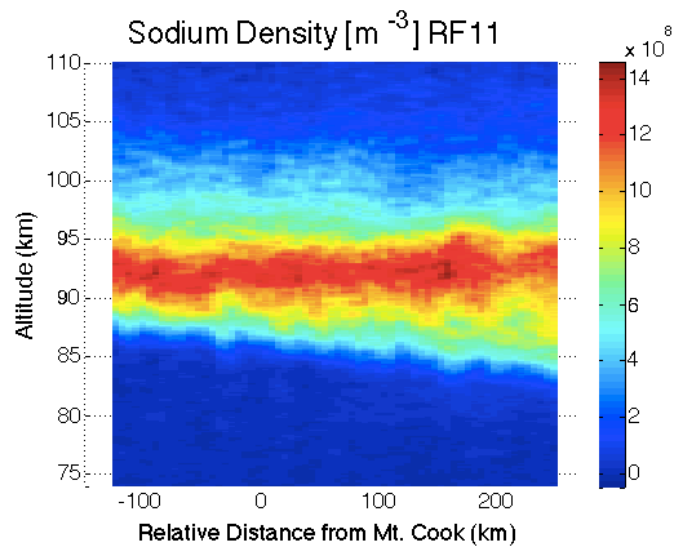


Figure 5.11: Sodium densities from 28 June 2014 from 11:09-11:35 UT

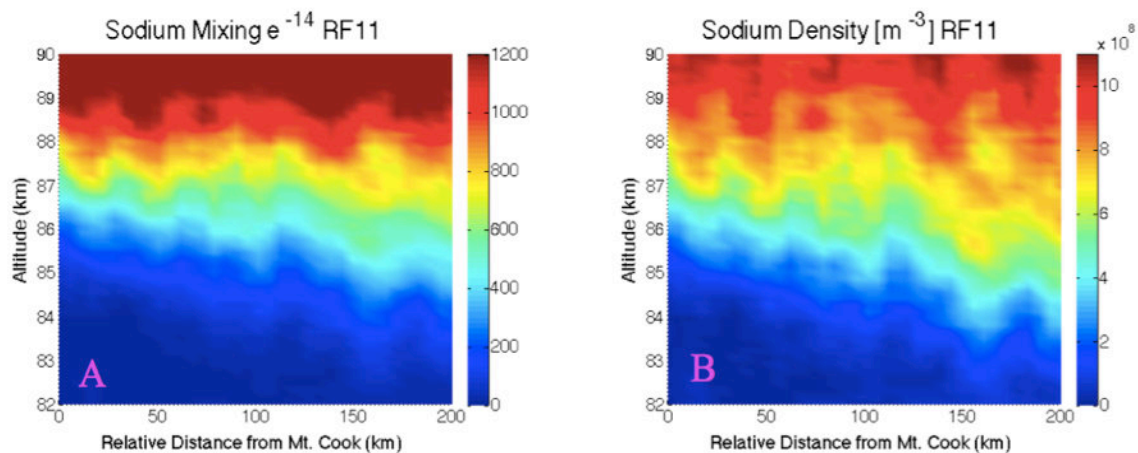


Figure 5.12: The Plot A shows the sodium mixing ratios for the bottom side of the layer on 28 June 2014. Plot B shows the sodium densities for the bottom side of the layer. Near the Eastern end of the flight GW overturning is apparent.

Four successive OH overhead and side-viewing images are shown in Figure 5.13. As previously noted, the MWs observed in the overhead camera appeared to have a near zero phase speed. GWs of a similar scale were also observed in the north viewing camera, but these appeared to have a slightly NW phase movement, so they may not be the same GW field observed overhead.

The overhead MWs appeared near the western edge of the island and disappeared at the eastern edge.

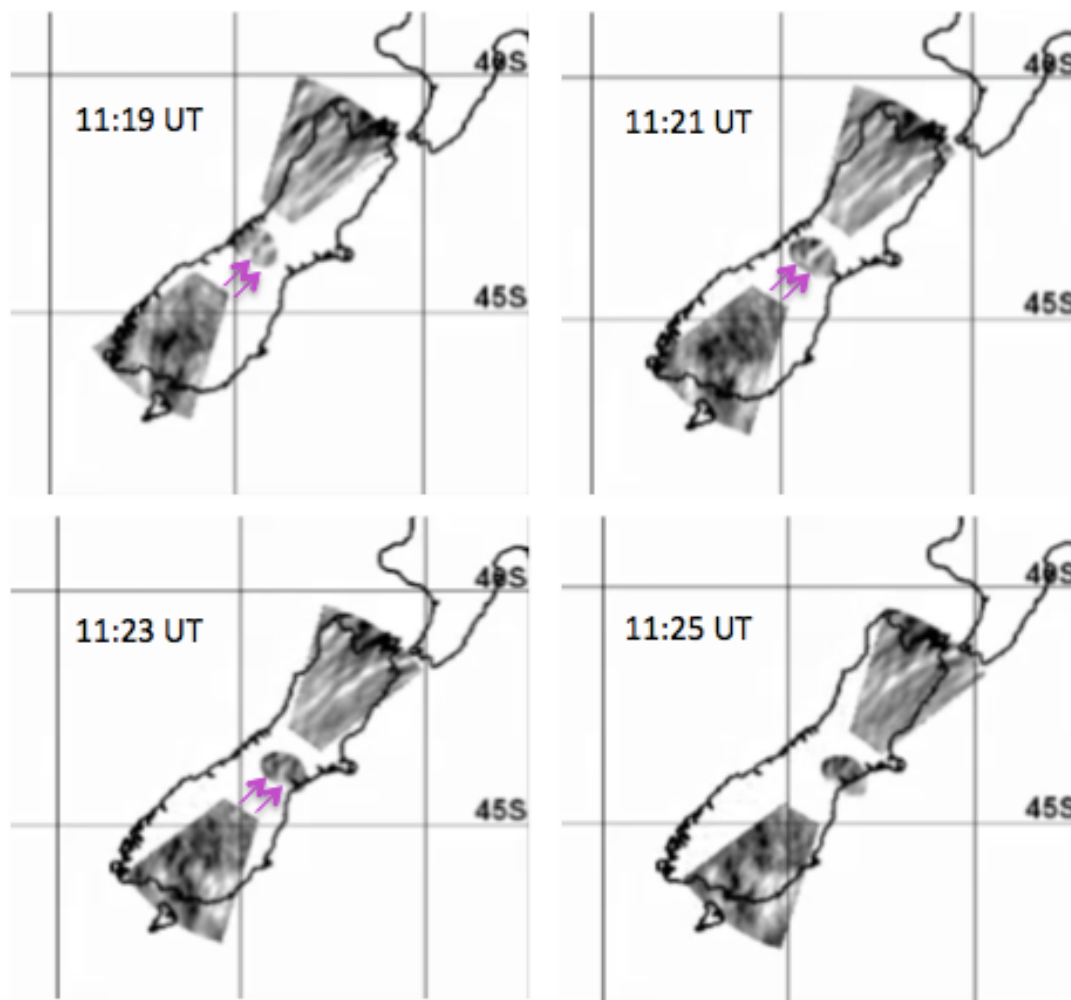


Figure 5.13: Overhead OH camera images from 28 June 2014 show the MW appears at the western edge of the island and is spatially visible until the eastern edge.

Temperatures were also available from the sodium lidar for this flight and are shown in Figure 5.14. The temperatures clearly show the MW, especially on the bottom side of the layer. The wave structure disappears towards the end of the flight path in the same location that the GW

overturning is observed in the sodium densities. In the coherent portion of the GW, the temperature perturbation is observed to be ~ 11 K. The horizontal wavelength is ~ 50 km and the vertical wavelength is ~ 20 km.

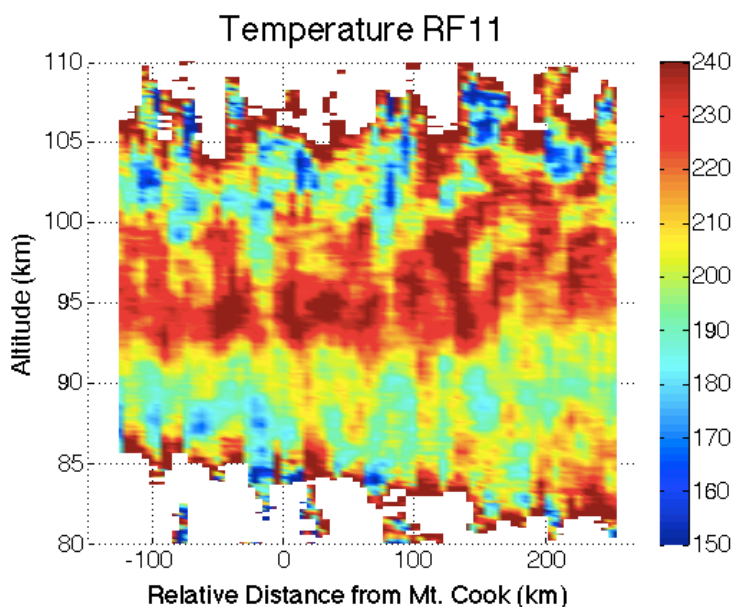


Figure 5.14: Sodium lidar temperatures from 28 June 2014 from 11:09-11:35UT

The background values of N^2 can be calculated using smoothed temperatures. These N^2 values are shown in Figure 5.15 and were calculated using a smoothing of 100 km spatially and 6 km vertically, with a dT/dz differencing of 900 m. The average N value between 86 to 91 km altitude and -50 to 150 km relative distance is ~ 0.0216 s $^{-1}$.

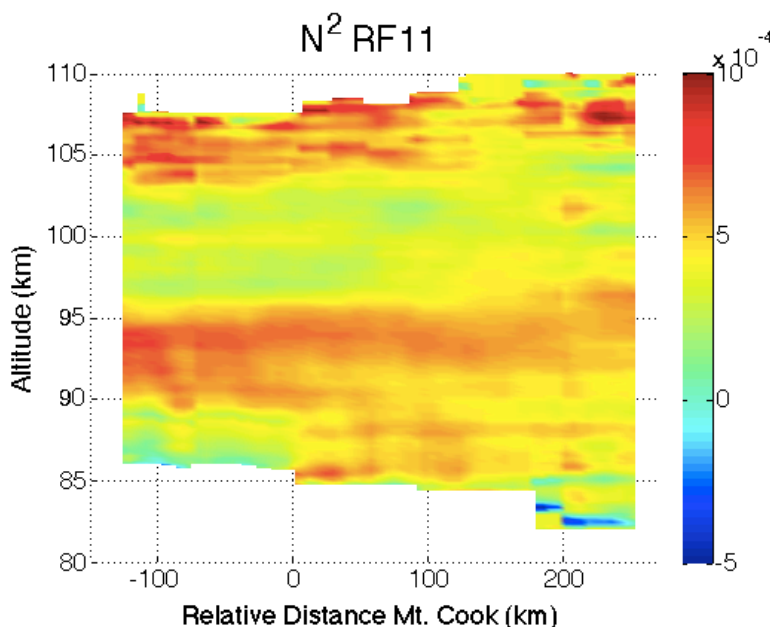


Figure 5.15: N^2 values calculated from smoothed temperatures for the flight on 28 June 2014 from 11:09-11:35UT

Using the above parameters, the MF was calculated using equation 2.23. This MF was found to be $\sim 100 \text{ m}^2\text{s}^{-2}$, which is again large compared to mean values, and is more than twice the value measured on the following day. An overview of the parameters of the observed MW on the 28 June RF11 flight and the corresponding MF are summarized in Table 5.7.

Table 5.7: Parameters for observed GW on 28 June 2014 and corresponding MF calculation

λ_x [m]	λ_z [m]	N [s^{-1}]	T' [K]	MF [m^2s^{-2}]
50	20	0.0216	11	100

5.3 Secondary GW Generation

The research reported in this thesis has demonstrated the importance of small-scale GWs on localized momentum deposition due to GW breaking. A necessary consequence of GW breaking is secondary GW generation. Vadas et al. [2003] have discussed one such mechanism, and this has also been observed [Smith et al., 2013]. While the lidar would likely be unable to detect the larger-scale GWs accompanying breaking through that particular mechanism, it is possible for the lidar to observe smaller-scale GWs generated through other mechanisms associated with breaking. The previous sections of this chapter have discussed the observations of multiple high *MF* GW breaking events. Here, these events are shown in more detail with the observations of multiple types of wave structures above the breaking regions that appear to be secondary GWs.

13 July 2014

As was previously discussed, this research flight observed a 240 km GW that experienced a critical level near 90 km (Figure 5.1 shows the sodium mixing ratio contours for this GW). Near 83 km, the *MF* calculated from the sodium mixing ratio was predicted to be as high as $\sim 70 \text{ m}^2\text{s}^{-2}$. While temperatures were unavailable for this night, high-resolution sodium density measurements were available. Figure 5.16 shows four mixing ratio plots highlighting different altitudes and the visible smaller-scale GWs that develop with increasing altitude.

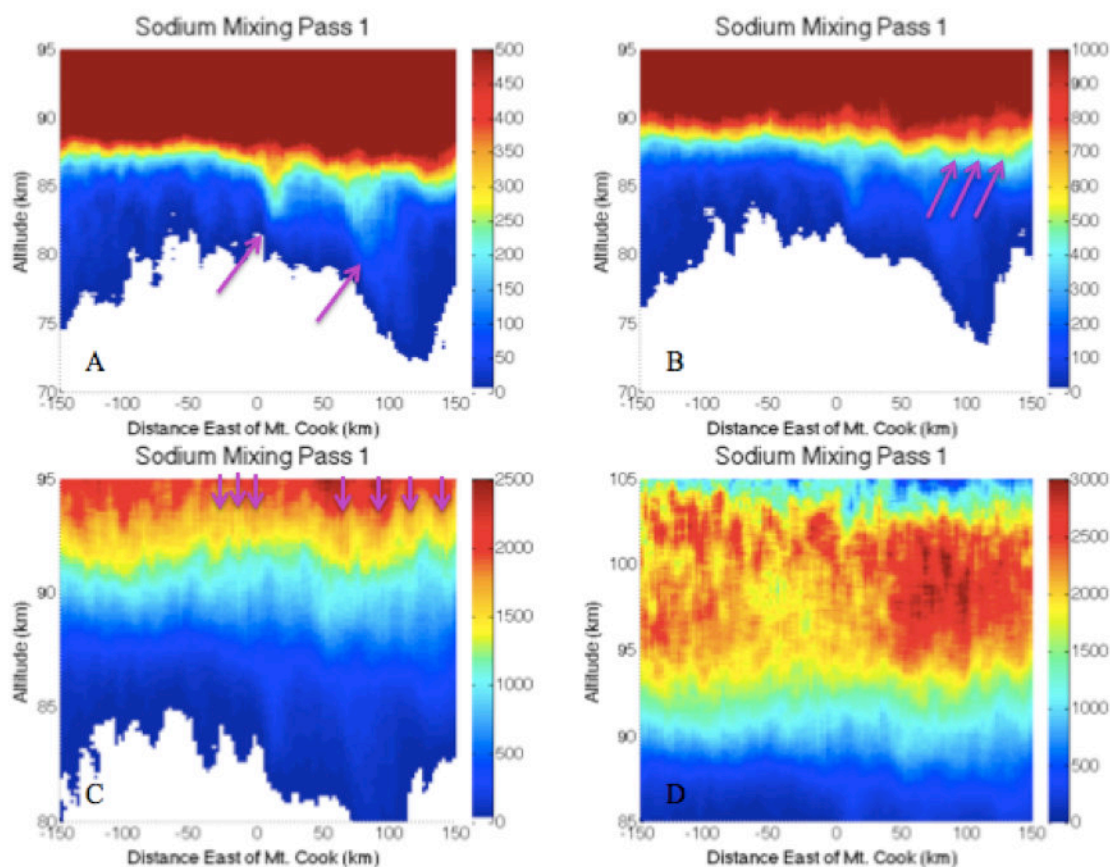


Figure 5.16: Sodium mixing ratios at different altitudes for the first pass of the flight on 13 July 2014. Plot A shows lower altitudes below the critical level where MWs are still present. Plot B shows smaller scale GWs starting to appear near 90 km where a critical level is predicted. Plots C and D show the multiple different scales and phases of smaller scale GWs above the critical level.

At altitudes below 86 km, the larger-scale MWs are clearly seen, but smaller-scale GWs are not present. Figure 5.16b shows small-scale GWs beginning to form near 90 km where there is thought to be a critical level for the stationary MWs. Figures 5.16c and d show multiple small-scale GWs that appear to be propagating in different directions with different wavelengths. The differing phase slants associated with these GWs indicate that they cannot be ducted, but are instead propagating in different directions. These small-scale GWs are also not visible at lower altitudes, further implying local generation. Additionally, it would be difficult for smaller-scale

GWs to propagate through the breaking region of the 240 km GW, which also supports the notion that these observed GWs are secondary GWs.

29 June 2014

The 29 June event observed an overturning GW event with MF of $\sim 34\text{m}^2\text{s}^{-2}$. While these temperatures and densities were shown in Figures 5.5 and 5.3, plots are shown here to highlight some of the observed secondary GW features. Figure 5.17 shows sodium densities and mixing ratios with a 0.6 km vertical resolution. Figure 5.18 shows temperatures with a 1.2 km vertical averaging.

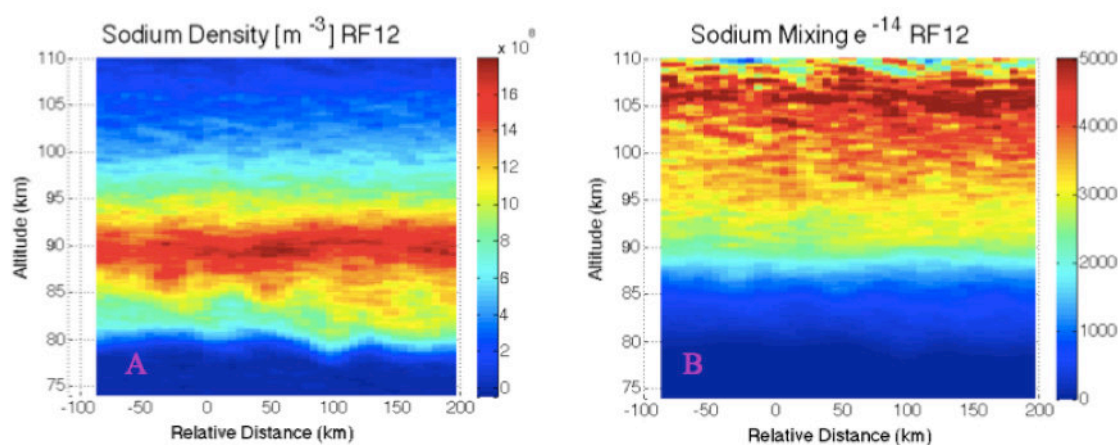


Figure 5.17: Plot A shows sodium densities for 29 June 2014 and Plot B shows the corresponding mixing ratios.

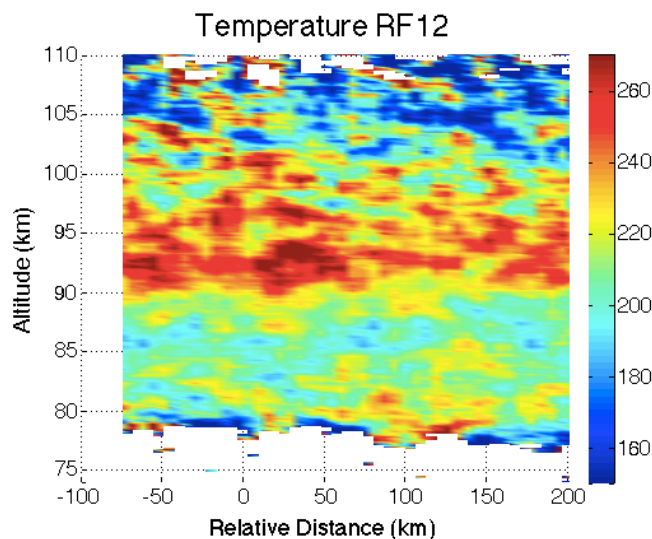


Figure 5.18: Temperatures for 29 June 2014 from 15:16-15:37 UT using 1.2 km vertical averaging

Both the temperatures and densities show interesting layering structures that appear to be associated with this particular event. Figure 5.17 shows very fine, layered structure apparent in both the sodium densities and mixing ratios. The temperatures shown in Figure 5.18 yield further insight into GW activity, and its potential consequences above the observed breaking MW over 90 km. The observed temperatures above 90 km show short vertical wavelength wave structures with significant temperature perturbations. These structures are not readily observable at lower altitudes, suggesting potential secondary GWs and/or the consequences of additional instabilities and turbulent mixing.

28 June 2014

The 28 June flight also observed overturning and GWs with a significant MF of $\sim 100\text{m}^2\text{s}^{-2}$ similar to the 29 June flight. The densities and temperatures for this flight were shown

in Figures 5.11 and 5.14, and are shown again here for reference. Figures 5.19, 5.20, and 5.21 show the sodium densities, mixing ratios, and temperatures.

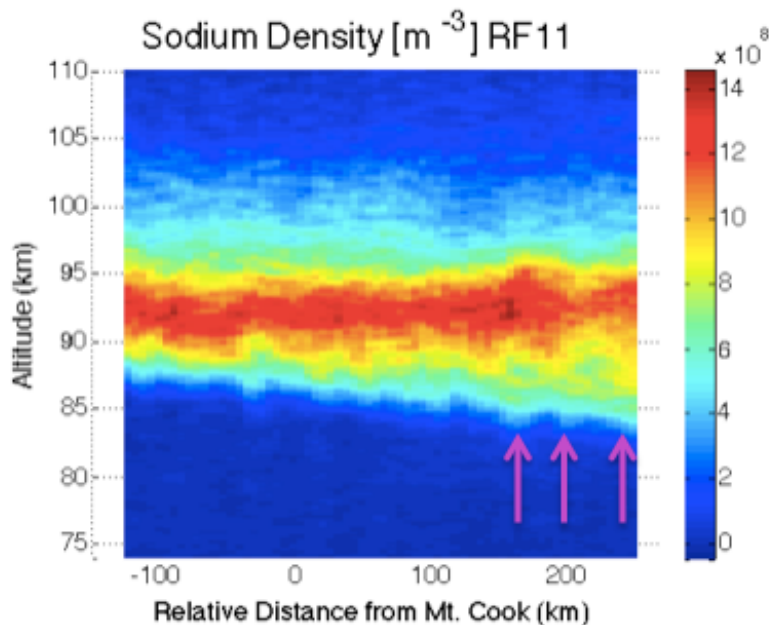


Figure 5.19: Sodium densities on 28 June 2014. The arrows highlight the area of observed GW overturning

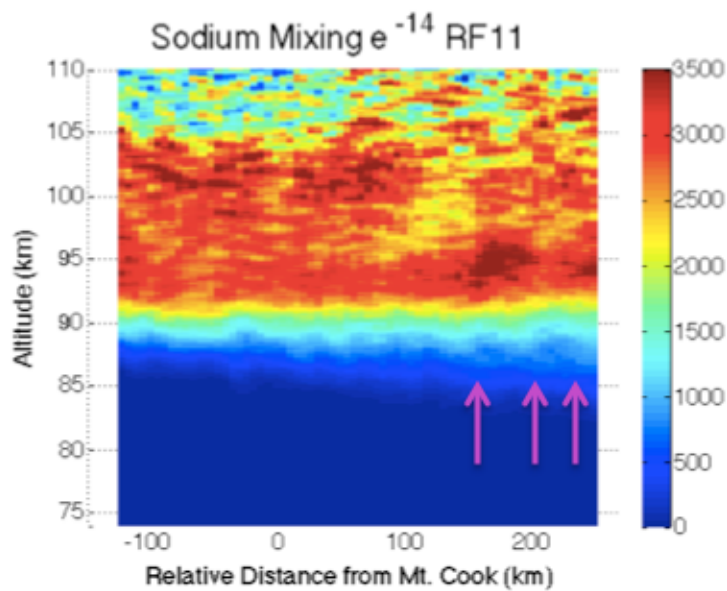


Figure 5.20: Sodium mixing ratios on 28 June 2014. The arrows highlight the area of observed GW overturning

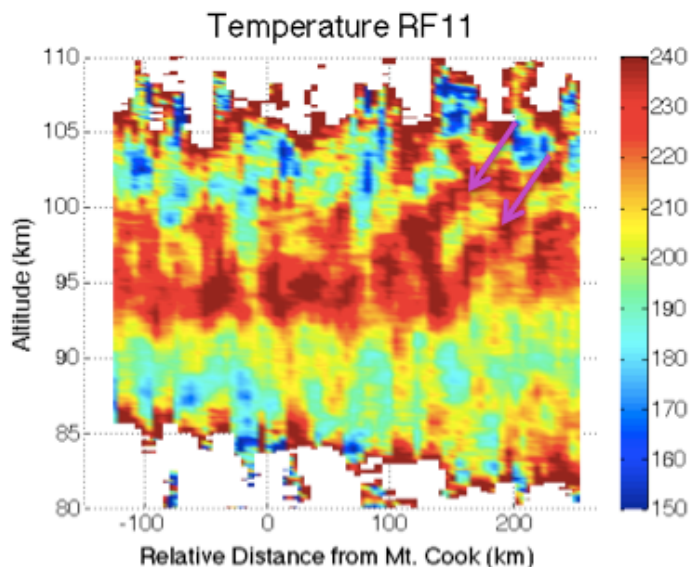


Figure 5.21: Temperatures on 28 June 2014. The arrows highlight the wave structure observed above the region of GW overturning.

The overturning GWs are clearly observed in the sodium densities in Figure 5.19 starting ~150 km East of Mt. Cook. Similar to the 29 June case, the mixing ratios in Figure 5.20 also show the finely layered structures throughout the sodium layer. There are more visible structures in the mixing ratios above the region of GW breaking. While the temperatures in Figure 5.21 do not show the GW overturning as clearly, there is very clear wave structure above the region of breaking. Although this could be due to secondary GW generation, as these GW structures are not visible at lower altitudes, it is also possible that these observed wave structures may have propagated from other sources, and contributed to the GW breaking near 90 km.

Summary of Secondary GW Generation

As previously noted, secondary GW generation is a necessary consequence of GW breaking. While breaking GW MF induces drag on the background atmospheric winds causing notable effects in the MLT, secondary GWs generated from breaking GWs allow for momentum to be transported to higher regions of the atmosphere. Three separate days of observed high MF GW breaking all showed evidence of secondary GWs above the region of breaking. The observed secondary waves were on scales smaller than the original breaking GWs. These observations show that small-scale GWs with significant MF may not only have large effects within the MLT region, but may also have farther reaching effects through the generation of multi-scale secondary GWs.

5.4 Summary of small-scale GW Forcing

The observations discussed above have revealed the strong contributions that small-scale GWs make to the total MF in the MLT. As previously mentioned, ground based instrumentation such as radars have measured mean values ranging from 1-20 m^2s^{-2} and satellite observations have measured values ranging from 1-8 m^2s^{-2} in this region. These measurements of small-scale GWs taken during the DEEPWAVE campaign demonstrate MF values ranging from $\sim 70m^2s^{-2}$ for the larger horizontal GWs to values ranging between 20-100 m^2s^{-2} for GWs with horizontal wavelengths less than 100 km on three different days. Recall also that these measurements were conservative in cases employing the AMTM temperatures because they do not account for phase averaging that may significantly reduce estimated GW amplitudes. These significant values indicate that mean MF due to small-horizontal scale GWs is large, with the potential to contribute disproportionately to localized MF values. Despite these significant MF contributions,

these small-scale GWs are still largely unaccounted for on a global scale in both models and satellite MF estimates. Additionally, measurements also show secondary GW formation above regions of GW breaking, implying additional small-scale GWs that can transport significant momentum to higher altitudes.

6. Conclusions

Research discussed in this thesis has investigated GW propagation and momentum transport in variable environments. Observations were made utilizing data from ALOMAR in northern Norway and the dataset collected during the extensive DEEPWAVE airborne and ground-based field program performed over New Zealand and the surrounding region in June and July 2014. These measurements have enabled new and more comprehensive analyses of small-scale GW events than have been possible elsewhere to date. The research focused on two main areas. The key contributions and conclusions from each component are discussed below.

6.1 Gravity Wave Propagation in Variable Environments

This portion of the research aimed to provide further insight into the following question for several representative measurement sequences:

How are GW propagation and MF affected by variable background environments?

The combination of the AMTM and sodium lidar at ALOMAR allowed for a more comprehensive analysis to characterize the propagation environment for a number of small-scale GWs in the MLT region. The method employed sodium densities and wind and temperature fields to evaluate the predictions of small-scale GW propagation and to distinguish between propagating and evanescent GW behavior over an extended altitude range. The results from measurements on 22-23 January 2012 showed a complex ducting environment accompanying the

observation of GW perturbations throughout the evening in the AMTM data. Complementary sodium densities indicated GW perturbations in regions where favorable propagation was predicted, and that these sodium density perturbations disappeared in regions of unfavorable propagation or evanescence. This study also demonstrated the importance of distinguishing evanescent (or ducted) GWs from propagating GWs in the AMTM data, because ducted GWs may easily be mistaken for vertically propagating GWs based on airglow observations alone, but ducted GWs have little or no vertical MF , whereas propagating GWs at the same scales imply large MF s. The complex nature of background environments can make this task difficult without measurements from a coincident profiling instrument such as a lidar or radar. As demonstrated, the distinction between propagating and evanescent or ducted GWs is not necessarily straightforward, but is critical in quantifying GW forcing of the MLT.

Another example of environmental influences on GW propagation employed data collected at ALOMAR on 27-28 January 2014 during an event where multiple GW scales and periods were observed. For this event, the ALOMAR sodium lidar and SAURA radar defined the background wind and temperature fields with time and the AMTM quantified the small-scale GW characteristics during this observation interval. These results revealed a very strong influence of larger-scale GWs on the vertical propagation of a small-scale GW having a 10-min period and a large MF . These results highlight the important role that larger-scale GWs play in modulating the propagation environment of small-scale GWs.

Measurements from the DEEPWAVE campaign provided additional insights into the vertical propagation and temporal variability of small-scale GWs in the presence of larger-scale GWs and mean winds. Successive GV flights enabled the observation of small-scale GW behavior within the evolving larger-scale environment over periods of several hours.

Specifically, several observations of MWs approaching a critical level identified by the Kingston meteor radar winds revealed multiple varied responses accompanying GW superpositions and instabilities driven by large amplitudes and critical level approach.

Key findings of this section are summarized below:

- The AMTM and sodium lidar combination provide a new technique to map the propagation environment for a given spectrum of observed small-scale <100 km GWs. This method gives a temporal and vertical map of where a given observed GW may be ducted or propagating.
- Sodium densities provide an effective tracer for small horizontal-scale GW propagation within the MLT that would otherwise be undetectable by the temperature resolution of the sodium lidar. In the case study from 22-23 January 2012, sodium density perturbations showed small-scale GW propagation to match regions of predicted favorable propagation inferred from the lidar winds and temperatures in altitude.
- Complex ducting environments sustain ducted GWs for extended periods of time. These GWs may appear to be propagating at the altitude of the AMTM, but should not be included in *MF* calculations.
- Larger-scale dynamics appear to have influences on smaller-scale GW propagation and the local small-scale GW propagation environment. Additionally, some observations show that smaller-scale GWs appear to exhibit enhanced propagation and amplitudes within a specific phase of larger-scale GWs.
- Decreasing winds in the MLT cause critical levels for MWs that have been able to propagate to these altitudes under suitable environmental conditions. This has strong

influences on the local dynamics as the amplitudes, and corresponding MF s of MWs that reach this region are significant.

6.2 Gravity Wave Momentum Flux Contributions

The research regarding GW MF aimed to investigate the following question:

What contributions do smaller-scale GWs (horizontal scales < 100 km) make to the momentum budget of the MLT?

Several observations from the DEEPWAVE campaign showed GWs with significant associated MF s. On 13 July 2014, multiple scales of both MWs and propagating GWs were observed. While previously measured mean values of MF in the MLT range from ~ 1 - $20 \text{ m}^2\text{s}^{-2}$, MF values measured on this night ranged from 17 - $68 \text{ m}^2\text{s}^{-2}$ for the ~ 240 km MW, and from ~ 20 - $100 \text{ m}^2\text{s}^{-2}$ for the GWs with horizontal wavelengths < 30 km. These values are either on the higher end of mean values or several times the mean MF s previously measured within the MLT.

MWs observed on other flights on the 28th and 29th of June also had significant MF contributions as estimated from the lidar temperature measurements. The values for these two flights were $\sim 100 \text{ m}^2\text{s}^{-2}$ and $\sim 34 \text{ m}^2\text{s}^{-2}$, which are also higher than mean MF values previously measured for this region.

The observations of these MWs occurred during passes where the MW was overturning or expected to be breaking given a background critical level. Above these regions of overturning and breaking, signatures in both the densities and temperatures revealed the presence of smaller-

scale wave features likely to be secondary GWs generated by the breaking MWs. This indicates that MWs play complex roles in transporting momentum throughout the atmosphere.

All of the observations summarized above show the potential for small-scale GWs to have distinct and significant localized *MF*s. These large *MF*s are important to the global momentum budget assuming these observations are happening over a broad range of locations, and the findings are essential given that global scale models do not generally account for or resolve these smaller-scale GWs. The measurements quantify a largely unaccounted for contribution of *MF* in the MLT.

Key findings of this section are listed below:

- Small horizontal-scale GWs contribute uniquely and disproportionately to localized *MF*, demonstrating their importance in the global momentum budget.
- *MF* measurements from small-scale GWs quantify *MF* that is largely unaccounted for in global scale models.
- Overturning and breaking MWs that reach the MLT have significant *MF* contributions.
- Smaller-scale secondary GWs appear above regions of observed MW breaking.

6.3 Overview and Future Work

The findings of this dissertation bring up new questions that may be answered with future research. Measurements of small-scale GW *MF*s indicate that these GWs make significant contributions to the global momentum budget. Yet, these smaller-scale GWs are largely unaccounted for in global-scale models.

The observed critical levels in the MLT during various breaking events provide insight into breaking conditions leading to momentum deposition in the MLT region. While the theory of GW breaking due to critical levels is understood, the observations of this kind are new. These observations lead to a more quantitative potential for predictive capabilities with modeling, and the connection between MW generation, propagation into the MLT, and critical levels leading to breaking that causes acceleration on local winds due to momentum deposition.

In addition to these environmental conditions that lead to GW breaking, the observations of secondary GWs above breaking regions are a key target for further research. The mechanism under which these smaller-scale secondary GWs form is of interest, and more modeling and research is needed on this topic. These observations also raise further questions about the nature of secondary GWs generated by primary GW breaking, and the transport of momentum by these secondary GWs. More research is needed to understand the different scales of secondary GWs generated, and how far these GWs propagate before breaking and creating further secondary GWs.

The research described in this dissertation also provided measurements and analysis regarding multi-scale GW interactions and dynamics. Several events observed small-scale GWs within the warmer phase of a larger scale GW, indicating that there are strong influences of these larger-scale dynamics on small-scale GWs. The event on 27-28 January 2014 showed that a ~10-minute period GW appeared to correlate with a phase of a background 1-hr period GW. The propagation environment for this 10-minute period GW mapped using the radar also showed that the 1-hr period GW strongly modulated the m^2 that this short 10-minute period GW would experience propagating through this multi-scale environment at different times of the evening. Similarly, during the 13 July flight of the DEEPWAVE campaign, many smaller-scale GWs

were observed in the warm phase of the 240 km MW, indicating that the larger-scale GW has influences on the propagation of smaller-scale GWs. These dynamics are poorly understood currently, and represent another target for additional research.

The measurements and analyses presented here have yielded a better understanding of multi-scale interactions, and suggest that more studies are needed to appreciate the impact of these multi-scale environments on the intrinsic parameters and influences of small-scale GWs, especially their vertical propagation, dissipation, and momentum deposition. This research has provided new contributions as well as produced new questions and research problems.

References

- Alexander, M. J. and T. J. Dunkerton, (1999), A Spectral Parameterization of Mean-Flow Forcing due to Breaking Gravity Waves, *J. of The Atmos. Sci.*, 56, 4167-4182.
- Alexander, MJ, M. Geller, C. McLandress, S. Polavarapu, P. Preusse, F. Sassi, K. Sato, S. Eckermann, M. Ern, A. Hertzog, Y-A Kawatani, M. Pulido, T. Shaw, M. Sigmond, R. Vincent, S. Watanabe, (2010), Recent developments in gravity-wave effects in climate models and the global distribution of gravity-wave momentum flux from observations and models. *Q. J. R. Meteorol. Soc.*, 136, 1103-1124. DOI:10.1002/qj.637.
- Alexander, M. J., J. Gille, C. Cavanaugh, M. Coffey, C. Craig, T. Eden, G. Francis, C. Halvorson, J. Hannigan, R. Khosravi, D. Kinnison, H. Lee, S. Massie, B. Nardi, J. Barnett, C. Hepplewhite, A. Lambert, and V. Dean, (2008), Global estimates of gravity wave momentum flux from High Resolution Dynamics Limb Sounder observations, *J. Geophys. Res.*, 113, D15S18, doi:10.1029/2007/JD008807.
- Alexander, M. J., and C. Barnet, (2007), Using Satellite Observations to Constrain Parameterizations of Gravity Wave Effects for Global Models, *J. Atmos. Sci.*, 64, 1652-1664.
- Beres, J. H., M. J. Alexander, and J. R. Holton (2002), Effects of Tropospheric Wind Shear on the Spectrum of Convectively Generated Gravity Waves, *J. Atmos. Sci.*, 59, 1805-1824.
- Bossert, K., D. C. Fritts, P.-D. Pautet, M. J. Taylor, B. P. Williams, and W. R. Pendelton (2014), Investigation of a mesospheric gravity wave ducting event using coordinated sodium lidar and Mesospheric Temperature Mapper measurements at ALOMAR, Norway (69°N), *J. Geophys. Res. Atmos.*, 119, 9765–9778, doi:10.1002/2014JD021460.
- Bossert, K., D. C. Fritts, P.-D. Pautet, B. P. Williams, M. J. Taylor, B. Kaifler, A. Dörnbrack, I. M. Reid, D. J. Murphy, A. J. Spargo, and A. D. MacKinnon, (2015), Momentum Flux

Estimates Accompanying Multi-Scale Gravity Waves over Mt. Cook, New Zealand on 13 July 2014 during the DEEPWAVE Campaign, *J. Geophys. Res.*, doi: 10.1002/2015JD023197.

Cai, X., T. Yuan, Y. Zhao, P.-D. Pautet, M. J. Taylor, and W. R. Pendelton Jr, (2014), A coordinated investigation of the gravity wave breaking and the associated dynamical instability by Na lidar and Advanced Mesospheric Temperature Mapper over Logan, UT (41.7 N, 111.8 W), *J. Geophys. Res. Space Physics*, 119, 6852-6864, doi:10.1002/2014JA020131.

Chimonas, G. and C. Hines (1986), Doppler Ducting of Atmospheric Gravity Waves, *J. Geophys. Res.*, 91, D1, 1219-1230.

Chimonas, G. and J. R. Grant (1984), Shear Excitation of Gravity Waves. Part II: Upscale Scattering from Kelvin-Helmholtz Waves, *J. Atmos. Sci.* 41, 15, 2278-2288.

Chiu, Y. T., and B. K. Ching, 1978: The Response of Atmospheric and Lower Ionospheric Layer Structures to Gravity Waves, *Geophys. Res. Lett.*, 5, 6, 539-542.

Clark, T. L., Hauf, T. and Kuettner, J. P. (1986), Convectively forced internal gravity waves: Results from two-dimensional numerical experiments. *Q. J. R. Meteorol. Soc.*, 112: 899-929.

Collins, R. L., X. Tao, and C. S. Gardener, 1996: Gravity wave activity in the upper mesosphere over Urbana, Illinois: lidar observations and analysis of gravity wave propagation models, *J. Atmos. Terr. Phys.*, 58(16), 1905-1926.

Collins, R. L. and R. W. Smith, (2004), Evidence of damping and overturning of gravity waves in the Arctic mesosphere: Na lidar and OH temperature observations, *J. Atmos. Solar-Terr. Phys.*, 66, 867-879.

- Dornbrack, A., M. Leutbecher, R. Kivi, and E. Kyro (1999), Mountain wave induced record low stratospheric temperatures above northern Scandinavia, *Tellus, Ser. A*, 51, 951-963.
- Dunkerton, T. J. and N. Butchart (1984), Propagation and Selective Transmission of Internal Gravity Waves in a sudden warming, *J. Atmos. Sci.*, 41, 1443-1460.
- Durrán, D. R., and J. B. Klemp (1987), Another look at downslope winds, part II, Nonlinear amplification beneath wave over-turning layers, *J. Atmos. Sci.*, 44, 3402-3412.
- Ern, M., P. Preusse, J. C. Gille, C. L. Hepplewhite, M. G. Mlynczak, J. M. Russell III, and M. Riese (2011), Implications for atmospheric dynamics derived from global observations of gravity wave momentum flux in stratosphere and mesosphere, *J. Geophys. Res.*, 116, D19107, doi:10.1029/2011JD015821.
- Espy, P. J., G. O. L. Jones, G. R. Swenson, J. Tang, and M. J. Taylor (2004a), Tidal modulation of the gravity-wave momentum flux in the Antarctic mesosphere, *Geophys. Res. Lett.*, 31, L11111, doi:10.1029/2004GL019624.
- Espy, P. J., G. O. L. Jones, G. R., Swenson, J. Tang, and M. J. Taylor (2004b), Seasonal variations of the gravity wave momentum flux in the Antarctic mesosphere and lower thermosphere, *J. Geophys. Res.*, 109, D23109, DOI:10.1029/2003JD004446.
- Farmer, D., and L. Armi (1999), Stratified flow over topography: The role of small-scale entrainment and mixing in flow establishment, *Proc. R. Soc. London, Ser. A*, 455, 3221-3258.
- Forbes, J. M., J. Gu and S. Miyahara (1984), On the interactions between gravity waves and the diurnal propagating tide, *Planet. Space Sci.*, 39, 9, 1249-1257.
- Fritts, D. C., D. Janches, and W. K. Hocking (2010), Southern Argentina Agile Meteor Radar: Initial assessment of gravity wave momentum fluxes, *J. Geophys. Res.*, 115, D19123.

- Fritts, D. C. (1984), Shear Excitation of Atmospheric Gravity Waves. Part II: Nonlinear Radiation from a Free Shear Layer. *J. Atmos. Sci.*, 41, 524-537.
- Fritts, D. C. (1984b), Gravity wave saturation in the middle atmosphere: A review of theory and observations, *Rev. Geophys.*, doi: 10.1029/RG022i003p00275.
- Fritts, D. C., T. Tsuda, T. E. VanZandt, S. A. Smith, T. Sato, S. Fukao, S. Kato (1990), Studies of velocity fluctuations on the lower atmosphere using the MU radar, II, Momentum fluxes and energy densities, *J. Atmos. Sci.*, 47, 51-66.
- Fritts, D. C., and W. Lu, (1993), Spectral Estimates of Gravity Wave Energy and Momentum Fluxes. Part II: Parameterization of Wave Forcing and Variability, *J. of The Atmos. Sci.*, 50, 22, 3695-3713.
- Fritts, D. C. and S. L. Vadas (2008), Gravity wave penetration into the thermosphere: sensitivity to solar cycle variations and mean winds, *Ann. Geophys.*, 26, 3841-3861.
- Fritts, D. C., and G. D. Nastrom (1992), Sources of Mesoscale Variability of Gravity Waves. Part II: Fronal, Convective, and Jet Stream Excitation. *J. Atmos. Sci.*, 49, 111-127.
- Fritts, D. C., P.-D. Pautet, K. Bossert, M. J. Taylor, B. P. Williams, H. Iimura, T. Yuan, N. J. Mitchell, and G. Stober (2014), Quantifying gravity wave momentum fluxes with Mesosphere Temperature Mappers and correlative instrumentation, *J. Geophys. Res. Atmos.*, 119, doi:10.1002/2014JD022150.
- Fritts, D. C., and R. A. Vincent (1987), Mesospheric momentum flux studies at Adelaide, Australia: Observations and a gravity wave/tidal interaction model, *J. Atmos. Sci.*, 44, 605-619.

- Fritts, D. C., L. Wang, J. Werne, T. Lund, and K. Wang (2009), Gravity Wave Instability Dynamics at High Reynolds Numbers. Part 1: Wave Field Evolution at Large Amplitudes and High Frequencies, *J. Atmos. Sci.* 66, 1126-1148.
- Fritts, D. C. (2015), *Encyclopedia of Atmospheric Sciences: Gravity Waves*, 2nd edition, Vol. 3, ISBN:9780123822253.
- Gardner, C. S. and J. D. Shelton (1985), Density Response of Neutral Atmospheric Layers to Gravity Wave Perturbations, *J. Geophys. Res.*, 90(2), 1745-754.
- Geller, M. A., M. J. Alexander, P. T. Love, J. Bacmeister, M. Ern, A. Hertzog, E. Manzini, P. Preusse, K. Sato, A. A. Scaife, and T. Zhou, (2013), A Comparison between Gravity Wave Momentum Fluxes in Observations and Climate Models, *J. of Climate*, 26, 6383-6404.
- Garcia, R. R. and S. Solomon (1985), The Effect of Breaking Gravity Waves on the Dynamics and Chemical Composition of the Mesosphere and Lower Thermosphere, *J. Geophys. Res.* 90, D2, 3850-3868.
- Heale, C. J., J. B. Snively, and M. P. Hickey (2014), Numerical simulation of the long-range propagation of gravity wave packets at high latitudes, *J. Geophys. Res. Atmos.*, 119, 11, 116-11, 134, doi:10.1002/2014JD022099.
- Hecht, J. H., R. L., Walterscheid, M. P. Hickey, and S. J. Franke, 2001: Climatology and modeling of quasi-monochromatic atmospheric gravity waves observed over Urbana Illinois, *J. Geophys. Res.*, 106(D6), 5181-5195.
- Hecht, J. H., R. L. Walterscheid, D. C. Fritts, J. R. Isler, D. C. Senft, C. S. Gardner, and S. J. Franke, 1997: Wave breaking signatures in OH airglow and sodium densities and temperatures 1. Airglow imaging, Na lidar, and MF radar observations, *J. Geophys. Res.*, 102(D6), 6655-6668.

- Hertzog, A., M. J. Alexander, and R. Plougonven (2012), On the Intermittency of Gravity Wave Momentum Flux in the Stratosphere, *J. Atmos. Sci.*, 69, 3433-3448.
- Hitchman, M., K. W. Bywaters, D. C. Fritts, L. Coy, E. Kudeki, and F. Surucu (1992) Mean Winds and Momentum Fluxes over Jicamarca, Peru, during June and August 1987. *J. Atmos. Sci.*, **49**, 2372–2383.
- Hines, C. O. (1960), Internal atmospheric gravity waves at ionospheric heights, *Can. J. Phys.*, 38, 1441-1481.
- Holton, J. R. (1982), The role of gravity wave induced grad and diffusion in the momentum budget of the mesosphere, *J. Atmos. Sci.*, 39, 791–799.
- Holton, J. R. (1984), The generation of mesospheric planetary waves by zonally asymmetric gravity wave breaking, *J. Atmos. Sci.*, 41, 3427–3430, 1984.
- Hu, X., A. Z. Liu, C. S. Gardener, and G. R. Swenson, 2002: Characteristics of quasi-monochromatic gravity waves observed with Na lidar in the mesopause region at Starfire Optical Range, NM, *Geophys. Res. Lett*, 29(24), 2169, doi:10.1029/2002GL014975.
- Isler, J. R., M. J. Taylor, and D. C. Fritts, 1997: Observational evidence of wave ducting and evanescence in the mesosphere, *J. Geophys. Res.*, 102(D22), 26,301-26,313.
- Jiang, Q., A. Reinecke, and J. D. Doyle, (2014), Orographic Wave Drag over the Southern Ocean: A Linear Theory Perspective, *J. of The Atmos. Sci.*, 71, 4235-4252.
- Kim, Y.-J., S. D. Eckermann, H.-Y. Chun, (2003), An overview of the past, present and future of gravity-wave drag parameterization for numerical climate and weather prediction models, *Atmosphere-Ocean*, 41:1, 65-98, DOI: 10.3137/ao.410405.
- Krassovsky, V. I. (1972), Infrasonic variation of OH emission in the upper atmosphere, *Ann. Geophys*, 28, 739-746.

- Lane, T. P., R. D. Sharman (2006), Gravity wave breaking, secondary wave generation, and mixing above deep convection in a three-dimensional cloud model, *Geophys. Res. Lett.* 33, L23813, DOI:10.1029/2006GL027988.
- Lieberman, R. S., D. M. Riggin, and D. E. Siskind (2013), Stationary waves in the wintertime mesosphere: Evidence for gravity wave filtering by stratospheric planetary waves, *J. Geophys. Res. Atmos.*, 118, 3139-3149, doi:10.1002/jgrd.50319.
- Liller, W. and F. L. Whipple (1954), Special Supplement to *J. Atmospheric and Terr. Phys.* 1, 112.
- Lilly, D. K., and P. J. Kennedy (1973), Observations of a Stationary Mountain Wave and its Associated Momentum Flux and Energy Dissipation, *J. Atmos. Sci.*, 30, 1135-1152.
- Liu, A. Z., X. Lu, and S. J. Franke (2013), Diurnal variation of gravity wave momentum flux and its forcing on the diurnal tide, *J. Geophys. Res. Atmos.*, 118, 1668-1678, doi:10.1029/2012JD018653.
- Manson, A. H., C. E. Meek, Y. Luo, W. K. Hocking, J. MacDougall, D. Riggin, D. C. Fritts, and R. A. Vincent (2003), Modulation of gravity waves by planetary waves (2 and 16 d): observations with the North American-Pacific MLT-MFR radar network, *J. Atmos. Solar Terr. Phys.*, 65, 85-104. DOI:10.1016/S1364-6826(02)00282-1.
- McFarlane, N., (1987), The Effect of Orographically Excited Gravity Wave Drag on the General Circulation of the Lower Stratosphere and Troposphere, *J. of The Atmos. Sci.*, 44, 14, 1775-1800.
- McLandress, C., T. G. Shepherd, S. Polavarapu, S. R. Beagley, (2012), Is Missing Orographic Gravity Wave Drag near 60°S the Cause of the Stratospheric Zonal Wind Biases in Chemistry-Climate Models?, *J. of The Atmos. Sci.*, 69, 802-818.

- McLandress, C., (1998), On the importance of gravity waves in the middle atmosphere and their parameterization in general circulation models, *J. Atmos. and Solar-Terr. Phys.*, 60, 1357-1383.
- Murphy, D. J., and R. A. Vincent (1993), Estimates of momentum flux in the mesosphere and lower thermosphere over Adelaide, Australia, from March 1985 to February 1986, *J. Geophys. Res.*, 98(D10), 18617–18638.
- Nakamura, T., D. C. Fritts, J. R. Isler, T. Tsuda, R. A. Vincent, and I. M. Reid (1997), Short-period fluctuations of the diurnal tide observed with low-latitude MF and meteor radars during CADRE: Evidence for gravity wave/tidal interactions, *J. Geophys. Res.*, 102, D22, 26,225-26,238.
- Nakamura, T., T. Tsuda, M. Yamamoto, S. Fukao, and S. Kato (1993), Characteristics of gravity waves in the mesosphere observed with the middle and upper atmosphere radar: 1. Momentum flux, *J. Geophys. Res.*, 98(D5), 8899–8910.
- Namboothiri, S. P., T. Tsuda, M. Tsutsumi, and T. Nakamura, 1996: Simultaneous observations of mesospheric gravity waves with the MU radar and a sodium lidar, *J. Geophys. Res.*, 101(D2), 4057-4063.
- Nappo, C. J.: An introduction to atmospheric gravity waves, Amsterdam: Academic Press, International geophysics series, vol. 102, ISBN 9780123852236, 2013.
- Nastrom, G. D., and D. C. Fritts (1992), Sources of mesoscale variability of gravity waves, I: Topographic excitation, *J. Atmos. Sci.*, 49, 101-110.
- Nastrom, G. D., D. C. Fritts, and K. S. Gage (1987), An Investigation of Terrain Effects on the Mesoscale Spectrum of Atmospheric Motions. *J. Atmos. Sci.*, 44, 3087-3096.

- Nielsen, K., Taylor, M.J, Hibbins, R.E, Jarvis, M.J., and J.M. Russell III, 2012: On the nature of short-period mesospheric gravity wave propagation over Halley, Antarctica, *J. Geophys. Res.*, 117(D05124), doi:10.1029/2011JD016261.
- Pautet, P.-D., Taylor, M. J., Pendelton, W. R. Jr., Zhao, Y., Yuan, T., Esplin, R., and D. McLain (2014), An Advanced Mesospheric Temperature Mapper for high-latitude airglow studies, *App. Optics*, 53(26), 5934-5943.
- Pandaya, R. E. and M. J. Alexander (1999), Linear Stratospheric Gravity Waves above Convective Thermal Forcing, *J. Atmos. Sci.*, 56, 2434-2446.
- Palmer, T. N., G. J. Shutts, and R. Swinbank (1986), Alleviation of a systematic westerly bias in general circulation and numerical weather prediction models through an orographic gravity wave drag parameterization, *Q. J. R. Meteorol. Soc.*, 112: 1001-1039. Doi:10.1002/qj.49711247406.
- Peterson, A. W. and L. M. Keiffaber (1973), Infrared photography of OH airglow structures. *Nature* 242: 321-322.
- Pfister, L., S. Scott, M. Loewenstein, S. Bowen, and M. Legg, (1993), Mesoscale Disturbances in the Tropical Stratosphere Excited by Convection: Observations and Effects on the Stratospheric Momentum Budget, *J. Atmos. Sci.*, 50, 1058-1075.
- Plougonven, R., A. Hertzog, and H. Teitelbaum, 2008: Observations of a large-amplitude mountain wave breaking over the Antarctic Peninsula, *J. Geophys. Res.*, 113(D16), doi:10.1029JD009739.
- Preusse, P., S. D. Eckermann, M. Ern, (2008), Transparency of the atmosphere to short horizontal wavelength gravity waves, *J. Geophys. Res.*, 113, D24104, doi:10.1029/2007JD009682.

- Reid, I. M., R. Ruster, P. Czechowsky, and G. Schmidt (1988), VHF radar measurements of momentum flux in the summer polar mesosphere over Andenes (69°N, 16°E), Norway, *Geophys. Res. Lett.*, 15(11), 1263-1266.
- Salby, M. L., and R. R. Garcia (1987), Transient Response to Localized Episodic Heating in the Tropics. Part I: Excitation and Short-Time Near-Field Behavior. *J. Atmos. Sci.*, 44, 458-498.
- Scinocca, J. F., and R. Ford (2000), The Nonlinear Forcing of Large-Scale Internal Gravity Waves by Stratified Shear Instability. *J. Atmos. Sci.*, 57, 653-672.
- Scinocca, J. F., (2003), An Accurate Spectral Nonorographic Gravity Wave Parameterization for General Circulation Models, *J. of The Atmos. Sci.*, 60, 667-682.
- Shelton, J. D., C.S. Gardener and C.F. Sechrist Jr., 1980: Density Response of the Mesospheric Sodium Layer to Gravity Wave Perturbations, *Geophys. Res. Lett.* 7(12), 1069-1072.
- Simkhada, D.B., J. B. Snively, M. J. Taylor, and S. J. Franke 2009: Analysis and modeling of ducted and evanescent gravity waves observed in the Hawaiian airglow, *Ann. Geophys.*, 27, 3213-3224.
- Smith, R. B. (1978), A measurement of mountain drag, *J. Atmos. Sci.*, 35, 1644-1654.
- Smith, A. K., (1995), Longitudinal Variations in Mesospheric Winds: Evidence for Gravity Wave Filtering by Planetary Waves, *J. of the Atmos. Sci.*, 53, 8, 1156-1173.
- Smith, R. B., B. K. Woods, J. Jensen, W. A. Cooper, J. D. Doyle, Q. Jiang, V. Grubisic, (2008), Mountain Waves Entering the Stratosphere, *J. Atmos. Sci.*, 65, 2543-2562.
- Snively, J. B., K. Nielsen, M. P. Hickey, C. J. Heale, M. J. Taylor, and T. Moffat-Griffin (2013), Numerical and statistical evidence for long-range ducted gravity wave propagation over Halley, Antarctica, *Geophys. Res. Lett.*, 40, 4813-4817, doi:10.1002/grl.50926.

- Snively, J. B., V. P. Pasko, M. J. Taylor, and W. K. Hocking (2007) Doppler Ducting of short-period gravity waves by midlatitude tidal wind structure, *J. Geophys. Res.*, 112, A03304, doi:10.1029/2006JA011895.
- Swenson, G. R. and C. S. Gardner 1998: Analytical models for the responses of the mesospheric OH* and Na layers to atmospheric gravity waves, *J. Geophys. Res.*, 103(D6), 6271-6294.
- Taylor, M. J., E. H. Ryan, T. F. Tuan, and R. Edwards (2003), Evidence of Preferential Directions for Gravity Wave Propagation Due to Wind Filtering in the Middle Atmosphere, *J. Geophys. Res.*, 98, A4, 6047-6057.
- Taylor, M. J., W. R. Pendleton, S. Clark, H. Takahashi, D. Gobbi, and R. A. Goldberg, 1997: Image measurements of short-period gravity waves at equatorial latitudes, *J. Geophys. Res.*, 102(D22), 26,283-26,299.
- Tsuda, T., Y. Murayama, M. Yamamoto, S. Kato, S. Fukao (1990), Seasonal variation of momentum flux in the mesosphere observed with the MU radar, *Geophys. Res. Lett.*, 17(6), 725-728.
- Vadas, S., J. Yue, and T. Nakamura (2012), Mesospheric concentric gravity waves generated by multiple convective storms over the North American Great Plain, *J. Geophys. Res.* 117, D07113, DOI:10.1029/2011JD17025.
- Vadas, S. L., D. C. Fritts, and M. J. Alexander (2003), Mechanism for the Generation of Secondary Waves in Wave Breaking Regions, *J. Atmos. Sci.*, 60, 194-214.
- Vadas, S. L., and M. J. Nicolls, 2009: Temporal evolution of neutral, thermospheric winds and plasma response using PFISR measurements of gravity waves, *J. Atmos. and Solar-Terr Phys.*, 71, 744-770.

- Vincent, R. A., and I. M. Reid, 1983: HF Doppler measurements of mesospheric momentum fluxes, *J. Atmos. Sci.*, 40, 1321-1333.
- Wang, D.-Y., and D. C. Fritts (1990) Mesospheric Momentum Fluxes Observed by the MST Radar at Poker Flat, Alaska. *J. Atmos. Sci.*, **47**, 1512–1521.
- Walterscheid, R. L. (1981), Inertio-Gravity Wave Induced Accelerations of Mean Flow Having an Imposed Periodic Component: Implications for Tidal Observations in the Meteor Region , *J. Geophys. Res.*, 86, C10, 9698-9706.
- Williams, B. P., M. A. White, D. A. Krueger, and C. Y. She, (2002), Observation of a large amplitude wave and inversion layer leading to convective instability in the mesopause region over Fort Collins CO (41° N, 105° W), *Geophys. Res. Lett.*, 29(17), 1850, doi:10.1029/2001GL014514, 2002.
- Wilson, R., M.L. Chanin, and A. Hauchecorne, 1991: Gravity Waves in the Middle Atmosphere Observed by Rayleigh Lidar 2. Climatology, *J. Geophys. Res.*, 96(D3), 5169-5183.
- Yue, J., C.-Y. She, and H.-L. Liu (2010), Large wind shears and stabilities in the mesopause region observed by Na wind-temperature lidar at midlatitude, *J. Geophys. Res.*, 115, A10307, doi:10.1029/2009JA014864.
- Yue, J., S. L. Vadas, C.-Y. She, T. Nakamura, S. C. Reising, H.-L. Liu, P. Stamus, D. A. Krueger, W. Lyons, and T. Li, 2009: Concentric gravity waves in the mesosphere generated by deep convective plumes in the lower atmosphere near Fort Collins, Colorado, *J. Geophys. Res.*, 114, D06104, doi: 10.1029/2008JD011244.

Appendix A

Gravity Wave Equations and Derivations

Polarization Relations

Derivation of equation (2.11)

$$-i\hat{\omega}\tilde{u} + w' \frac{\partial \bar{u}}{\partial z} + ik \frac{p'}{\bar{\rho}} = 0$$

Starting from 2.1 and expanding the material derivative and linearizing:

$$\frac{Du}{Dt} + \frac{1}{\rho} \frac{\partial p}{\partial x} = \frac{d\bar{u}}{dt} + \frac{du'}{dt} + (\bar{u} + u') \frac{\partial(\bar{u} + u')}{\partial x} + (\bar{w} + w') \frac{\partial(\bar{u} + u')}{\partial z} + \left(\frac{1 - \frac{\rho'}{\bar{\rho}}}{\bar{\rho}} \right) \left[\frac{\partial p'}{\partial x} + \frac{\partial \bar{p}}{\partial x} \right] = 0$$

Removing terms that go to zero, or small perturbation*perturbation terms:

$$\frac{du'}{dt} + \bar{u} \frac{\partial u'}{\partial x} + w' \frac{\partial \bar{u}}{\partial z} + \frac{\partial}{\partial x} \left(\frac{p'}{\bar{\rho}} \right) = 0 \quad (2.6)$$

Using the following relations from equation 2.10:

$$\frac{du'}{dt} = \tilde{u}(-i\omega)$$

$$\bar{u} \frac{\partial u'}{\partial x} = \bar{u}(ik)\tilde{u}$$

And

$$\omega = kc$$

$$\hat{\omega} = k(c - u)$$

Equation 2.11 can be obtained as

$$-i\hat{\omega}\tilde{u} + w' \frac{\partial \bar{u}}{\partial z} + ik \frac{p'}{\bar{\rho}} = 0$$

Derivation of equation (2.12)

$$-i\hat{\omega}\tilde{w} + \frac{\partial}{\partial z} \left(\frac{p'}{\bar{\rho}} \right) - \frac{p'}{\bar{\rho}} \frac{1}{H} + g \frac{\rho'}{\bar{\rho}} = 0$$

Starting from 2.2

$$\frac{Dw}{Dt} + \frac{1}{\rho} \frac{\partial p}{\partial z} + g = \frac{dw'}{dt} + (\bar{u} + u') \frac{dw'}{dx} + w' \frac{dw'}{dz} + \left(1 - \frac{\rho'}{\bar{\rho}}\right) \frac{\partial}{\partial z} (p' + \bar{p}) + g = 0$$

Removing zero and perturbation*perturbation terms

$$\frac{dw'}{dt} + \bar{u} \frac{dw'}{dx} + \frac{1}{\bar{\rho}} \frac{\partial}{\partial z} p' + \frac{\rho'}{\bar{\rho}} g = 0$$

Convert $\frac{1}{\bar{\rho}} \frac{\partial}{\partial z} p'$ in terms of $\frac{\partial}{\partial z} \left(\frac{p'}{\bar{\rho}}\right)$

Note that $\frac{d}{dz}(\bar{p}) = -g\bar{\rho}$ and

$$\frac{\partial}{\partial z} \left(\frac{p'}{\bar{\rho}}\right) = \frac{\bar{\rho} \frac{\partial}{\partial z} p' - p' \frac{\partial}{\partial z} \bar{\rho}}{\bar{\rho}\bar{\rho}} = \frac{\partial}{\partial z} p' + \frac{p'}{H}$$

So

$$\frac{1}{\bar{\rho}} \frac{\partial}{\partial z} p' = \frac{\partial}{\partial z} \left(\frac{p'}{\bar{\rho}}\right) - \left(\frac{p'}{\bar{\rho}}\right) \left(\frac{1}{H}\right)$$

Thus we can substitute this in to obtain equation 2.7:

$$\frac{dw'}{dt} + \bar{u} \frac{\partial w'}{\partial x} + \frac{\partial}{\partial z} \left(\frac{p'}{\bar{\rho}}\right) - \frac{1}{H} \left(\frac{p'}{\bar{\rho}}\right) + g \frac{\rho'}{\bar{\rho}} = 0 \quad (2.7)$$

Using equation 2.10, equation 2.7 can be simplified to:

$$-i\omega w' + \bar{u} i k w' + \frac{\partial}{\partial z} \left(\frac{p'}{\bar{\rho}}\right) - \frac{\rho'}{\bar{\rho}} \left(\frac{1}{H}\right) + g \frac{\rho'}{\bar{\rho}} = 0$$

Combining terms, this simplifies to equation 2.12:

$$-i\omega \tilde{w} + \frac{\partial}{\partial z} \left(\frac{p'}{\bar{\rho}}\right) - \frac{p'}{\bar{\rho}} \frac{1}{H} + g \frac{\rho'}{\bar{\rho}} = 0 \quad (2.12)$$

Derivation of equation (2.13)

$$i\omega \tilde{\rho} + \frac{N^2}{g} \tilde{w} = 0$$

Starting from equation 2.3

$$\frac{D\theta}{Dt} = \frac{d(\bar{\theta} + \theta')}{dt} + (\bar{u} + u') \frac{\partial(\bar{\theta} + \theta')}{\partial x} + (w') \frac{\partial(\bar{\theta} + \theta')}{\partial z} = 0$$

Removing zero and small perturbation*perturbation terms:

$$\frac{d\theta'}{dt} + \bar{u} \frac{\partial\theta'}{\partial x} + w' \frac{\partial\bar{\theta}}{\partial z} = 0$$

Dividing by $\bar{\theta}$ the following is obtained:

$$\frac{d}{dt} \left(\frac{\theta'}{\bar{\theta}} \right) + \bar{u} \frac{\partial}{\partial x} \left(\frac{\theta'}{\bar{\theta}} \right) + w' \left(\frac{\partial\bar{\theta}}{\partial z} \right) \left(\frac{1}{\bar{\theta}} \right) = 0$$

Using the relation for the buoyancy frequency $\frac{N^2}{g} = \frac{1}{\bar{\theta}} \frac{d\bar{\theta}}{dz}$

Equation 2.8 is obtained:

$$\frac{d}{dt} \left(\frac{\theta'}{\bar{\theta}} \right) + \bar{u} \frac{\partial}{\partial x} \left(\frac{\theta'}{\bar{\theta}} \right) + w' \frac{N^2}{g} = 0 \quad (2.8)$$

Using equation 2.10, we obtain

$$-i\omega\tilde{\theta} + \frac{N^2}{g}\tilde{w} = 0$$

This can be simplified to equation 2.13 using the Boussinesq approximation:

$$\tilde{\theta} \approx -\tilde{\rho}$$

$$i\omega\tilde{\rho} + \frac{N^2}{g}\tilde{w} = 0 \quad (2.13)$$

Derivation of equation (2.14)

Starting from 2.4:

$$\frac{1}{\rho} \frac{D\rho}{Dt} + \frac{\partial u}{\partial x} + \frac{\partial w}{\partial z} = 0$$

Expanding:

$$\frac{1}{\bar{\rho}\left(1+\frac{\rho'}{\bar{\rho}}\right)}\left[\frac{d}{dt}(\bar{\rho}+\rho')+(\bar{u}+u')\frac{d}{dx}(\bar{\rho}+\rho')+(w')\frac{d}{dz}(\bar{\rho}+\rho')\right]+\frac{\partial(\bar{u}+u')}{\partial x}+\frac{\partial(\bar{w}+w')}{\partial z}=0$$

Removing zero terms:

$$\left(\frac{1}{\bar{\rho}}-\frac{\rho'}{\bar{\rho}\bar{\rho}}\right)\left[\frac{d}{dt}\rho'+\bar{u}\frac{d}{dx}\rho'+w'\frac{d}{dz}(\bar{\rho}+\rho')\right]+\frac{\partial u'}{\partial x}+\frac{\partial w'}{\partial z}=0$$

Further Expanding and removing perturbation* perturbation terms:

$$\frac{d}{dt}\left(\frac{\rho'}{\bar{\rho}}\right)+\bar{u}\frac{\partial}{\partial x}\left(\frac{\rho'}{\bar{\rho}}\right)+w'\frac{d}{dz}\bar{\rho}+\frac{\partial u'}{\partial x}+\frac{\partial w'}{\partial z}=0$$

Simplifying using $\frac{d}{dz}\bar{\rho}=-\frac{\bar{\rho}}{H}$, equation 2.9 is obtained:

$$\frac{d}{dt}\left(\frac{\rho'}{\bar{\rho}}\right)+u\frac{\partial}{\partial x}\left(\frac{\rho'}{\bar{\rho}}\right)+\frac{\partial u'}{\partial x}+\frac{\partial w'}{\partial z}-\frac{w'}{H}=0 \quad (2.9)$$

Using the relations from equation 2.10, equation 2.14 can be obtained:

$$-i\omega\tilde{\rho}+ik\tilde{u}+\frac{\partial\tilde{w}}{\partial z}-\frac{\tilde{w}}{H}=0 \quad (2.14)$$

Deriving the Dispersion Relation

Starting from equations 2.11-2.14, assuming no wind shear and simplifying derivative terms, the

following 4 equations are obtained:

$$-i\omega\tilde{u}+ik\tilde{p}=0 \quad (A2.11)$$

$$-i\omega\tilde{w}+\left(im-\frac{1}{2H}\right)\tilde{p}+g\tilde{\rho}=0 \quad (A2.12)$$

$$i\omega\tilde{\rho}+\frac{N^2}{g}\tilde{w}=0 \quad (A2.13)$$

$$-i\hat{\omega}\tilde{\rho} + ik\tilde{u} + \left(im - \frac{1}{2H}\right)\tilde{w} = 0 \quad (\text{A2.14})$$

Using equations A2.11 and A2.13, u and ρ can be eliminated, resulting in the equations listed below:

$$-i\hat{\omega}\tilde{w} + \left(im - \frac{1}{2H}\right)\tilde{p} + i\frac{N^2}{\hat{\omega}}\tilde{w} = 0$$

$$\frac{N^2}{g}\tilde{w} + \frac{ik^2}{\hat{\omega}}\tilde{p} + \left(im - \frac{1}{2H}\right)\tilde{w} = 0$$

Using a polarization relation as in equation 2.17, p can be eliminated and an equation in terms of w can be obtained. After removing imaginary terms, the following is left:

$$\hat{\omega}^2 \left[k^2 + m^2 + \frac{N^2}{g} \frac{1}{2H} - \frac{1}{4H^2} \right] = N^2 k^2$$

Using equation 21 from [Fritts and Alexander, 2003], and assuming that the speed of sound c_s goes to infinity, the following relation can be obtained:

$$\frac{N^2}{g} = \frac{1}{H}$$

Using this relation, the dispersion relation can be simplified to that given in equation 2.20:

$$\hat{\omega} = \frac{k^2 N^2}{\left(k^2 + m^2 + \frac{1}{4H^2}\right)} \quad (\text{2.20})$$

Momentum Flux

The vertical flux of horizontal momentum per unit density can be calculated in the following way from equation 2.23:

$$\langle u'w' \rangle \quad (2.23)$$

The process for deriving this equation in terms that can be used with measurements from a lidar or radar system and an imager is given below:

1. Using the continuity equation, a relation between u' and w' can be obtained:

$$\begin{aligned} \nabla \cdot \mathbf{v}' &= 0 \\ \frac{\partial u'}{\partial x} + \frac{\partial w'}{\partial z} &= 0 \end{aligned}$$

For medium frequency waves, u' and w' can be related by the polarization relation:

$$k\tilde{u} = -m\tilde{w}$$

This results in the following relation:

$$\tilde{w} = \frac{-k}{m} \tilde{u} = \frac{\hat{\omega}}{N} \tilde{u}$$

2. Derivation of $u' = \frac{g}{N} \frac{\theta'}{\theta}$

Where

θ = Average Temperature

θ' = Temperature Perturbation

g = gravitational acceleration

N^2 = Buoyancy Frequency

u' = Horizontal Wind Perturbation

Note that u' can either be for meridional, zonal, or a combination transposed into the direction of gravity wave propagation.

Starting from material derivative given in equation 2.4, where thermal forcing is assumed to be zero, and expanding the equation into horizontal (meridional and zonal), vertical, and time components, the following is obtained:

$$\frac{\partial(\bar{\theta} + \theta')}{\partial t} + (\bar{u} + u') \frac{\partial(\bar{\theta} + \theta')}{\partial x} + (\bar{w} + w') \frac{\partial(\bar{\theta} + \theta')}{\partial z} = 0$$

Expansion yields:

$$\frac{\partial \bar{\theta}}{\partial t} + \frac{\partial \theta'}{\partial t} + \frac{\bar{u} \partial \bar{\theta}}{\partial x} + \frac{\bar{u} \partial \theta'}{\partial x} + \frac{u' \partial \bar{\theta}}{\partial x} + \frac{u' \partial \theta'}{\partial x} + \frac{\bar{w} \partial \bar{\theta}}{\partial z} + \frac{\bar{w} \partial \theta'}{\partial z} + \frac{w' \partial \bar{\theta}}{\partial z} + \frac{w' \partial \theta'}{\partial z} = 0$$

The small terms and zero terms are eliminated from this expanded equation. The assumptions are as follows:

- mean temperature does not change with time
- mean temperature does not change in horizontal direction
- average vertical wind is zero
- wind times temperature perturbations are small

The simplified material derivative is given as:

$$\frac{\partial \theta'}{\partial t} + \frac{\bar{u} \partial \theta'}{\partial x} + \frac{w' \partial \bar{\theta}}{\partial z} = 0$$

The perturbations for this calculation are given by sinusoidal functions:

$$\begin{aligned} \theta' &= \tilde{\theta} e^{i(kx+mz-\omega t)} \\ \frac{\partial \theta'}{\partial t} &= -(i\omega) \tilde{\theta} e^{i(kx+mz-\omega t)} \\ \frac{\partial \theta'}{\partial x} &= (ik) \tilde{\theta} e^{i(kx+mz-\omega t)} \end{aligned}$$

Plugging these above equations into the material derivative yields:

$$-(i\omega)\tilde{\theta}e^{i(kx+mz-\omega t)} + (ik)\tilde{\theta}e^{i(kx+mz-\omega t)}\bar{u} + \tilde{w}e^{i(kx+mz-\omega t)}\frac{\partial\bar{\theta}}{\partial z} = 0$$

$$-(i\omega)\tilde{\theta} + (ik)\tilde{\theta}\bar{u} + \tilde{w}\frac{\partial\bar{\theta}}{\partial z} = 0$$

Then, multiplying by $\frac{g}{\bar{\theta}}$

$$-(i\omega)\tilde{\theta}\frac{g}{\bar{\theta}} + (ik)\tilde{\theta}\bar{u}\frac{g}{\bar{\theta}} + \tilde{w}\frac{\partial\bar{\theta}}{\partial z}\frac{g}{\bar{\theta}} = 0$$

By definition:

$$\omega = kc$$

and

$$\frac{\partial\bar{\theta}}{\partial z}\frac{g}{\bar{\theta}} = N^2$$

Plugging in the above equations yields:

$$\frac{\tilde{\theta}}{\bar{\theta}}ig(-kc + k\bar{u}) + \tilde{w}N^2 = 0$$

$$-\frac{\tilde{\theta}}{\bar{\theta}}ig(\omega_{\text{int}}) + \tilde{w}N^2 = 0$$

Where the intrinsic frequency is defined as:

$$\omega_{\text{int}} = k(c - \bar{u})$$

Now, using the relationship from the continuity equation, the advective derivative can be simplified even further to:

$$i\frac{\tilde{\theta}}{\bar{\theta}}\frac{g}{N} = \tilde{u}$$

3. Derivation of momentum flux $w'u'$

Recall from equation 2.6,

$$u' = \tilde{u}e^{i(kx+mz-\omega t)}$$

$$w' = \tilde{w}e^{i(kx+mz-\omega t)}$$

Thus momentum flux can be calculated using the following equation:

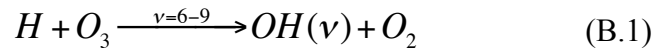
$$\langle u'w' \rangle = \frac{1}{2} \tilde{u}^2 \left(\frac{k}{m} \right) = \frac{1}{2} \left(\frac{\tilde{\theta}}{\tilde{\theta}} \frac{g}{N} \right)^2 \left(\frac{k}{m} \right) \quad (2.24)$$

Appendix B

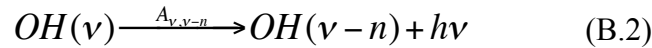
Instrument Information

AMTM Background and Theory

The hydroxyl emission spectrum is dominantly composed of Meinel (vibrational) bands. The AMTM utilizes emissions from the OH(3-1) vibrational band to determine temperatures from the hydroxyl layer. The hydroxyl compound is created from H and O₃ given by the reaction in equation B.1 [Makhlouf, 1995].



The vibrationally excited OH is either quenched by N₂ or O₂ or radiates through the reaction given in equation B.2.



$A_{\nu,\nu-n}$ is the Einstein coefficient which can be derived from the vibrational wave functions as has been done previously [Turnbull and Lowe, 1989; Mies 1974]. The states can be assumed to be in a Boltzmann distribution, and the Einstein coefficient in terms of the rotational temperature can be calculated using equation B.3 [Mies 1974].

$$A_{\nu'' \leftarrow \nu'}(T_{rot}) = \sum_{J', J''} \left(\bar{A}(J'', \nu'' \leftarrow J', \nu') \right) \frac{2(2J'+1)}{Q_{\nu'}(T_{rot})} \exp \left\{ \frac{-E_{i', \nu'}(J')}{kT_{rot}} \right\} \quad (B.3)$$

Where \bar{A} is a total transition probability between states, $Q_{\nu'}$ is the electronic-rotational partition function for the initial state, J' , J'' are the rotational states, and ν' , ν'' are vibrational states. Using this dependence of rotational-vibrational levels on temperature, the temperature of the hydroxyl layer can be obtained through the intensity ratios of emissions. For the AMTM, the

P₁(2) and P₁(4) doublets of the OH(3,1) emission band are used as described in [Pautet et al., 2014].

Sodium Lidar Equations

Lidar Equation:

$$N_s(\lambda, z) = (N_{trans}) * (\sigma(\lambda_{up})n\Delta z) * \left(\frac{A}{4\pi z^2}\right) * (\eta \cdot T_a^2(\lambda)E(\lambda_{up})E(\lambda_{down})G(z)) + N_B\Delta t \quad (3.5)$$

Where

N=number of counts

σ =scattering cross section

n=number density

A=telescope aperture area

η =optical system efficiency

T_a=transmission of air

E=extinction through sodium layer

G=geometrical overlap of laser and telescope view field

N_B=number of background counts

Transmitted number of photons:

$$N_{trans}(\lambda) = \frac{P_L(\lambda) * \Delta t}{(h * c) / \lambda} \quad (3.6)$$

Where

N_{trans} =number of transmitted counts

P_L =Laser power

λ =wavelength

σ =scattering cross section

h =Planck's constant

Δt =laser pulse period

Figure 3.8 shows a diagram of the sodium hyperfine structure. The intensities and frequency offsets from the D2 line (589.1583nm) of the transitions are given in Table B.1 [Fricke and von Zahn, 1985].

Table B.1: Frequency offsets and relative line strengths

	Transition n	$^2S_{1/2}$	$^2P_{3/2}$	Frequency Offset (MHz)	Spatial Average for Multiplet An
D _{2a}	1	F=2	F=3	-621.6	14
D _{2a}	2	F=2	F=2	-680.5	5
D _{2a}	3	F=2	F=1	-715	1
D _{2b}	4	F=1	F=2	1091.1	5
D _{2b}	5	F=1	F=1	1056.6	5
D _{2b}	6	F=1	F=0	1040.8	2

Sodium scattering cross section:

$$\sigma_{na}(\nu, T, V_r, \Omega) = \frac{1}{\sqrt{2\pi}\sigma_D} \frac{e^2 f}{\epsilon_0 m_e c} \sum_n \left(g_n q_n(\Omega) \cdot \exp \left(- \frac{\left[\nu_n - \nu \left(1 - \frac{V_r}{c} \right) \right]^2}{2 \cdot \left(\frac{k_b T}{M \lambda_o} \right)} \right) \right) \quad (3.7)$$

Where

f=oscillator strength

e=charge of electron

m_e=mass of electron

σ_D=Doppler broadening

ε₀=electric constant

k_b=Boltzmann constant

V_r=radial velocity

ν_n, ν=line frequency, laser frequency

g_n=average multiplet strength

λ_o=mean D2 transition wavelength

Appendix C

Equations Used For GW Propagation Environment

Derivations of Sodium Perturbations

Defining R as the mixing ratio:

$$R = \frac{(\bar{\rho}_s + \rho_s')}{(\bar{\rho} + \rho')} \quad (C1)$$

Which expands to:

$$R = \frac{\bar{\rho}_s}{\bar{\rho}} \left[\frac{\rho_s'}{\bar{\rho}_s} - \frac{\rho'}{\bar{\rho}} + 1 \right] \quad (C2)$$

And starting from the continuity equation:

$$\frac{\delta R}{\delta t} + (v \cdot \nabla)R = 0 \quad (C3)$$

Which for two dimensions expands to:

$$\frac{\delta R}{\delta t} + (\bar{u} + u') \frac{\delta}{\delta x} R + (\bar{w} + w') \frac{\delta}{\delta z} R = 0 \quad (C4)$$

The above equation can be split into 3 sections. It is assumed that the mean vertical background wind is zero, that mean values are constant in the horizontal direction, and that multiples of perturbations are negligible compared to other terms. The background density is assumed to change with scale height H.

$$\frac{\delta R}{\delta t} = \frac{\delta}{\delta t} \left[\frac{\rho_s'}{\bar{\rho}} \exp \left(i(kx + mz - \omega t) - \frac{z}{H} \right) - \frac{\bar{\rho}_s \rho'}{\bar{\rho} \bar{\rho}} \exp \left(i(kx + mz - \omega t) - \frac{2z}{H} \right) \right]$$

Simplifies to:

$$\frac{\exp(i(kx+mz-\omega t))}{\bar{\rho}(\exp(-\frac{z}{H}))} \left[\rho_s'(i\omega) - \frac{\bar{\rho}_s(z)}{\bar{\rho}(z)} \rho'(i\omega) \right]$$

The second term in equation C4 expands as follows:

$$(\bar{u} + u') \frac{\delta}{\delta x} \frac{\bar{\rho}_s}{\bar{\rho}} \left[\frac{\rho'_s}{\bar{\rho}_s} - \frac{\rho'}{\bar{\rho}} + 1 \right] = \bar{u} \frac{\delta}{\delta x} \frac{\rho'_s}{\bar{\rho}} + \bar{u} \frac{\delta}{\delta x} \frac{-\bar{\rho}_s}{\bar{\rho}} \frac{\rho'}{\bar{\rho}}$$

This simplifies to the following:

$$\frac{\bar{u} \exp(i(kx+mz-\omega t))}{\bar{\rho} \left(\exp\left(-\frac{z}{H}\right) \right)} \left[ik\rho'_s - ik \frac{\bar{\rho}_s}{\bar{\rho}} \rho' \right]$$

Similarly the third term simplifies as follows:

$$\frac{w' \exp(i(kx+mz-\omega t))}{\bar{\rho} \left(\exp\left(-\frac{z}{H}\right) \right)} \left[\frac{\delta}{\delta z} \bar{\rho}_s + \frac{1}{H} \bar{\rho}_s \right]$$

Dividing similar terms and combining results in the following:

$$-(i\bar{u}k - i\omega) \left(\rho'_s - \rho' \frac{\bar{\rho}_s}{\bar{\rho}} \right) = w' \left[\frac{\delta}{\delta z} \bar{\rho}_s + \frac{1}{H} \bar{\rho}_s \right]$$

Which is rearranged to the following:

$$\rho'_s = \frac{w'}{i\bar{\omega}} \left[\frac{\delta}{\delta z} \bar{\rho}_s + \frac{1}{H} \bar{\rho}_s \right] + \rho' \frac{\bar{\rho}_s}{\bar{\rho}}$$

Using the polarization relation given in equation 2.18, the following is obtained:

$$\rho'_s = \frac{-\rho'}{\bar{\rho}} \frac{g}{N^2} \left[\frac{\delta}{\delta z} \bar{\rho}_s + \frac{1}{H} \bar{\rho}_s \right] + \rho' \frac{\bar{\rho}_s}{\bar{\rho}}$$

Using the Boussinesq approximation $\left(\frac{T'}{T} \sim -\frac{\rho'}{\rho}\right)$ equation 4.5 is obtained:

$$\rho'_s = \frac{g}{N^2} \frac{T'}{T} \left[\frac{\delta}{\delta z} \bar{\rho}_s + \frac{1}{H} \bar{\rho}_s \right] - \bar{\rho}_s \frac{T'}{T} \quad (4.5)$$